PolyPublie
Polytechnique Montréal

POLYTECHNIQUE MONTRÉAL
UNIVERSITÉ D'INGÉNIERIE

Titre: Title:	Modelling of a Solar Thermal Power Plant for Benchmarking Blackbox Optimization Solvers
Auteur: Author:	Mathieu Lemyre Garneau
Date:	2015
Type:	Mémoire ou thèse / Dissertation or Thesis
Référence: Citation:	Lemyre Garneau, M. (2015). Modelling of a Solar Thermal Power Plant for Benchmarking Blackbox Optimization Solvers [Mémoire de maîtrise, École Polytechnique de Montréal]. PolyPublie. https://publications.polymtl.ca/1996/

Document en libre accès dans PolyPublie
Open Access document in PolyPublie

URL de PolyPublie: PolyPublie URL:	https://publications.polymtl.ca/1996/
Directeurs de recherche: Advisors:	Sébastien Le Digabel, Charles Audet, & Christophe Tribes
Programme: Program:	Mathématiques appliquées

Ce fichier a été téléchargé à partir de PolyPublie, le dépôt institutionnel de Polytechnique Montréal
This file has been downloaded from PolyPublie, the institutional repository of Polytechnique Montréal

https://publications.polymtl.ca

UNIVERSITÉ DE MONTRÉAL

MODELLING OF A SOLAR THERMAL POWER PLANT FOR BENCHMARKING BLACKBOX OPTIMIZATION SOLVERS

MATHIEU LEMYRE GARNEAU
DÉPARTEMENT DE MATHÉMATIQUES ET DE GÉNIE INDUSTRIEL
ÉCOLE POLYTECHNIQUE DE MONTRÉAL

MÉMOIRE PRÉSENTÉ EN VUE DE L'OBTENTION
DU DIPLÔME DE MAÎTRISE ÈS SCIENCES APPLIQUÉES
(MATHÉMATIQUES APPLIQUÉES)
DÉCEMBRE 2015

© Mathieu Lemyre Garneau, 2015.

UNIVERSITÉ DE MONTRÉAL

ÉCOLE POLYTECHNIQUE DE MONTRÉAL

Ce mémoire intitulé :

MODELLING OF A SOLAR THERMAL POWER PLANT FOR BENCHMARKING BLACKBOX OPTIMIZATION SOLVERS

présenté par : LEMYRE GARNEAU Mathieu
en vue de l'obtention du diplôme de : Maîtrise ès sciences appliquées
a été dûment accepté par le jury d'examen constitué de :

M. ANJOS F. Miguel, Ph. D., président
M. LE DIGABEL Sébastien, Ph. D., membre et directeur de recherche
M. AUDET Charles, Ph. D., membre et codirecteur de recherche
M. TRIBES Christophe, Ph. D., membre et codirecteur de recherche
M. SAVADOGO Oumarou, D. d'État, membre

RÉSUMÉ

On propose une famille de problèmes d'optimisation originaux pouvant servir de banc d'essai pour les algorithmes d'optimisation de boîtes noires. Les problèmes proposés varient en terme de nombre de variables (5 à 29), de leur type (discrètes, continues, de catégories), du nombre et du type de contraintes (de 5 à 17 contraintes binaires ou continues) ainsi qu'au niveau du nombre de fonctions objectif et de leur nature. Le but étant de tester la performance d'algorithmes d'optimisation pour des problèmes réels d'ingénierie, un modèle numérique d'une centrale électrique solaire thermique avec système de stockage de chaleur à sel fondu a été développé et implémenté. Le modèle simule le fonctionnement des principales composantes d'une telle centrale, soit un champs d'héliostats, un récepteur solaire à cavité, un système de stockage thermique, un échangeur de chaleur et une turbine à vapeur reliée à un alternateur. Afin d'éviter un trop grand nombre de variables, le champs d'héliostats est généré selon une stratégie gloutonne qui consiste à choisir les positions au plus haut rendement individuel en tenant compte de l'efficacité de surface, de l'atténuation atmosphérique et des effets de dépassement. La performance de l'ensemble du champs d'héliostats est calculée par une méthode de Monte-Carlo afin de tenir compte des effets d'ombrage. Les résultats de cette évaluation sont utilisés comme valeurs d'entrées afin de calculer l'évolution du niveau et de la température des unités de stockage au cours de la période simulée. La méthode NUT (nombre d'unité de transfert) est utilisée afin de simuler la performance de l'échangeur de chaleur pour transférer l'énergie du stockage vers le cycle thermique servant à alimenter la turbine de façon à répondre à un profil de demande variable. Quelques modèles auxiliaires sont utilisés afin de générer des contraintes d'optimisation sur le budget, les pertes d'opération et les défaillances. Des résultats sommaires d'optimisation réalisés à l'aide des paramètres par défaut du logiciel NOMAD sont fournis afin de démontrer la validité des problèmes proposés.

ABSTRACT

A new family of problems is provided to serve as a benchmark for blackbox optimization solvers. The problems are single or bi-objective and vary in complexity in terms of the number of variables used (from 5 to 29), the type of variables (integer, real, category), the number of constraints (from 5 to 17) and their types (binary or continuous). In order to provide problems exhibiting dynamics that reflect real engineering challenges, they are extracted from an original numerical model of a concentrated solar power (CSP) power plant with molten salt thermal storage. The model simulates the performance of the power plant by using a high level modeling of each of its main components, namely, an heliostats field, a central cavity receiver, a molten salt heat storage, a steam generator and an idealized powerblock. The heliostats field layout is determined through a simple automatic strategy that finds the best individual positions on the field by considering their respective cosine efficiency, atmospheric scattering and spillage losses as a function of the design parameters. A Monte-Carlo integral method is used to evaluate the heliostats field's optical performance throughout the day so that shadowing effects between heliostats are considered, and the results of this evaluation provide the inputs to simulate the levels and temperatures of the thermal storage. The molten salt storage inventory is used to transfer thermal energy to the powerblock, which simulates a simple Rankine cycle with a single steam turbine. Auxiliary models are used to provide additional optimization constraints on the investment cost, parasitic losses or components failure. The results of preliminary optimizations performed with the NOMAD software using default settings are provided to show the validity of the problems.

TABLE OF CONTENTS

LISTE OF TABLES

LIST OF FIGURES

LIST OF SYMBOLS

Nomenclature

A	heliostat area (m^2)
A_a	receiver aperture area (m^2)
$\vec{A}_h$	area vector of heliostat
A_{proj}	heliostat area perpendicular to incident radiation (m^2)
A_{Re}	receiver absorbing area (m^2)
$\vec{BL}$	bottom left corner position relative to heliostat center
c	thermal capacity (j/kgK)
C	constraint or cost
d	insulation thickness (m)
D	diameter (m)
f	friction factor
F	view factor
G_s	direct solar irradiance at the earth's surface (W/m^2)
h	convection heat transfer coefficient (W/m^2K)
H	height (m)
H_a	height of the center of receiver aperture (m)
$\hat{I}$	incident radiations unit vector
k	thermal conductivity (W/mK)
l	heliostats length (m)
$\dot{m}$	mass flow (kg/s)
m	mass (kg)
n	day of the year
N	number
Nu	Nusselt's number
P	Power (W)
Pr	Prandtl number
$\vec{p}$	position vector
q	heat rate (j/s)
R	thermal resistance
$\hat{R}_h$	direction vector reflected sunlight
Re	Reynold's number

R_{min}	minimum distance between heliostats and the tower (multiple of H_T)
R_{max}	maximum distance between heliostats and the tower (multiple of H_T)
S_h	slant range (m)
S_t	tubes spacing (m)
t	time
T	temperature (K)
$\vec{Tgt}$	target position
$\vec{TL}$	top left corner position relative to heliostat center
$\vec{TR}$	top right corner position relative to heliostat center
ST	steam turbine
w	heliostats width (m)
W_{Re}	receiver aperture width (m)
α_s	sun elevation (deg)
χ	vapor quality
γ_s	sun azimuth (deg)
δ_s	sun declination (deg)
ϵ	emissivity
η	efficiency (deg)
θ_{fld}	angular width of heliostats field (deg)
θ_h	angle between incident and reflected radiations for heliostat h
μ	internal energy (j/kgK)
ρ	reflectivity
σ	Boltzmann constant $(5.67 \times 10^{-8} W/m^2K^4)$ or tensile stress (kg/s^2m)
τ	atmospheric transmissivity
ϕ	powerplant latitude (deg)
ω	sun hour angle (deg)

Subscripts

a	related to the receiver aperture
abs	absorbed
atm	atmosphere
avg	average
AF	anti-freeze
baf	baffle
bot	bottom

$cond$	conduction
$conv$	convection
cos	cosine
$cost$	investment cost
CS	related to the cold storage
dry	dry wall
em	emitted
fld	related to the properties of the field
hel	related to heliostats
HS	related to the hot storage
i, j	general index
in	inlet or inner
ins	insulation
$loss$	losses
min	minimum
max	maximum
ms	molten salt
o	outlet or outer
$pass$	tubes passes
$proj$	projected on a plane perpendicular to incident radiations
rad	radiation
Re	related to the central receiver
r	sun rays index
s	related to the sun
Sg	related to the steam generator
$spill$	spillage
st	steam
$stor$	stored
sur	surface
t	time index
T	related to the tower
top	top
$tube$	tubes
tur	turbine
$shell$	shell passes
wet	wetted wall

LIST OF APPENDICES

CHAPTER 1 INTRODUCTION

Blackbox optimization deals with the task of finding optimal solutions to problems for which the user is unable to make any assumptions with regard to the objective function(s) properties, be it the availability of the derivatives, its continuity, the presence of noise, etc., and to do so by resorting to evaluate the function as few times as possible, because each evaluation of the blackbox might be computationally costly and time consuming. In addition, the feasibility constraints to which the problem is subjected may be equally unknown [4].The functions may come from a complex computer code, or be the result of actual experimental measurements, thereby leaving the user in the dark with regard to the relations that exist between the results and the input parameters [3, 43].

In Engineering, this may also be referred to as *simulation-based optimization*, though in these cases, the algorithms used to optimize the solution may tend to exploit known structures of the problem. The development of actual blackbox optimization solvers is motivated by the need to completely separate the optimization process from the problem [36]. In many cases, one might want to optimize a problem only once, and spending time and resources on tuning the algorithm itself might not be an option. In other situations, the intrinsic mechanics of the problem may not be accessible to a consulting optimization specialist because it is confidential or classified.

Many different approaches to tackle this type of problems already exist in the literature [45], which may range from widely known meta-heuristics like genetic algorithms, particle swarms and simulated annealing, to more sophisticated and mathematically rigorous methods including the *Mesh Adaptative Direct Search* (MADS) [4] algorithm or the TOMLAB solvers [27]. Due to the large variety of problems upon which these algorithms may be applied, scientifically determining which method is the best is a complex thing to do [22, 25, 39]. Thus benchmarking such general optimization methods requires that they be tested against as many problems as possible. Unfortunately, the public library of testable and publishable Engineering problems to do so is quite limited. While there exist many academic, theoretical or numerical problems that may be used to compare their performance, several of these are handpicked and designed with the sole purpose of serving as test problems, and the level to which they are representative of actual Engineering problems is hard to assess. For instance, Rios and Sahinidis [45] used libraries containing some smooth problems to propose a comparison between derivative-free optimization algorithms.

1.1 Concentrated Solar Power

Concentrated Solar Power (CSP) systems harness the energy of the sun using a reflective surface to concentrate direct solar irradiation of a large area onto a smaller receptive area, in order to generate high temperatures, and therefore high heat flux [31]. The heat thereby generated can be used to drive a variety of processes. In coastal regions with low fresh water availability, CSP technologies are explored to provide the energy for the desalination of sea water [24]. In other cases, it is used to facilitate the extraction of oil by using solar energy to heat up underground deposits and increase pressure, a process referred to as "Solar thermal enhanced oil recovery" [20]. But most importantly, CSP can be used for power generation [65], by driving a regular thermodynamic cycle, sunlight being used as the heat source instead of the burning of a combustible that would typically be either nuclear material or fossil fuel. The current work focuses solely on the power generation application.

The CSP approach to solar-based electrical power generation differs from the more popular photovoltaic (PV) in that it does not require that power be generated in the form of electricity right away. Instead, it is gathered in the form of heat, which can be more easily stored in large quantity. This grants CSP a level of dispatchability and reliability that PV and wind power currently lack [10]. In order to store heat and isolate the power cycle from solar transients, the energy of the sunlight is generally not absorbed directly by the working fluid. Instead, it is absorbed by a heat transfer fluid (HTF) with properties that make it easier to store. This hot fluid is stored in isolated tanks until it is needed, and then used as the heat source for a steam generator. The choice of the heat transfer fluid depends on the specific technology that is being used. For lower temperature applications (less than 390˚C), conventional and synthetic oils can be used [58]. For higher temperature applications (500˚C and more), molten salt mixtures have been used successfully [44]. Using an intermediate fluid to store heat instead of just storing the working fluid facilitates the storage greatly : once it is heated, the working fluid is turned to pressurized steam, which means that the whole storage and collector systems would need to work with high pressures ; working with a fluid that has a higher boiling point makes storage more efficient and safer.

While these technologies are not yet widely known to the public, they have actually been explored since the 1970's, and since then, various approaches have been tested [65]. There are four technologies of solar concentrators that stand out at the moment : linear Fresnel reflector (LFR), parabolic dish collectors (also known as dish-stirling) (DS), parabolic through collectors (PTC) and the heliostat field collector (HFC). PTC is the most mature of the four, while HFC is the most recent, and thus, least tested.

Parabolic through collectors are made of long linear mirrors with a parabolic cross-section. A tube, through which flows the HTF, is held at the focal point of the parabolic cross-section over the mirror's length, where it is heated by the concentrated light. The PTC technology is the most mature and cost efficient of the four at the moment [9]. Its most detrimental aspect is the fact that the heated fluid needs to be pumped through kilometers of tubes, which causes high parasitic loads. It also limits the temperature to which the HTF can be heated because it has to flow over long distances in a tube that is exposed to the ambient air.

The heliostat field collector technology uses an array of flat sun-tracking mirrors called "heliostats", that reflect the light onto a receiver located atop a tower. This approach solves the problem of having to pump a fluid through kilometers of tubes and allows the HTF to reach higher temperatures [33]. Since the fluid is used to drive a thermodynamic cycle, a higher HTF temperature means a better maximum efficiency [32]. This technology is the most recent of the four and is the one that offers the best solar-electric aperture related efficiency (more energy is produced for the same reflective surface). While the PTC approach has an aperture efficiency between 11 to 16 %, the heliostat field's aperture's is between 20 and 25 % [57], and both have a comparable land-use efficiency. The receiver is basically a receptive surface made of a light absorbing material that gets heated by sunlight, and that is crossed by tubes through which the HTF flows and gets heated. The Gemasolar experimental power plant in Spain [40] and the Solar Two experimental project [60] both used a cylindrical external receiver. This allowed light to be received from all around the receiver and thus the tower is placed more or less at the center of the field, and the heliostats are all around. The PS20 project [56] instead uses a cavity receiver, a concept according to which light is reflected by the heliostats through an aperture and onto a concave absorbing surface. Having the light absorbed inside the cavity instead of in the open air reduces re-radiation and convection losses, but forces the heliostats to be placed only in front of the receiver instead of all around it. While the concept in its simplest and most common expression uses a heliostat field to concentrate sunlight onto a single central receiver located on top of a tower, typically referred to as "power tower", it is worth noting that there exist at least two alternative approaches to the use of heliostat field. One of those is to use not just one but an array of multiple tower receivers [48]. Such system is complex but allows a better land-use efficiency because since the heliostats do not all have the same aim point, it is possible to organize more densely without creating too much interference between them, and it also allows each heliostat to be placed closer to the tower to which it is aiming, thus reducing atmospheric scattering losses. The other alternative is the use of tower reflectors [49]. In this case, instead of placing the

receiver on top of the tower to be directly aimed at by the heliostats, a secondary central reflector is placed on top of the tower, and this one reflects light to a central receiver located below. This allows the use of a directional cavity receiver because light hits it from a single direction : above.

Compact Fresnel reflectors use long linear mirrors that too adjust with the sun's position through the day. Instead of reflecting light on a central receiver though, they reflect light on long linear receivers on each side of the field. This technology has a generally higher land-use efficiency than the previous two [57].

The Stirling-dish technology uses sun-tracking parabolic mirrors with a small collector and heat engine located at the focal point of each dish [38]. This approach is modular, meaning that each new dish is independent from the others, and new power can be installed quickly without requiring substantial modifications to a larger system like it would be the case for the other centralized approaches, similar to how wind turbines can be added to the grid. Unfortunately, this approach also suffers from the same problem as wind turbines, which is that energy is converted directly to electricity and can hardly be stored. While this technology suffers from the same problem related to storage as PV does all while being less cost-efficient (at least for now), it is worth noting that it is the CSP technology that reaches the highest solar-to-electric efficiency with a conversion rate that was reported to have reached a record 31% [14].

1.2 Creating a new set of blackbox optimization problems

The object of the work described in this text is to provide a new set of engineering based problems to serve as a valid test for the above-mentioned optimization algorithms. These problems are of course not unique and others have presented similar work in order to enrich the public library of problems. For instance, the *Black-Box Optimization Benchmark* [25] was proposed in 2010, and the second edition of a wind farm layout optimization competition was proposed this year by the *Institut de Recherche en Informatique de Toulouse* [62], to name only those.

In order to obtain problems with objective functions and constraints that are representative of practical engineering problems, the idea has been to base them on an actual simulation model. Therefore the objective of the project was two-fold : to create a numerical model of an engineering problem, and then to extract various optimization problems from this model. Considering the growing relevance and interest in CSP technologies [61], the choice was made

to make problems based on this technology.

This text contains a detailed description of the work that was done in modeling a CSP power plant using a heliostat field collector combined with a molten salt cavity receiver and thermal storage, along with a description of the different problems that were derived from it, containing the definition of their objective functions and constraints.

1.3 Structure

This text is structured as follows. Since the work presented in this thesis touches the many different systems of the simulated CSP power plant, no singular literature review is proposed. Instead, a non exhaustive review of the modeling approaches is done on a per-system basis whenever it is deemed relevant.

Chapter 2 presents the definition of the model. We begin by giving a general description of the specific technology simulated for each major subsystem. Section 2.1 gives an overview of the dynamic of the whole system, and of the operational strategy that is used to drive the power plant throughout the day. This section includes a detailed explanation of how the different objects of the model interact with each other. Section 2.2 provides the details of the numerical model used for each of the subsystems. This section shows the level of detail that is used to model each of the components, along with the assumptions and simplifications made to do so. Numerical results showing the behavior of the models with regard to some design parameters are shown on a per-system basis. Section 2.3 presents the auxiliary models used to create additional constraints to guide the optimization process.

Chapter 3 presents the definition of the general blackbox optimization problem and of the specific problems created from the CSP plant model. The qualitative description along with optimization results obtained with the NOMAD [1] software are provided for each problem in Section 3.3. The annexes contain a technical definition including the set of constraints, the list of variables and their ranges, and the list of active model components for every problem.

CHAPTER 2 THE THERMAL SOLAR POWER PLANT MODEL

As it has been mentioned in the introduction, the acronym "CSP" applies to a number of different concepts that each aim to use solar direct irradiation and convert it to heat. In the present work, only one of these variants is studied. This chapter gives details about the technologies that were simulated and the mathematical/numerical models used to represent them.

The system includes an optical concentrator field, a central tower receiver, a thermal storage unit, a steam generator to transfer heat from the storage fluid to the thermodynamic cycle, and the thermodynamic cycle itself using pressurized steam. The receiver-storage-exchanger loop uses molten salt as the heat transfer fluid (HTF).

2.1 System dynamics

This section presents the model dynamics. The first part describes the behavior that is sought to be represented by the numerical model. The second part explains the actual interactions between the different parts of the numerical code.

2.1.1 Physical dynamics

The way the power plant operates is simple: energy enters the system as concentrated sunlight, and leaves the system as generated electricity and losses. Figure 2.1 below illustrates this dynamic. Red arrows indicate systems affected by thermal losses and the blue ones indicates energy consumed to drive some subsystems.

The first component is the sun, of which the position will impact directly the amount of energy that can be concentrated at any specific moment by the heliostat field. Of the light crossing the field, a fraction impacts the heliostats and is reflected towards the receiver. Only a part of this light will actually reach the receiver aperture. The rest will either be lost to the atmosphere (scattering) or miss the receiver aperture (spillage).

Upon reaching the receiver aperture, some of the sunlight and the ensuing heat is lost back to the environment, and part of it is transferred to the molten salt flowing in the receiver tubes. This molten salt flows to the hot storage until it is needed to drive the powerblock. While it remains stored in the insulated storage, the molten salt loses energy progressively to the environment through various loss processes.

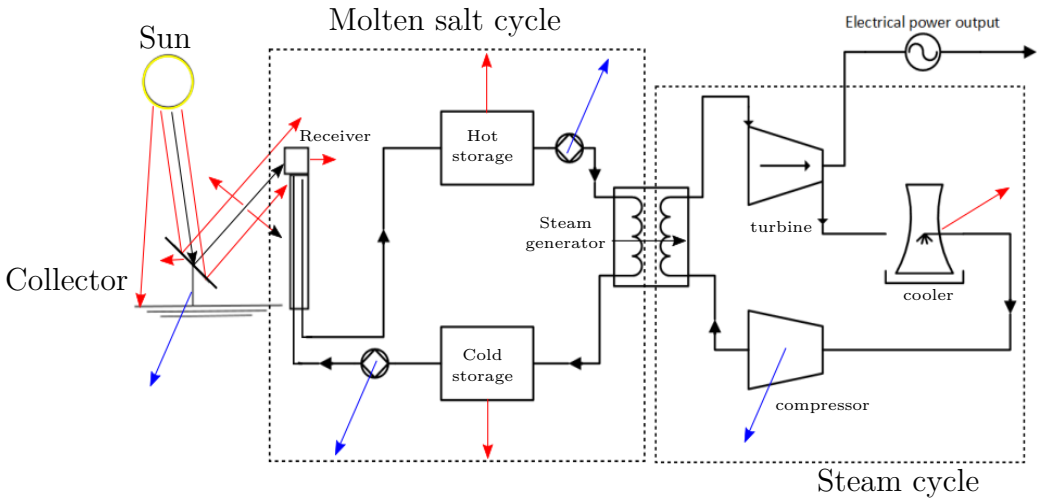

Figure 2.1 Energy flow representation.

When energy is required at the powerblock, molten salt is pumped in the heat exchanger shells while water flows in the tubes. Heat is transferred from the molten salt to the water, turning it into superheated steam, and we assume that no losses occur to the exterior. Therefore, all thermal energy is conserved. The then cooled molten salt is sent to the cold storage, where it will remain and sustain heat losses until it flows through the receiver again.

The heat transferred to the powerblock is used to produce superheated steam to drive the steam turbine to generate electricity. Energy is thus extracted from the steam as electric power and as mechanic losses in the turbine. Not all the thermal energy transferred to the steam is used by the turbine and the low pressure steam exiting the turbine must be cooled and condensed in order to be pumped again in the heat exchanger.

2.1.2 Software dynamics

The power plant model operates as three main systems interacting with each others: the heliostat field, the molten salt cycle, and the powerblock. Thus the molten salt cycle is central to the operation of the power plant because it is through it that the energy collected from the heliostat field is fed to the powerblock. At all time, the power plant model is fed two data types from external models: the heliostat field receives information from the solar model which allows it to determine its own performance, and the powerblock system receives information from the demand model, that dictates how much power it should be seeking to generate. There is no direct interaction between the heliostat field model and the powerblock, or, as a result, between the heliostat field's performance and the demand. This is symptomatic of the use of a heat storage system, of which the objective is to isolate the turbine from solar transients.

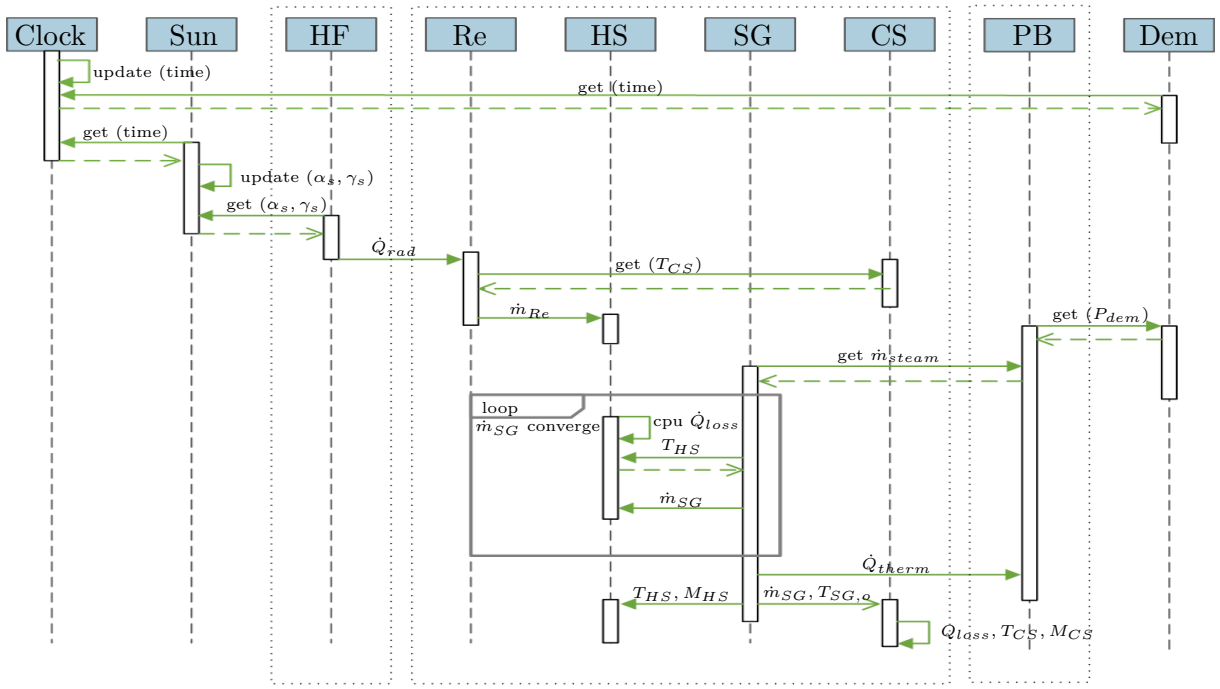

Figure 2.2 Sequence diagram for the simulation of one time interval.

Figure 2.2 shows the sequence operated for each time step of the simulated interval. First, the sun's position angles are updated to match the solar hour. The sun position is used by the heliostat field model (HF) to adjust the orientation of each heliostat so that they keep reflecting light towards the receiver aperture. The performance of the heliostat field for this arrangement is then computed, and the amount of energy Q_{rad} concentrated on the receiver aperture is fed to the central receiver model (Re).

The receiver model then computes the rate at which molten salt flows $\dot{m}_{Re}$ through it and is sent to the hot storage (HS) unit. This amount is computed as a function of the receiver's design parameters, the power received from the collector field and the temperatures of both the cold storage (CS) and the receiver outlet design point.

The demand model (Dem) instructs the powerblock model (PB) of the power it needs to generate for this time interval. The latter determines the steam rate $\dot{m}_{steam}$ necessary to drive the turbine accordingly. Using this steam rate, the hot storage temperature T_{HS} and hard coded inlet and outlet steam conditions required for the turbine to operate, the steam generator model (SG) determines the rate of molten salt $\dot{m}_{SG}$ flowing through the heat exchanger shells. For some storage conditions and design parameters, the temperature of its molten salt inventory can vary quickly. The steam generator model uses the arithmetic average of the storage temperature at the beginning and end of the time interval. Since the

stored temperature directly influences the amount of molten salt that needs to be drained by the steam generator to achieve its desired heat transfer rate, and since the amount of mass removed from the storage impacts the rate of heat losses during this time interval, the molten salt rate and hot storage temperature are found through an iterative procedure.

Once the steam generator model is done determining the heat transfer conditions, the rate of energy transferred $\dot{Q}_{therm}$ is confirmed to the powerblock. Using the molten salt flows determined by both the receiver and the heat exchanger, both storage units final statuses (inventory M and temperature) are adjusted.

2.2 System components models

2.2.1 Optical concentrator

The optical concentrator consists in an array of sun tracking mirrors, called heliostats, used to reflect sunbeams onto the central receiver. The following section describes the model used to represent the collector field and calculate the instantaneous power output that can be expected from it for a given set of design parameters. Table 2.1 below gives the list of design parameters that directly impact the performance of the heliostat field. Figure 2.3 shows the

Table 2.1 List of design parameters for the heliostat field.

Symbol	Definition	Unit
ϕ	latitude	deg
w	heliostats width	m
l	heliostats length	m
H_T	height of tower	m
N_h	number of heliostats on the field	-
θ_{fld}	angular width of the heliostat field on each side of the N-S axis	deg
R_{min}	minimum distance between heliostats and tower	m
R_{max}	maximum distance between heliostats and tower	m
H_a	Receiver aperture height	m
W_a	Receiver aperture width	m

definition of the input parameters that determine the field dimensions.

Sun radiation model

Since the heliostat field performance varies throughout the day as a function of the direction of the incident radiations from the sun, a model is needed to describe the sun's position

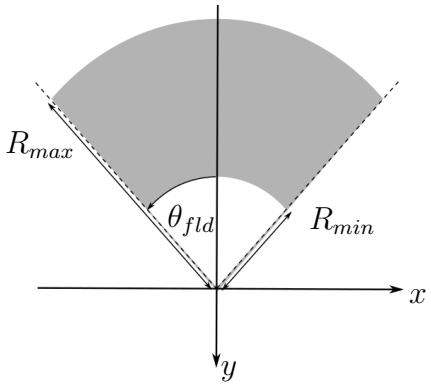

Figure 2.3 Heliostats field parameters definition.

relative to the field as a function of time.

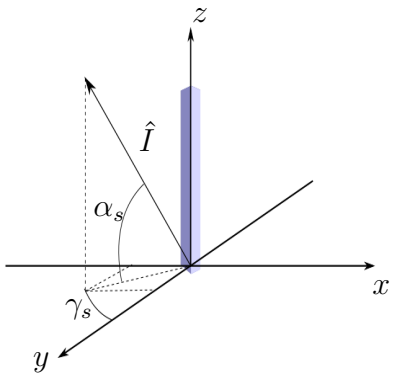

Figure 2.4 Solar azimuth and elevation angles and field axis definition.

The center of the solar disc is defined by the surface azimuth angle and the elevation (or incidence) angle [64], as depicted in Figure 2.4. Both angles are obtained using the equations below.

$$\begin{aligned} \delta =& 23.45 \sin\left(360\frac{284+n}{365}\right) \\ \sin\alpha_s =& \sin\phi\sin\delta + \cos\phi\cos\delta\cos\omega \\ \cos\gamma_s =& \frac{\sin\alpha_s\sin\phi - \sin\delta}{\cos\alpha_s\cos\phi} \end{aligned} \tag{2.1}$$

δ sun declination

α_s elevation angle of the solar disc center

γ_s azimuth angle of the solar disc center

n day of the year ($n = 0$ is January first)

ϕ location latitude

ω solar hour angle

With each of the angles used above using the conventions from Duffie and Beckman [19].

The sun shape is neglected and the sun itself is approximated as a point source. Because the sun is very far from the earth, radiations are approximated to be perfectly parallel and uniformly distributed on the surface of the field. The direct solar irradiance per unit surface at the Earth's surface (G_s) is approximated to be $1kW/m^2$ [55]. Clouds and atmospheric transmissivity variations in the atmosphere throughout the day are not considered.

These approximations tend to increase the performance of the field because radiations reflected from a perfectly flat heliostat would normally tend to diverge slightly between the heliostats and the receiver, and also because the apparent size and shape of the sun should cause a slight deviation for the beams originating from the periphery of the solar disc, causing increased spillage losses. For the sake of simplicity, these factors are nevertheless neglected.

Generating the heliostat field

When the simulator is launched, it first proceeds to build the heliostat field using the parameters provided by the user. This same heliostat field will then be used to calculate the energy inputed in the system at any hour of the day. Optimizing the layout of the heliostats is in itself a complex problem to solve, and many authors have attempted to tackle this problem in other works [11]. The eSolar company [47] proposes a simple layout of many small heliostats lined up on a rectangular grid. While this design does not necessarily achieve the best reflective aperture efficiency, it greatly facilitates the maintenance and cleaning process. Many currently operating power plants use a radially staggered arrangement, as it's been shown to give the most efficient use of a given reflective area [18, 12, 40]. Sanchez and Romero [46] propose a way to select the positions in the radially staggered grid and to depart from the grid arrangement by using the so-called Heliostat Growth Method (HGM) which increase the field efficiency by a few percentage points as compared to older layout strategies like that of the well known DELSOL software. More recently, Carriroza et al. [15] proposed a method for the optimization of the layout for heliostats of different sizes.

In the present work, a systematic approach proposed by Siala and Elayeb [51] to determine a radially staggered grid is used for a single size of heliostats and no attempt to further refine the layout is done. This determines the arrangement of the potential positions of the heliostats as a function of their sizes and tower height, in a way that ensures that there will be no blocking losses (the term "blocking" refers to the losses suffered when an heliostat stands between another heliostat and the receiver). The fact that there is no blocking between heliostats contributes to simplifying the evaluation of the field's performance, as will be

explained later in this section.

The first step in building the heliostat field consists in finding the coordinates of all the potential positions. The method proposed by Siala and Elayeb is used integrally and is therefore not described here. Figure 2.5 shows two examples of radially staggered grid layouts generated with this algorithm for identical heliostats sizes but different tower heights. The central receiver tower is located at (0,0).

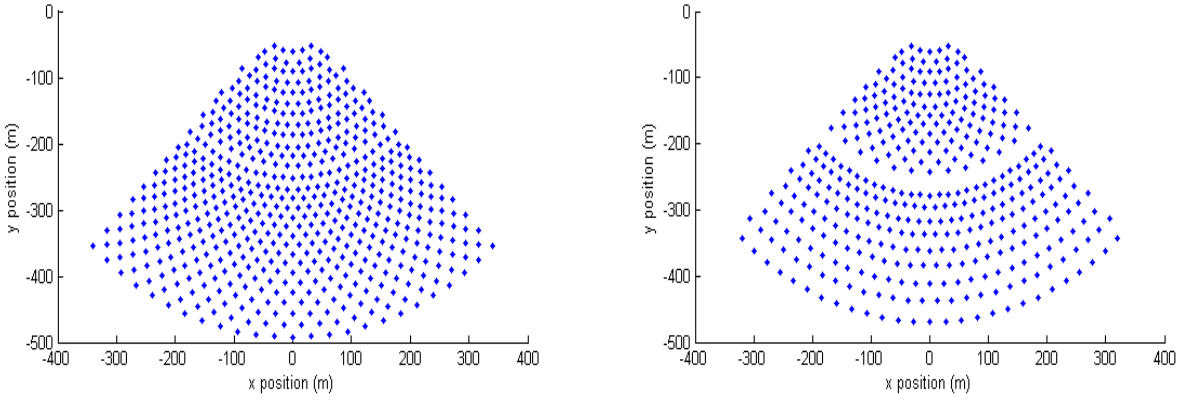

Figure 2.5 Examples of heliostat field layouts for 8x8 heliostats with a tower height of 120m on the left and 70m on the right.

Calculating heliostats efficiency

The model gives the user the possibility of specifying a maximum number of heliostats N_h. If N_h is inferior to the number of positions in the grid, the best individual heliostats will be selected, with regards to their respective efficiency.

The efficiency of a heliostat is determined by combining its cosine efficiency factor η_{cos}, the atmospheric attenuation sustained by light reflected from its position τ and proportion of reflected light that can get inside of the receiver aperture η_{spill}. Shadowing effects are not considered during this step, but will be accounted for when calculating the overall field's performance later on. The efficiency for one potential heliostat position h at any given moment is defined as

$$\eta_h = \tau_h \eta_{spill,h} \eta_{cos,h}. \tag{2.2}$$

The heliostats are assumed to be perfectly flat, leaving the reflected sun rays parallel to each others after the reflection. Thus the assumption is made that if the heliostats reflectivity is equal to 1, and no atmospheric attenuation losses are considered, the totality of radiations

reaching the heliostat also reaches the receiver. Note also that the shadow created by the tower itself is not considered.

The cosine efficiency η_{cos} is the ratio of the area of the reflective surface projected on a plane perpendicular to the incoming sunlight over its total reflective area.

With $\hat{I}$ defined as the unit vector pointing towards the center of the solar disc, and $\hat{R}_h$ the unit vector pointing from the central point of heliostat h to the aim point on the receiver, both vectors are given by the following equations [64]:

$$\hat{I} = (-\cos\alpha_s \sin\gamma_s, \cos\alpha_s \cos\gamma_s, \sin\alpha_s) \tag{2.3}$$

$$\hat{R}_h = \left(\frac{-x_h}{\sqrt{x_h^2 + y_h^2 + (H_T - z_h)^2}}, \frac{-y_h}{\sqrt{x_h^2 + y_h^2 + (H_T - z_h)^2}}, \frac{H_T - z_h}{\sqrt{x_h^2 + y_h^2 + (H_T - z_h)^2}} \right). \tag{2.4}$$

Let θ_h be the angle between $\hat{I}$ and $\hat{R}_h$, and let $\overrightarrow{A}_h$ be the vector normal to the reflective surface of heliostat h, then the angle between $\overrightarrow{I}$ and $\overrightarrow{A}_h$ is given by [64]

$$\theta_h = \frac{1}{2} \arccos(\hat{I} \cdot \hat{R}_h),$$

with the resulting cosine efficiency being

$$\eta_{cos,h} = \frac{A_{proj,h}}{A} = \cos\theta_h. \tag{2.5}$$

This gives the cosine efficiency for a given value of α_s and γ_s, which both vary with time. Thus the best heliostats are found by averaging the cosine efficiency for all sunny hours.

The spillage efficiency η_{spill} is the proportion of reflected light that can geometrically enter the receiver aperture. This is what connects the receiver aperture dimensions to the choice of heliostats dimensions. $(\eta_{spill})_h$ is defined as the ratio of the intersection area of the aperture and heliostat h as projected on a plane perpendicular to $\hat{R}_h$

$$\eta_{spill,h} = \frac{A_{proj,h} \cap A_{proj,re}}{A_{proj,h}}. \tag{2.6}$$

Like for the cosine efficiency, this ratio varies with time as the heliostats orientation changes.

Atmospheric attenuation τ_h of the radiations occuring between each heliostat and the central receiver aperture is calculated for a clear day with a visibility of 23km. The equation used to account for atmospheric losses is given by [8]:

$$\tau_h = 1 - (0.29544 + 15.22128\|S_h\| - 1.8598\|S_h\|^2 + 0.15182\|S_h\|^3), \tag{2.7}$$

where S_h is the slant range separating the center point of heliostat h and the aim point on the receiver, in km, and τ_h is the atmospheric transmittance from this heliostat. All light reflected form a single heliostat h is assumed to come from a distance equal to S_h and the difference of distance crossed between different points of the heliostat is neglected.

The best heliostats are found by averaging their total efficiency over the whole simulation period:

$$Avg(\eta_h) = \frac{\tau_h \int_{t_{sunrise}}^{t_{sunset}} \eta_{cos,h}(t)\eta_{spill,h}(t)dt}{t_{sunset} - t_{sunrise}}. \tag{2.8}$$

Figure 2.6 shows two examples of heliostat field selections for identical grid layouts but different receiver aperture sizes. The two examples show a selection for a field containing 700 heliostats, in red, chosen from the 1960 possible positions in the radially staggered grid. We see that the narrower receiver aperture, spillage is an important factor and causes the algorithm to select positions closer to the centerline, whereas the wider receiver makes spillage negligible, letting cosine efficiency and atmospheric attenuation dictate the selection.

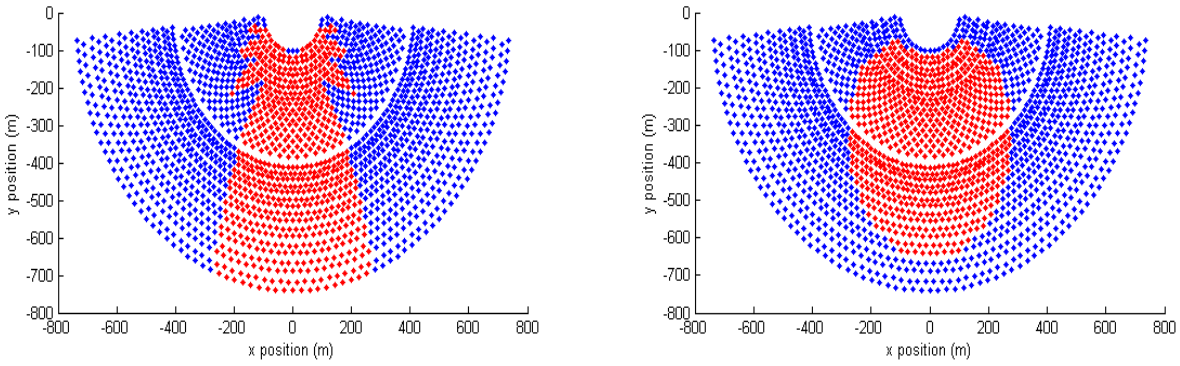

Figure 2.6 Examples of positions selection after the efficiency evaluation, with a receiver aperture width of 3 m on the left and 15 m the right.

Evaluating the field's power output

Once the heliostat field has been generated, its hourly power output is determined. Because of the previously mentioned assumptions of no-aiming or tracking error, perfectly flat heliostats, and sunlight parallelism, though, the trajectory of sunbeams need not be computed between the heliostats surfaces and the receiver. Thus computing the total energy transmitted to the receiver simplifies to calculating how much energy reaches each heliostat, and correcting for their respective atmospheric losses and spillage factors.

Evaluating the total energy reaching the heliostats is done in two steps. First, the total direct irradiance on the field is calculated. This is done by considering the field as a control volume, and evaluating the radiation flux crossing its surface. The solid considered has the shape of a share of an isometric pie chart, with an angular width equivalent to $2\theta_{field}$, a height equal to the heliostats length l and a radius equal to R_{max} (see Figure 2.7).

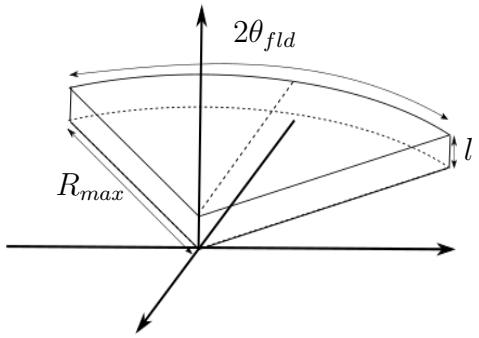

Figure 2.7 Field shape approximation.

The entering flux integral is performed over each faces bounding the field. The second step is to break down this total amount of energy in a finite amount of sunrays, each carrying an identical fraction of the total energy crossing the field, to distribute them randomly using a uniform distribution on the field and to calculate the amount of energy impacting the surface of each heliostat.

A number of sun rays proportional to the field's surface area is generated and distributed randomly on the field, uniformly. This is done by generating a random target located inside the volume of the field for every sunray. The number of sunrays intercepted by each heliostat is stored. For each heliostat, the amount of power transmitted to the central receiver is then calculated as below:

$$P_h = \rho \tau_h \eta_{spill,h} \frac{N_h G_s S_{field}}{N_r}. \tag{2.9}$$

P_h power delivered to the receiver from heliostat h

N_h number of sunrays intercepted by heliostat h

ρ_h heliostats reflectivity

G_s solar irradiance (W/m^2)

τ_h atmospheric transmittance between heliostat h and the receiver

N_r total number of sunrays distributed on the field

S_{field} Field surface area, (m^2)

Thus the total power concentrated to the receiver is the sum of the power reflected by each heliostat,

$$P_{total} = \sum_{h=1}^{N_h} P_h. \tag{2.10}$$

Figure 2.8 shows the resulting concentrated solar energy throughout a 24 hours period for a field using a 120m high tower with a 10mx10m receiver aperture. Each configuration tested has the same total reflective surface but uses heliostats of different sizes or placements. For scenario c), the field dimensions were reduced as to force the algorithm to use every available positions instead of selecting them as a function of their overall efficiency. The curves show the radiative power concentrated on the receiver aperture by supposing perfect heliostats reflectivity.

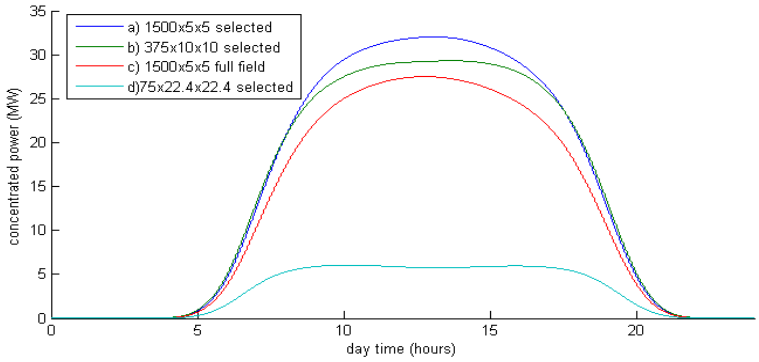

Figure 2.8 Examples of the heliostat field power output for a 37500 m^2 reflective surface with various heliostats distribution and sizes. a) uses 1500 5mx5m heliostats selected from 4100 positions, b) uses 375 10mx10m heliostats selected from 970 positions, c) uses 1500 5mx5m heliostats with imposed positions, and d) uses 75 22.4mx22.4m heliostats selected from 273 positions

Sun Rays Interception In order to determine which heliostats are impacted by each sunray (if any), all heliostats position and all sunrays target points are projected onto a single plane that is perpendicular to the incoming solar radiation.

The baseline coordinates system are cartesian coordinates, with the origin placed at the bottom of the receiver tower, the x axis pointing due East, the y axis pointing due South, and the z axis pointing directly upwards.

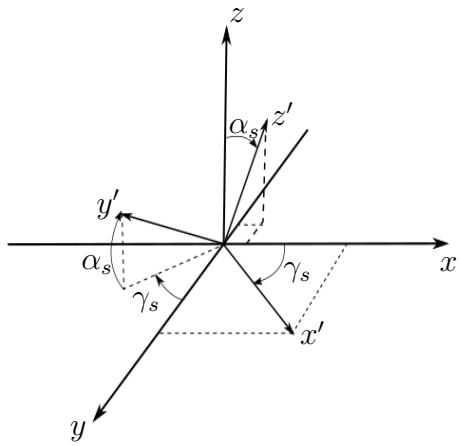

Figure 2.9 Rotated coordinates system.

A rotated axis system is then obtained as showed in Figure 2.9, by placing the new y' axis pointing directly towards the center of the solar disc. This is done by first rotating the frame around the z axis by an angle equivalent to the Sun azimuth, and then by rotating the frame around its x' axis by an angle equivalent to the Sun's elevation. By doing so, we obtain the following definition of the new unit vectors:

$$\begin{aligned}
\hat{x'} &= (\cos\gamma_s, \sin\gamma_s, 0) \\
\hat{y'} &= (-\cos\alpha_s \sin\gamma_s, \cos\alpha_s \cos\gamma_s, \sin\alpha_s) \\
\hat{z'} &= (\sin\alpha_s \sin\gamma_s, -\sin\alpha_s \cos\gamma_s, \cos\alpha_s)\,.
\end{aligned} \tag{2.11}$$

Thus the heliostat field as seen from the sun is the view of the $X'Z'$ plane. In order to verify the collision of the sunrays with each heliostat, the position of the top left, top right and bottom left corners of each heliostat are also projected onto the new coordinate system. Once this is done, each sunray will be tested against each heliostat, starting with the heliostat with the highest value of y'_h. Each sunray can only be intercepted once.

Let $\overrightarrow{TL}_h, \overrightarrow{TR}_h$ and $\overrightarrow{BL}_h$ be the respective position of the top left, top right and bottom left corners of heliostat h as seen from the side of its reflective surface. Let also $\overrightarrow{TL'}_h, \overrightarrow{TR'}_h, \overrightarrow{BL'}_h$ be their projection on the $X'Z'$ plane and $\overrightarrow{Tgt'}$ be the projection of a sunray target onto the same plane.

Let $\overrightarrow{A} = \overrightarrow{Tgt'} - \overrightarrow{TL'}$, $\overrightarrow{B} = \overrightarrow{TR'} - \overrightarrow{TL'}$, and $\overrightarrow{C} = \overrightarrow{BL'} - \overrightarrow{TL'}$. If $\overrightarrow{B}$ and $\overrightarrow{C}$ are linearly

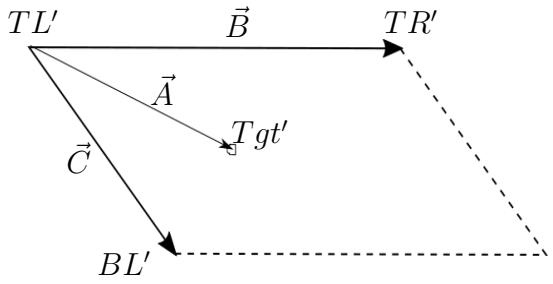

Figure 2.10 Definition of $\vec{A}, \vec{B}, \vec{C}$.

independent, that is, if the area of the corresponding heliostat projected onto the plane perpendicular to the radiations is not zero, then $\overrightarrow{A}$ can be expressed as a linear combination of the two.

$$\vec{A} = u_1\vec{B} + u_2\vec{C} \tag{2.12}$$

The sunray is intercepted by the heliostat if the target is found within the parallelogram delimited by $\overrightarrow{B}$ and $\overrightarrow{C}$. Thus a sunray will be considered to have been intercepted by heliostat h if $u_1, u_2 \in [0, 1]$ and if $\det([\overrightarrow{B}\,\overrightarrow{C}]) \neq 0$. This is verified using the following equations:

$$\begin{aligned} \det([\vec{B}\vec{C}]) &= B_1C_2 - B_2C_1 \\ u_2 &= \frac{A_2B_1 - A_1B_2}{\det([\overrightarrow{B}\,\overrightarrow{C}])} \\ u_1 &= \frac{A_1 - u_2C_1}{B_1}. \end{aligned} \tag{2.13}$$

2.2.2 The Central Receiver

A variety of central receiver systems have been tested over the past decades [6, 26]. Some authors have worked on optimizing the different concepts of central receivers alone. In general, these approaches consist in optimizing the receiver with regards to some specific design parameters and with the intent of reaching the best absorption rate. Steinfeld and Schubnell [53] propose a semi-empirical approach to optimizing the aperture size of a cavity receiver. Segal and Epstein [50] worked on the optimization of the working temperatures of a central receiver using a secondary reflector.

The type of receiver chosen here is a molten salt cavity receiver. This concept of receiver is directional, using a heat exchanger located in a cavity of which the aperture is closed by

glass. Instead of having the sunlight hit the absorbing surface directly in the open air, light goes through a glass and hits a wall of low reflectivity in which the tubes are embedded. Trapping light inside the receiver instead of having it be converted to heat in the open air reduces convective and re-radiation losses and increases the temperature at the tubes surface, causing increased heat transfer rates to the fluid. The simplified model for a cavity receiver with molten salt and tube exchanger visible on Figure 2.11 and proposed by Li et al. [37] is used. [1] Table 2.2 shows the list of design parameters for the central receiver.

Table 2.2 List of design parameters for the central receiver unit.

Symbol	**Definition**	**Unit**
W_a	aperture width	m
H_a	aperture height	m
N_{tubes}	number of tubes	-
D_{in}	tubes inner diameter	m
D_o	tubes outer diameter	m
d	thickness of insulation	m

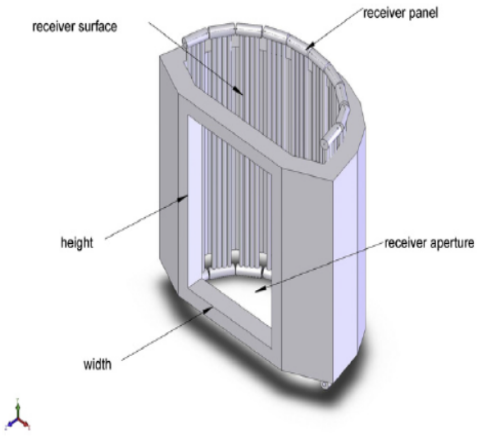

Figure 2.11 Central receiver model concept [37].

Li et al. use a constant heat input to the fluid and use the equations of the model to deduct the incident radiative energy necessary to achieve their desired heat transfer rate of 100kW. The efficiency of the receiver is then computed as the ratio of the input energy and the energy absorbed by the molten salt. In the case of the current model, the radiative energy input is

1. Figure 2.11 is reprinted from Renewable Energy, Vol 35, Xin Li and Weiqiang Kong and Zhifeng Wang and Chun Chang and Fengwu Bai, *Thermal model and thermodynamic performance of molten salt cavity receiver*, P. 983, 2009 Elsevier Ltd., with permission from Elsevier. [37]

provided by the heliostat field model described above for every time step. Equation 4 from Li et al. is re-organized in order to determine the surface temperature of the receiver tubes.

$$T_{Re,sur} = \dot{q}_{in}\left(\frac{D_0}{D_{in}h_{ms}} + \frac{D_0}{2k_{tubes}}\ln\frac{D_o}{D_{in}}\right) + T_{ms} \tag{2.14}$$

D_o, D_{in} outside and inside diameters of the tubes

h_{ms} convection heat transfer coefficient of molten salt W/m^{2}K

k_{tubes} thermal conductivity of the tubes, W/(mK)

$T_{Re,sur}$ absorbing surface temperature, K

T_{ms} molten salt temperature, K

$\dot{q}_{in}$ incident radiation over heat transfer area W/m^2

The surface temperature is assumed to be the same over the entire absorbing surface, and molten salt temperature is considered as the average temperature of inlet and outlet temperatures. $T_{Re,sur}$ is used to determine the overall energy loss $\dot{Q}_{loss}$ through re-emission, convection and conduction. The remaining energy $\dot{Q}_{abs}$ is used to determine the incident molten salt flow that can be heated to the design point temperature for a given radiation energy input.

Because Eq.2.14 involves h_{ms} and the later involves $\dot{m}_{ms}$, these values are determined through an iterative process until the receiver efficiency $\eta_{Re} = \dot{Q}_{abs}/\dot{Q}_{in}$ reaches convergence. Figure 2.12 illustrates this process.

While Li et al. propose to use the Dittus-Boelter equation to determine the Nusselt number Nu_D in the determination of h_{ms}, this equation is best suited for Reynold numbers Re above 10,000, and many configurations of the receiver or values of q_{in} will lead to mass flows with lower Re. We use instead the more precise equation for Nu_D [29]

$$Nu_D = \frac{(f/8)(Re_D - 1000)Pr}{1 + 12.7(f/8)^{1/2}(Pr^{2/3} - 1)}, \tag{2.15}$$

where f is the friction factor and is obtained through Equation 8.21 of [29] for $3000 \leq Re_D \leq 5 \times 10^6$:

$$f = (0.790\ln Re_D - 1.64)^{-2}. \tag{2.16}$$

For $Re \leq 3000$ laminar flow is assumed and Nu_D is set to 4.36 for smooth tubes. In the process of determining Re_D, the properties of the molten salt have to be known. The values

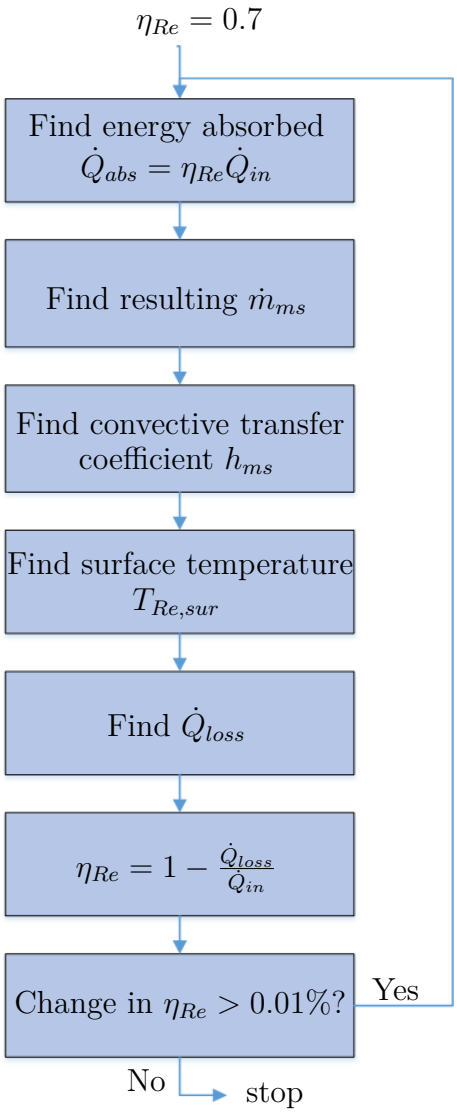

Figure 2.12 Receiver efficiency computation process.

for the melting point and heat capacity of the $NaNO_3 - KNO_3$ mixture are assumed constant and obtained from the Department of Metallurgical and Materials Engineering of the University of Alabama [44]. The fluid viscosity is taken from Table 72b of [30] for viscosity and computed as a function of T_{ms}. Because Table 72b gives coefficients for a finite set of concentrations which does not include the 60% mass $NaNO_3$, coefficients for the 50%, 75% and 100% molar concentrations were used to derive a second degree polynomial approximation for each coefficient for the viscosity polynomial, as a function of mass concentration.

Once q_{abs} has been determined we find the value of $\dot{m}_{ms}$ using the heat capacity of the molten salt and the temperature differential between the receiver outlet's design point conditions and the current cold storage temperature:

$$\dot{q}_{abs} = c_p \dot{m}_{ms}(T_{Re,o} - T_{CS}). \tag{2.17}$$

As a starting point for the iteration process $\eta_{Re} = 0.7$ is assumed and $\dot{m}_{ms}$ is determined accordingly.

Modeling the energy losses

Li et al. [37] propose a simple calculation model for every type of losses, that is, reflection losses $\dot{q}_{ref}$, emission losses $\dot{q}_{em}$, convection losses $\dot{q}_{conv}$ and conduction losses $\dot{q}_{cond}$. For each losses, a half-cylindre shape is assumed for the interior of the cavity.

Reflective losses $\dot{q}_{ref}$ are the only losses that don't depend on $T_{Re,sur}$. The reflectivity of the surfaces are assumed constant with temperature. Reflective losses are removed from $q_i n$ before $T_{Re,sur}$ is calculated and do not change during the iterative process.

$$\dot{q}_{ref} = F_r \dot{q}_{in} \rho_{Re,sur} \tag{2.18}$$

with $F_r = A_a / A_{Re,sur}$ and $\rho_{Re,sur}$ the reflectivity of the surface. Note that F_r is the view factor of the aperture as seen from the receiver absorbing surface, thus the reflection is here considered perfectly diffuse and equal in all directions from any point of the surface. The reflective losses are merely the part of the incoming radiation flux that is reflected and that then leaves the receiver through the aperture.

Emissive losses $\dot{q}_{em}$ are considered as the radiations emitted from the surface to the ambiant air outside the receiver, through the aperture. The stainless steel tubes that cover the surface of the cavity are coated with an absorbing coating for which we make a quasi-blackbody assumption. The emissivity of the absorbing surface is thus assumed to be $\epsilon_{Re,sur} = 0.95$. The exact model from [37] is used:

$$\dot{q}_{em} = \epsilon_{avg} \sigma (T_{Re,sur}^4 - T_{atm}^4) A_{Re,sur} F_r,$$

$$\epsilon_{avg} = \frac{\epsilon_{Re,sur}}{\epsilon_{Re,sur} + (1 - \epsilon_{Re,sur}) F_r},$$

$$F_r = \frac{A_a}{A_{Re,sur}}.$$

σ is the Stefan-Boltzmann constant ($5.67 \times 10^{-8} W/m^2 K^4$)

Convective and conductive heat losses $\dot{q}_{conv}, \dot{q}_{cond}$

Kribus [35] establishes that at high operating temperatures ($T_{Re,sur} \geq 1000^{\circ}C$), emissive losses dwarf other losses. In the present case, it is entirely possible that the operating temperatures may sit well below the thousand $^{\circ}C$. Li et al. [37] also establish that the conductive heat losses are the smallest losses. Thus in the present model, conductive losses to the tower structure are neglected. However, conductive losses through the receiver's back to the atmosphere, happening via convection and radiative losses to the outside surface of the insulation, are considered.

Assuming an arbitrary $7m/s$ wind speed (around world average on land) at ambient temperature $T_{atm} = 25^{\circ}C$, natural convection is neglected. Forced convective losses are computed using Hilpert's empirical correlation for Nusselt's number, as quoted on p.426 of [29], for a cylindrical surface standing perpendicular to a flow, with standard atmospheric conditions:

$$\bar{Nu}_D \equiv \frac{\bar{h}D}{k_{atm}} = CRe_D^m Pr^{1/3}. \tag{2.19}$$

For standard conditions, $Pr = 0.707$ and $k_{atm} = 0.0263w/mK$. With values for C and m available in Table 2.3 below

Table 2.3 Values of parameters C and m in Hilpert's correlation for expectable values of Re_D.

Re_D	C	m
4 - 40	0.911	0.385
40 - 4000	0.683	0.466
4000 - 40 000	0.193	0.618

The insulation material is mineral wool with properties identical to those used for the heat storage tanks. The energy losses associated with convection can be modeled with the electrical circuit analogy using a resistance for a semi-circular conductor and then a convection resistance with a convection coefficient h determined with Equation 2.19.

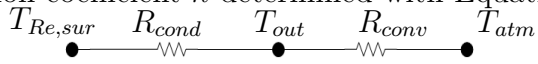

Figure 2.13 Electrical circuit analogy for receiver convection.

Figure 2.13 shows the analogous circuit for exterior convection and Eq. 2.20 gives the corresponding expression of the heat flux. External radiation is not considered.

$$\dot{q}_{conv} = \frac{T_{Re,sur} - T_{atm}}{\frac{W_{Re,a}/2}{k_{insul}H_{Re,a}} \ln \frac{(W_{Re,a}/2)+d_{Re}}{W_{Re,a}} + \frac{1}{h_{atm}\pi H_{Re,a}(W_{Re,a}+d_{Re})/2}}. \tag{2.20}$$

Figure 2.14 shows the behavior of the receiver for four different sizes of their aperture receiving the same incident radiation. The apertures area range from $50m^2$ to $500m^2$ with incident radiations ranging from 5 to 1200 MW_t. We see that heat losses are very high for the smallest receiver when the influx reaches high values. This is due to the fact that the incident radiative power per unit area becomes very high, causing excessive temperatures (well above $1000^{\circ}C$), meaning that this would be a poor choice of receiver design for a high power application.

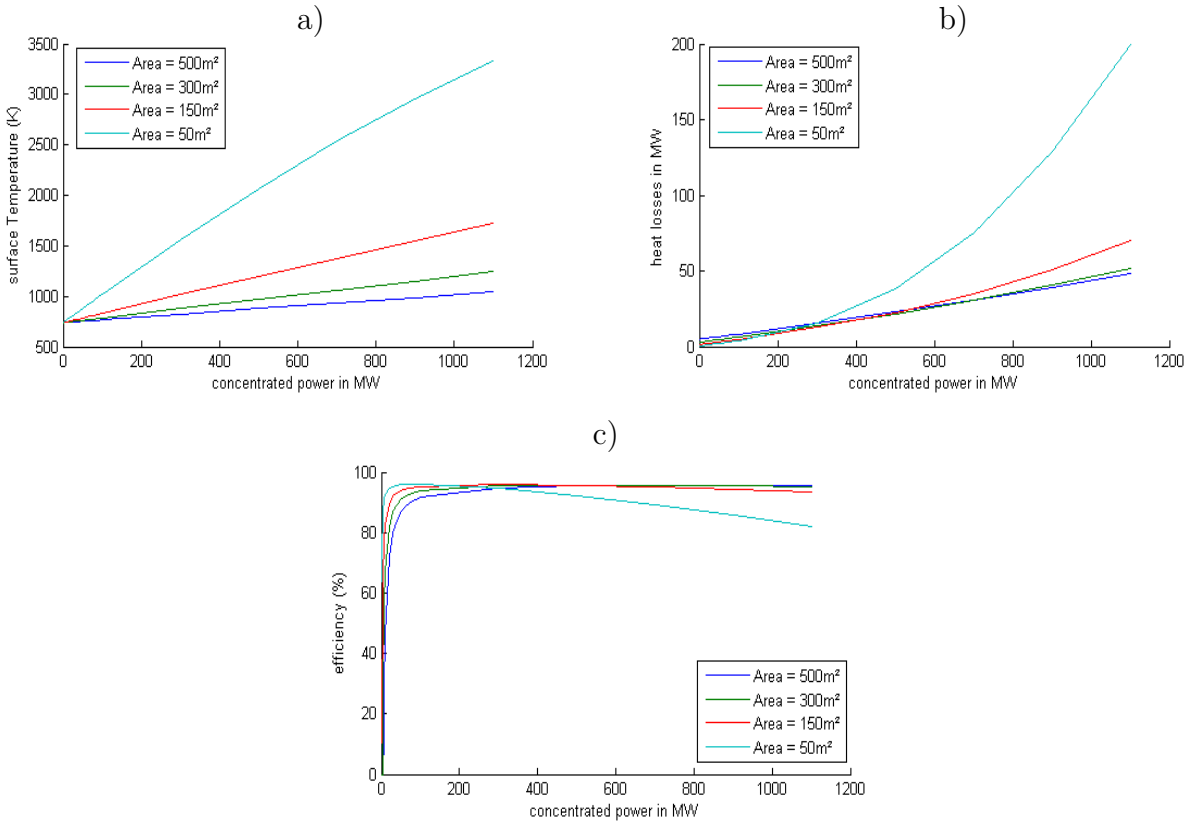

Figure 2.14 Receiver surface temperature (a) , heat losses (b) and efficiency (c) as a function of the incident power input in MW for different area of the receiver aperture.

2.2.3 The Cold and Hot Storage Units

The thermal storage units consist of large insulated tanks in which excess molten salt is kept until it is required. The tanks are cylindrical and have an inner wall made of stainless steel and an external layer of insulation wool. Table 2.4 shows the list of design parameters that define the thermal storage.

The storage model tracks the molten salt inventory m_{stor} contained in the tank at any moment along with the temperature of this inventory T_{stor}. For every time interval of the simulation,

Table 2.4 List of design parameters for the thermal storage units.

Symbol	Definition	Unit
d	tanks insulation thickness	m
H	height of the interior of the storage tanks	m
D	diameter of the interior of the storage tanks	m

m_{stor} and T_{stor} are determined for both storage units according to Eqs. 2.21.

$$\begin{aligned} m_{stor}(t_i) &= m_{stor}(t_{i-1}) + (\dot{m}_{in}(t_i) - \dot{m}_o(t_i))(t_i - t_{i-1}) \\ U_{stor}(t_i) &= U_{stor}(t_{i-1}) + (\dot{U}_{in}(t_i) - \dot{U}_o(t_i))(t_i - t_{i-1}), \end{aligned} \tag{2.21}$$

with

$$\begin{aligned} \dot{U}_{in}(t_i) &= \dot{m}_{in}(t_i) u_{in}(t_i) \\ \dot{U}_o(t_i) &= \dot{m}_o(t_i) u_o(t_i) + \dot{Q}_{loss} \end{aligned}$$

Where t is the time index, u is the internal energy per unit mass of molten salt, U is the internal energy and $\dot{Q}_{loss}$ is the rate of thermal losses.

A simplified model for the storage tank is used to determine the value of the heat loss Q_{loss} as a function of the level of the storage and its temperature. In order to do so, we use the heat loss model proposed by Zaversky et al. [63]. The work from which the model was taken includes many mechanisms of heat losses, including natural convection inside the empty space of the tank above the molten salt when the tank is not full. In their analysis, though, Zaversky et al. show that natural convection inside the tank amounts to a very small portion of the losses. In the current work, we ignored convection inside the tank. Figure 2.15 shows a schema of the tank with the different channels of thermal losses, along with the definition of the design parameters. The thickness of the insulation is the same for both the tank's ceiling and its wall.

As Figure 2.15 shows, there are three channels of thermal losses from the molten salt when the tank is not at full capacity: conduction through the tank's floor, conduction through the wetted part of the cylindrical wall, and radiation from its top surface to the ceiling and the non-wetted part of the cylindrical wall.

Because a small heat transfer rate is assumed from the hot tank to the outside ambient air, homogeneous temperature is assumed and no natural convection occurring inside the molten salt is considered. The mass of molten salt stored is considered as a solid body with uniform temperature, losing energy through means of conduction through the cylindrical wall and

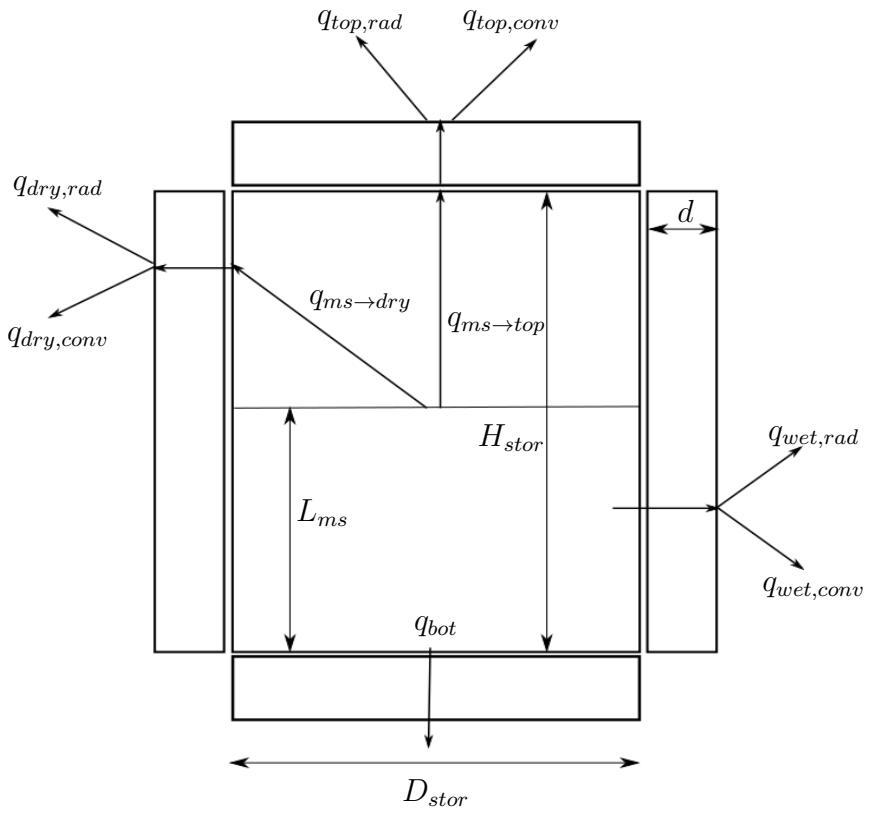

Figure 2.15 Thermal storage model parameters definition and loss processes.

the bottom of the tank, and radiation from its top surface to the remainder of the tank's non-wetted surface. Uniform temperatures are assumed on each of the tank's inner and outer surface subdivisions, that is, the wetted and non-wetted parts of the cylindrical wall, and the top surface.

In order to maintain atmospheric pressure inside the tank, there has to be some air filling the upper part of the tank when it isn't full. Thus if the air is assumed to reach the same temperature as the molten salt inside the tank, energy is transferred to it from the molten salt and this energy is lost when the level of the tank rises and air has to be evacuated from the tank. Because of the air's small volumetric energy density compared to the molten salt, this factor is not considered in the model.

From the outside surface of the tank, heat is lost to the atmosphere via convection and radiation. For the cylindrical wall, we assume that there is no conduction vertically and we treat the wetted and non-wetted parts of the wall as two different surfaces with each their own inside and outside surface temperature. Thus the relative importance of each of the loss processes is influenced by the level of molten salt in the tank. Figure 2.16 shows the circuit analogy used to determine the thermal resistances for the various loss processes.

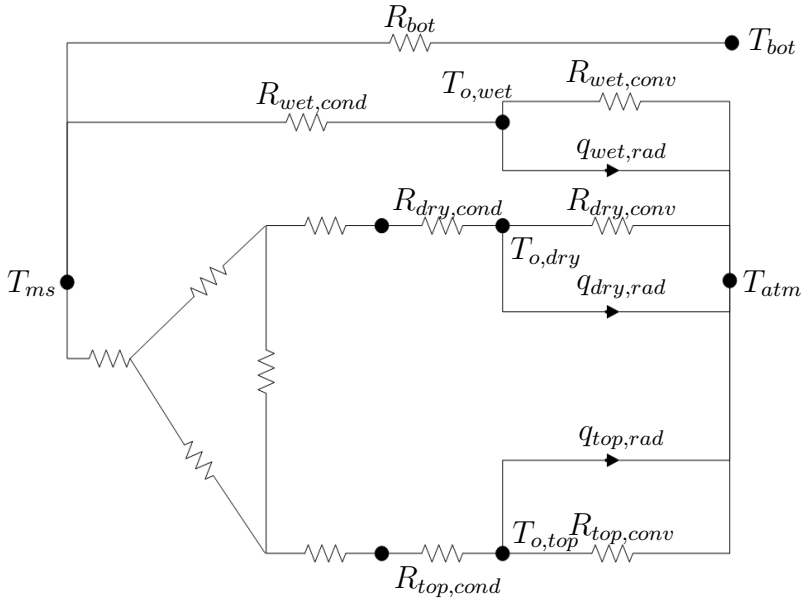

Figure 2.16 Thermal storage circuit analogy.

The total heat loss rate is the sum of the heat loss rates in each branch of the parallel circuit, which can all be calculated independently by assuming a constant heat rate during the time interval.

Outside surface losses

Zaversky et al. [63] include both natural and forced convection for the outside losses calculation. For the sake of simplicity, only forced convection is considered here and windspeed is assumed to be constant at $7m/s$, so that the convective coefficient is easily determined and not a function of the surface temperature.

Again using Hilpert's correlation, Nusselt's number and the average convection coefficient are found using Equation 2.19 and coefficients from Table 2.3.

For both radiative and convective heat transfers happening from the cylindrical part of the tank's exterior, two regions of potentially different temperature will be considered. The cylindrical surface will be divided into two regions at a height corresponding to the molten salt level. Finally, the influx of heat from sunlight to the exterior of the tank is not considered.

The same heat transfer mechanisms are used for the top of the tank. The correlations provided by [63] as quoted from [16] for Nusselt's number are used:

$$Nu = \frac{hL}{k} = 0.664 Re^{1/2} Pr^{1/3} \quad Re \leq 5 \times 10^5$$
$$Nu = \frac{hL}{k} = 0.037 Re^{4/5} Pr^{1/3} \quad 0.6 \leq Pr \leq 60 \text{ and } 5 \times 10^5 \leq Re \leq 10^7.$$

Wetted wall losses $\dot{q}_{wet}$

Conduction through a finite cylinder is used [29].

$$\dot{q}_{wet} = \frac{T_{ms} - T_a}{R_{tot}} = UA(T_{ms} - T_a) \tag{2.22}$$

$$UA = \frac{2\pi r_{in}(m_{ms}/\rho_{ms}\pi r_{in}^2)}{\left(\frac{r_{in}/2}{k_{ss}} \ln \frac{r_{in}+t_{ss}}{r_{in}} + \frac{r_{in}}{k_{insul}} \ln \frac{r_{in}+t_{ss}+d}{r_{in}+t_{ss}} + \frac{r_{in}}{(r_{in}+t_{ss}+d)h_a}\right)} \tag{2.23}$$

Tank bottom losses $\dot{q}_{bot}$

The bottom of the tank is laid on a thick plate of concrete floor crossed by air ducts to keep it from reaching high temperatures (high enough to degrade the concrete foundation). Zaversky et al. [63] assume a constant temperature T_{floor} of $90^{\circ}C$ for the concrete floor, thus avoiding the laborious calculations of heat dispersion through the ground. Because a constant temperature condition is applied for both sides of the tank's bottom wall, simple constant temperature conditions are assumed and the heat transfer rate $\dot{q}_{bot}$ is found by means of simple plane wall conduction analysis.

$$\dot{q}_{bot} = \frac{\pi(D/2)^2(T_{ms} - T_{floor})}{\frac{t_{ss}}{k_{kk}} + \frac{d}{k_{insul}}} \tag{2.24}$$

Radiative heat losses $\dot{q}_{top}, \dot{q}_{dry}$

Radiative losses from the surface of the molten salt have to be treated simultaneously for both surfaces. $\dot{q}_{top}$ refers to the losses occuring from the inner top surface and $\dot{q}_{dry}$ the losses occuring to the non-wetted part of the cylindrical wall.

In order to find the amount of energy leaving the tank by conduction, the temperatures of both surfaces have to be determined. Figure 2.17 shows the circuit analogy for both surfaces, where $\dot{q}_{in}$ is the sum of the incident radiation from the two other surfaces, and $\dot{q}_{em}$ the sum of the radiation emitted towards those two surfaces.

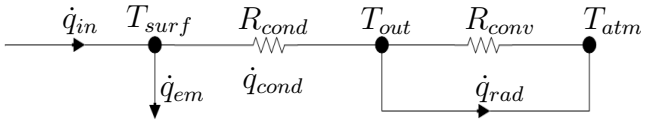

Figure 2.17 Radiative heat losses calculation.

Because the temperature of either surface is dependent on the other's, T_{dry} and T_{top} are found through an iterative process represented in Figure 2.18.

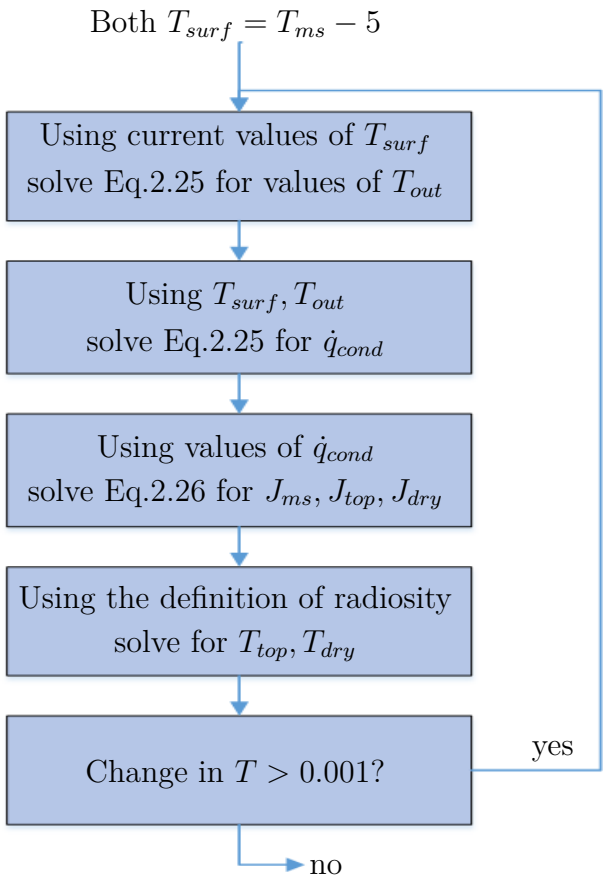

Figure 2.18 Radiative losses computation process.

First we start by assuming that the inner surface temperatures of both surfaces, $T_{in,top}, T_{in,dry}$ are the same and equal to $T_{ms} - 5$. Then for each surface, assuming this temperature, we find the heat transfer rate from the inner surface to the atmosphere. In order to do so and assuming steady states conditions, we recognize that the amount of heat being conducted through the insulation is equal to the heat being transferred to the atmosphere. Generally, we obtain Equation 2.25, which can be solved for T_{out} to obtain $\dot{q}_{cond}$:

$$\dot{q}_{cond} = \frac{T_{surf} - T_{out}}{R_{cond}} = \epsilon_{out}\sigma(T_{out}^4 - T_{atm}^4) + \frac{T_{out} - T_{atm}}{R_{conv}}. \tag{2.25}$$

Once a first value of $\dot{q}_{cond}$ is obtained, we use it to find the value of both inner surface temperatures that allow each section to receive enough radiation to match this heat rate. When doing so, we consider each surface to be a gray surface. Using the properties of stainless steel, we use a value of emissivity $\epsilon_{ss} = 0.35$ for the dry surfaces and a near black body approximation for the molten salt surface: $\epsilon_{ms} = 0.95$.

Figure 2.19 above shows the part of the circuit that corresponds to the 3 surface radiative

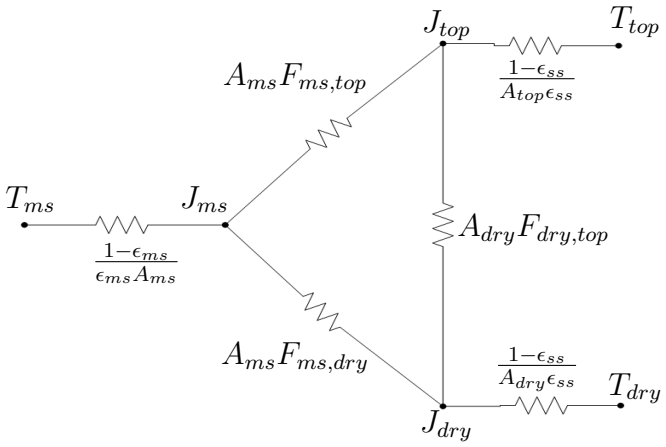

Figure 2.19 Gray surfaces radiation transfer sub-circuit.

heat transfer and the corresponding thermal resistance expressions being used. Recognizing that heat is conserved at each node of the circuit, we obtain the following equations:

$$\begin{aligned} -\dot{q}_{top} &= \frac{J_{top} - J_{ms}}{A_{top}F_{top,ms}} + \frac{J_{top} - J_{dry}}{A_{top}F_{top,dry}} \\ -\dot{q}_{dry} &= \frac{J_{dry} - J_{ms}}{A_{dry}F_{dry,ms}} + \frac{J_{dry} - J_{top}}{A_{dry}F_{dry,top}} \\ \frac{\sigma T_{ms}^4 - J_{ms}}{(1-\epsilon_{ms})/\epsilon_{ms}A_{ms}} &= \frac{J_{ms} - J_{top}}{A_{ms}F_{ms,top}} + \frac{J_{ms} - J_{dry}}{A_{ms}F_{ms,dry}}. \end{aligned} \tag{2.26}$$

For two parallel circular surfaces of diameter D, facing each others and separated by a distance d, it can be shown (see [29] Table 13.2) that the view factor $F_{ms,top}$ is given by:

$$F_{ms,top} = \frac{1}{2}\left[S - \sqrt{S^2 - 4}\right],$$

where

$$S = 2 + (2d/D)^2.$$

Since the empty volume of the tank is a closed volume, the view factor from the molten salt surface or the top surface to the cylindrical non-wetted wall is $F_{ms,dry} = F_{top,dry} = 1 - F_{ms,top} = 1 - F_{top,ms}$, as obtained by using the principle of conservation of energy. Applying the same principle yields the view factor for the non-wetted wall to itself and to the top surface.

The values of $\dot{q}_{top}$ and $\dot{q}_{dry}$ in Eqs. 2.26 are obtained by solving Eq. 2.25 for the value of $\dot{q}_{cond}$ for each surface. By convention, the values of $\dot{q}$ are positive when the net radiative flow leaves the surface, and negative when it is absorbed. Hence the minus signs for $\dot{q}_{top}$ and $\dot{q}_{dry}$.

2.2.4 The Steam Generator

The steam generator consists of a salt-to-water heat exchanger with phase change occurring when the water is turned to steam. This is a rather complex device to model because of the phase change, which induces important variations in the heat transfer coefficient due to changes in fluid properties like viscosity and density, as well as an irregular temperature progression (for the duration of the phase change, the water remains at constant temperature).

Two options are available to simulate this unit. The first option is a very simplified model for which no design parameters are required, consisting only in an energy balance equation. The second model simulates a shell-and-tubes heat exchanger.

Energy balance model

The steam generator's outlet molten salt temperature, as well as the inlet and outlet conditions of the water, are provided by the user as design parameters. Knowing the enthalpy difference on the water side of the exchanger, as well as the inlet and outlet temperatures of the molten salt, a simple energy balance is computed in order to determine the flow of molten salt required to provide the powerblock with the requested thermal energy.

$$\dot{m}_{ms} = \frac{Q}{c_{ms}(T_{Gn,ms,in} - T_{Gn,ms,o})}. \tag{2.27}$$

The heat exchanger is assumed to be able to provide the sufficient heat transfer rate to ensure that the outlet conditions are met for both fluids. In reality, having a heat exchanger that ensures specific outlet conditions for both fluids, for a variable flow of these fluids, is rather complicated.

Shell-and-tubes model

The second option is a model for a shell-and-tubes heat exchanger which is simplified by not considering the changes in fluid properties related to the phase change. The water is therefore treated as a liquid when it comes to evaluating the heat transfer coefficients. This is without question a gruesome simplification, and a better way to do it would have been to determine a point along the tubes' length from which the water is turned to steam and compute the heat transfer separately for the two portions of the tubes. This approximation was kept, for now, for time considerations.

The Effectiveness-NTU method [29] is used to determine the flow of molten salt necessary to achieve the expected heat transfer rate. When using this model, the outlet temperature

of the molten salt is not constant. Using this model requires additional design parameters from the user, as listed in Table 2.5.

Table 2.5 List of design parameters for the shell-and-tubes steam generator model.

Symbol	**Definition**	**Unit**
D_{in}	inner diameter of tubes	m
D_o	outer diameter of tubes	m
H_{baf}	baffles cut	-
L_{tubes}	length of tube passes	m
N_{baf}	number of baffles	-
N_{pass}	number of tube passes	-
N_{shell}	number of shell passes	-
N_{tubes}	number of tubes	-

The effectiveness-NTU method provides a means to use empirical equations to characterize the performance of different heat exchanger configurations. The effectiveness ϵ is defined as the ratio of the actual heat transfer taking place over the maximum theoretical heat transfer with regards to the inlet conditions of both fluids.

$$\begin{aligned} \epsilon &= \frac{Q}{Q_{max}} \\ Q_{max} &= C_{min}(T_{h,i} - T_{c,i}) \\ C_{min} &= \min(C_h, C_c) \\ C_h &= c_{ms}\dot{m}_{ms} \\ C_c &= \frac{h_{w,out} - h_{w,in}}{T_{c,o} - T_{c,i}}\dot{m}_w \end{aligned} \tag{2.28}$$

For specific heat exchanger characteristics, ϵ can be determined empirically for a shell-and-tubes heat exchanger with N_{shell} and N_{pass} [29]:

$$\epsilon = \left[\left(\frac{1-\epsilon_1 C_r}{1-\epsilon_1}\right)^{N_{shell}} - 1\right]\left[\left(\frac{1-\epsilon_1 C_r}{1-\epsilon_1}\right)^{N_{shell}} - C_r\right]^{-1} \tag{2.29}$$

$$\epsilon_1 = 2\left[1 + C_r + \left(1 + C_r^2\right)^{1/2}\frac{1 + e^{-(NTU)_1(1+C_r^2)^{1/2}}}{1 - e^{-(NTU)_1(1+C_r^2)^{1/2}}}\right]^{-1} \tag{2.30}$$

$$
\begin{aligned}
NTU_1 &= \frac{UA_{shell}}{C_{min}} = \frac{R_{tot}^{-1}}{C_{min}} \\
U &= \left[\frac{1}{h_w} + \frac{D_{in,tubes}}{k_{ss}} \ln \frac{D_{o,tubes}}{D_{in,tubes}} + \frac{D_{in,tubes}}{D_{o,tubes}} \frac{1}{h_{ms}} \right].
\end{aligned}
\tag{2.31}
$$

Provided the amount of energy Q that needs to be transferred to the powerblock and the specific enthalpy difference, the water flow $\dot{m}_w$ is determined along with the water velocity inside the tubes, to compute the heat transfer coefficient of the water. Equations 2.15 and 2.16 are used to determine the convection heat transfer coefficient to the water h_w.

The convection heat transfer coefficient on the molten salt side is then evaluated using Equations 7.60 to 7.63 and Tables 7.5-7.6 of [29] for a staggered arrangement of the tubes. No counterflow baffles are considered.

An iterative procedure is used from that point to determine the mass flow of the molten salt that will produce the desired heat transfer, along with the outlet temperature of the molten salt. The molten salt that would be required for the first basic exchanger model is used as a starting point (Equation 2.27).

$$
\begin{array}{ll}
C_h \leq C_c & \dot{m}_{ms} = \frac{Q}{\epsilon c_{ms}(T_{h,i} - T_{c,i})} \\
C_h \geq C_c & \dot{m}_{ms} = \frac{Q}{C_r \epsilon c_{ms}(T_{h,i} - T_{c,i})}
\end{array}
\quad .
$$

Using this new value of $\dot{m}_{ms}$, we iterate again until convergence is reached.

Note: using the second model is much more likely to result in a failure to compute. It is entirely possible to set the design parameters for the heat exchanger so that it will be impossible to achieve the desired heat transfer at all time, or to even build one that is *too* efficient for the purpose (too much heat is removed from the molten salt for any given volume so that its temperature falls below its melting point).

Tubes arrangement and shell dimensions

In order to determine the performance of the shell-and-tubes heat exchanger, important values that are not directly defined as input variables need to be determined. Namely, the shells diameter, the number of rows, the longitudinal pitch of the tubes arrangement and the space between baffles.

Baffles spacing S_{baf} is simply determined by considering the shell's length equal to that of the tubes and by distributing the baffles uniformly:

$$S_{baf} = \frac{L_{tubes}}{N_{baf} + 1}. \tag{2.32}$$

The longitudinal pitch S_l is the spacing between the rows of tubes inside the shell. In this work, we consider that the tubes are always arranged in an equilateral triangular lattice. The tubes spacing S_t is defined as the transversed pitch (the distance between the center of two adjacent tubes of the same row). Thus the longitudinal pitch is:

$$S_l = S_t\sqrt{3/4}.$$

The shell diameter D_{shell} is the minimum possible diameter so that the tubes can fit inside with the desired spacing. Because we use an equilateral triangular lattice arrangement, this minimum diameter is estimated by using an hexagon packing strategy, with hexagons of a side length h equal to the minimum length necessary to box a circle of diameter equal to S_t:

$$h = \frac{S_t\sqrt{4/3}}{2}.$$

In order to estimate the diameter of the shell, we define a lower and upper bounds, D_{lo} and D_{up}, between which we know it is possible to find a valid solution. The final shell diameter is found using a convex combination of the two bounds, with the weight u being a function of the total number of tubes $N_{tot} = N_{tubes}N_{pass}$.

Recognizing that a higher number of tubes will reduce the relative difference between the area of the circle that circumscribes the hexagonal tiling and the area of the tiling, we define u such that D_{shell} will be chosen to be increasingly close to D_{lo} as N_{tot} grows. Note that for any realistic solution, N_{tot} should always be rather high (well over 100), even for a small power plant.

$$D_{shell} = uD_{up} + (1-u)D_{lo}$$
$$u = \frac{1}{\sqrt{N_{tot}}}.$$

Let N_{hex} be the number of hexagons in a tessellation containing n_r layers from an initial central hexagon. Then,

$$N_{hex} = 1 + 6\frac{n_r(n_r+1)}{2}.$$

Finding the smallest n_r such that $N_{tot} \leq N_{hex}$, we obtain an upper bound for the smallest shell diameter required to circumscribe the tubes in this arrangement as

$$D_{up} = (2n_r + 1)S_t > D_{shell}.$$

Then, supposing even a perfectly optimal arrangement of the hexagons to fit them inside a circle, we know that the area of a circle that would circumscribe the tubes could never be smaller than the total area of the tessellation. Thus we obtain our lower bound by finding the diameter of a circle of area equal to the ideal arrangement:

$$D_{lo} = \sqrt{\frac{N_{tot}A_{hex}}{\pi/4}} < D_{shell},$$

A_{hex} is the area of a single hexagon ($A_{hex} = 3h^2\sqrt{3/4}$).

The number of rows N_{row} is found simply from the shell diameter and the longitudinal pitch:

$$N_{row} = \downarrow \left(\frac{D_{shell}}{S_l}\right).$$

2.2.5 The Powerblock

The only powerblock related variable is the choice of the type of turbine. Technical data for a variety of actual steam turbines specifically used for CSP applications are retrieved from steam turbine manufacturer Siemens. This part of the model is used to determine the amount of energy that ought to be extracted from the molten salt in order to meet the power demand P_{dem}.

The steam inlet pressures and temperatures required to operate each turbine, as well as their respective maximum and minimum power output, are provided on Figure 2.20. Using these values, the choice of either turbine will yield the required conditions at the steam generator outlet $T_{in,tur}, P_{in,tur}, h_{in,tur}$.

A simple empirical model for determining the steam turbine efficiency as a function of the inlet steam conditions and capacity usage ratio f_{tur}, provided by Bahadori and Vuthaluru [7], is used to determine the steam turbine's instantaneous efficiency η_{tur}. Using η_{tur} along with the vapor quality requirement χ at the turbine outlet, we find the enthalpy per unit $h_{o,tur}$ mass of the exiting vapor. Assuming a mechanical-to-electrical efficiency η_{ele} of 95%, we

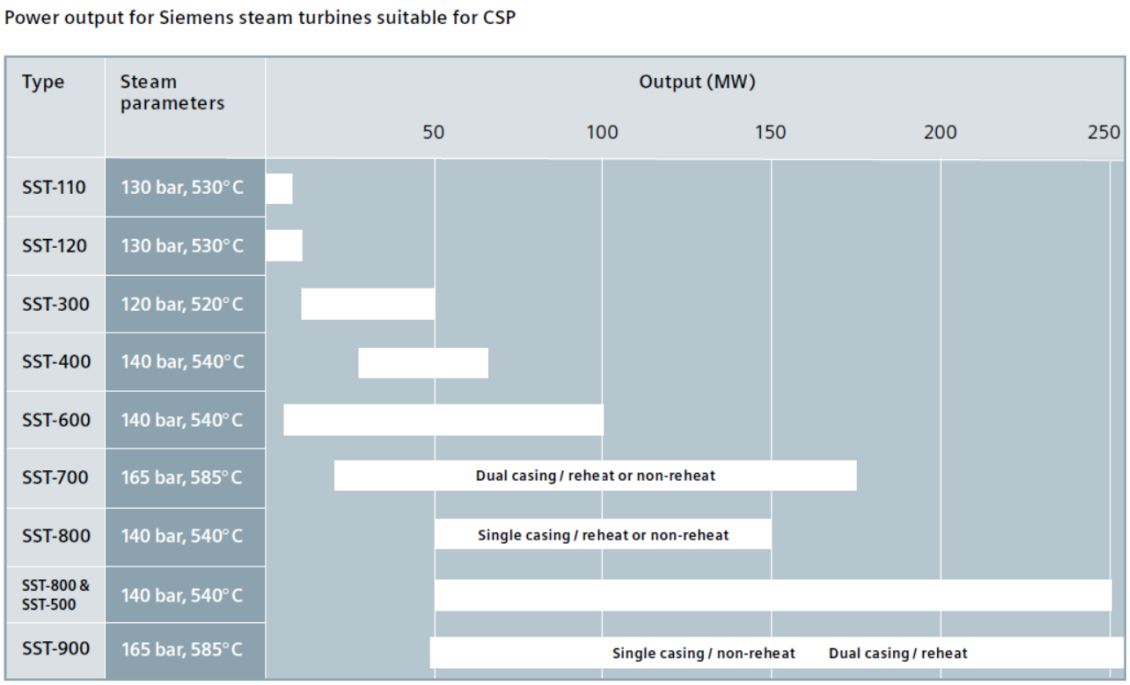

Figure 2.20 CSP steam turbines data from Siemens [52].

obtain the steam rate at the turbine (and steam generator) with Equation 2.33

$$\dot{m}_{st} = \frac{P_{dem}}{(h_{in,tur} - h_{o,tur})\eta_{ele}\eta_{tur}}. \tag{2.33}$$

As depicted in Figure 2.1, the low pressure steam that gets out of the turbine then has to be cooled in condensing unit and then pumped through the compressor before it goes through the steam generator again. Assuming a perfectly isobaric cooling of the saturated vapor, we find the drop in enthalpy Δh that is necessary to obtain a saturated liquid (with a vapor quality $\chi = 0$). The total heat rate $\dot{Q}$ transferred from the molten salt to the steam cycle for this interval is

$$\dot{Q} = \dot{m}_{st}(h_{in,tur} - (h_{o,tur} - \Delta h)). \tag{2.34}$$

All components of the power cycle other than the turbine are idealized, and the energy required by the compressor to compress the liquid water is not explicitly computed, and is thus comprised in the total amount of energy transferred from the molten salt. This was neglected because the energy input to compress a liquid is small. No transient regime is considered and the whole cycle is assumed to shift instantly to match the demand profile. For most turbines, there exists a minimum value of power for which it can be operated. In the event that the demand is inferior to the minimum requirement for a turbine, the model

will operate it at its minimum, least efficient regime, if possible, in order to reflect the fact that stopping the plant entirely in the middle of production is usually a bad operational option.

2.3 Auxiliary models

The auxiliary models are used to provide constraints to the optimization problems. Without them, the solution to many of the problems would be trivial, and the optimal solution would be impractical. For example, the thickness of the insulation is not counter-balanced by any physical phenomenon that is hereby taken into account. Thus we could expect that for every scenario, the value of the insulation for the storage and receiver units would always end up being set at their highest value. The same goes for the heliostats: there is no doubt that the best way to maximize the field's surface efficiency is to fill it with a maximum number of very small heliostats.

In order to provide a sufficient amount of constraints, four auxiliary models have been developed to extract the following informations from the simulation: equipment costs, parasitic loads, tubes stress and the energy demand.

The demand model differs from the other three in that it does not extract information from the simulation but instead drives the model by dictating, at all time, the amount of energy that the powerblock must be seeking to generate.

2.3.1 Initial Capital Cost Model

Although no complete life cycle cost analysis is integrated in the simulation, a simple initial investment cost model is provided in order to serve as a limiting factor for many of the design parameters.

While ignoring the economic considerations altogether would lead to unrealistic optimization results, a complete life cycle cost analysis goes beyond the scope of this project and would increase the complexity of the different scenarios by requiring many additional parameters such as long term interest rates, inflation, market-wide energy costs, maintenance cost and associated costs of labor, scheduling, etc. Not considering these factors leaves us unable to compute the levelized cost of energy (LCOE), but at least allows us to bound many parameters within realistic ranges.

The data used to build the capital cost model was taken mostly from the National Renewable Energy Laboratory report on the SAM (System Advisor Model) [59] software and the Sandia

Roadmap report [34]. The SAM model provides a means to determine the value of each component, but does so through an empirical model that mostly uses relations to the size or desired capacity of the plant: its objective is to predict the potential cost of a project based on its sheer scale, rather than based on specific technical characteristics. This turns out to be of little use to serve as a limiting factor in optimization problems.

In order to link the cost of the components to their basic design parameters, basic relations have been established from disparate sources of information on the price of the materials. The total cost C_{tot} of the power plant is the sum of the costs of its subsystems, each of which are described as a function of some of the design parameters previously listed in their respective sections.

$$\begin{aligned} C_{tot} =& N_{hel}C_{hel}(h, l, N_{hel}) + C_T(H_T) + C_{Re}(H_a, W_a, d_{Re}) + C_{HS}(H_{HS}, D_{HS}, d_{HS}) + \\ & C_{CS}(H_{HCS}, D_{CS}, d_{CS}) + C_{Sg}(N_{tube}, N_{pass}, N_{shell}, L_{tube}, D_o) + C_{tur} \end{aligned} \tag{2.35}$$

2.3.2 Parasitic loads model

The parasitic loads consist of the power required to operate the plant. SAM considers a detailed set of parasitic loads, including the electronic and mechanic systems to control the sun-tracking system of the heliostats, piping anti-freeze protections, the HTF pumps in the storage units, the receiver and steam generator, steam condenser and compressor operations, etc. A study produced by The Sunshot Initiative commanded by the U.S. Department of Energy (DOE) in 2012 [54] estimates that for documented CSP applications, parasitic loads typically consume between 10 to 15% of the power plant's total energy production.

In the current work, most components of the system that were not directly necessary to describe the dynamic of a CSP system, such as electronic controls or pumps, have been idealized. Thus the parasitic loads model is non-exhaustive, but considers the most important elements.

As with the investment cost model, the idea here is to provide an additional source of optimization constraints to prevent optimizers to reach unrealistic design points or trivial solutions. In this case, the limitations on the system are mostly physical. For example, the average heat transfer coefficient of the molten salt in the receiver unit is generally improved by a higher fluid velocity inside the tubes. Thus it is possible that a design using a single tube with hundreds of passes would be preferred to a design with several dozens of tubes, each doing only a few passes. Unfortunately, while this might result in a higher heat transfer, the pressure and power required in order to make large amounts of fluid flow at high velocity in a narrow tube of this length would probably be too large for such a design to be viable.

Since the pumps and pipes linking the main components of the system are not explicitly simulated or subject to optimization, their contribution to the losses are not considered. The evaluation of the parasitic load W_{par} is thus comprised of five terms:

$$W_{par} = W_{Re} + W_{shell} + W_{steam} + W_{fld} + Q_{AF}, \tag{2.36}$$

W_{Re} energy to pump HTF through the receiver

W_{shell} energy to pump HTF through the exchanger shell

W_{steam} energy to pump water through the exchanger tubes

W_{fld} energy to operate the heliostat field

Q_{AF} energy for the storage units anti-freezing systems.

Note that the energy required to pump fluid from the storage units is neglected. It is safe to assume that the losses to pump fluid in and out of a large reservoir are small compared to the losses observed when pumping fluid through an intricate circuit of tubes. Also the fact that no design parameter pertaining to the storage units currently represented in the model would be impacted by this constraint, as no variable is used to specify the geometry of the storage tanks inlet and outlet nozzles.

The following sections detail how the value for each of these terms are obtained.

Pumping losses through the receiver

The power required to pump fluid is generally obtained as such:

$$\dot{W}_{pump} = \frac{\dot{V}\Delta P}{\eta_{pump}}, \tag{2.37}$$

where $\dot{V}$ is the flow rate in m^3/s, ΔP is the pressure differential between the inlet and the outlet of the pump that forces the fluid to flow through the hydraulic element being analyzed, and η_{pump} is the pump's efficiency. For this section and all other sections about hydraulic friction losses, η_{pump} is assumed to be 0.90.

At all time, we assume that the pumps are capable of providing the required flow rate and pressure, and we simply compute what those values would be. The pressure differential is a function of both the flow rate and the geometry of the receiver.

For the receiver, we consider the flow of molten salt through the tubes.

$$\Delta P_{Re} = \Delta P_{tube} + \rho g H_T. \tag{2.38}$$

Where ΔP_{tube} is the pressure differential caused by friction in the receiver tubes and the second term on the right is the pressure differential caused by the height of the tower. Using equations from [29] for straight and smooth tubes,

$$\Delta P_{tube} = \frac{\lambda L_{tube} \rho_{ms} v^2}{2 D_h}. \tag{2.39}$$

L_{tube} is the length of one tube ($L_{tubes} = N_{pass} H_{Re}$)

v is the fluid velocity in one tube

D_h is the tubes inner diameter

λ is a function of the Reynold's number

The receiver absorber wall is assumed to have a vertical semi-cylindrical shape and the tubes have a length equal to its height. The tubes are assumed to be straight even for cases where there are multiple passes. Eq. 2.40 gives the expressions used to obtain λ depending on the value of Re:

$$\lambda = \begin{cases} 64/Re, & \text{if } Re < 2300 \\ 0.5\left(\frac{64}{Re} + 0.3164 Re^{-1/4}\right), & \text{if } 2300 \leq Re < 4000 \\ 0.3164 Re^{-1/4}, & \text{if } 4000 \leq Re < 100000. \end{cases} \tag{2.40}$$

Pumping losses through the exchanger tubes

As explained in section 2.2.4, water flows in the tubes side of the heat exchanger and is turned to pressurized steam. Here, we make the (false) assumption that water remains a liquid until it exits the steam generator in order to simplify the calculations pertaining to the latter's performance. The procedure to do so is exactly the same as in the section above. The same equations are used except for the fact that the fluid's properties are those of water, and that no height difference is considered.

$$\Delta P_{st} = \frac{\lambda L_{tube} \rho_w v^2}{2 D_h}. \tag{2.41}$$

Pumping losses through the exchanger shells

Evaluating the pressure drop inside the exchanger shells is not a simple thing to do. Gaddis and Gnielinski [23] proposes a high level model to predict the pressure drop across a single

shell $\Delta P_{shell,0}$, containing the evaluation of the pressure drop for each of the different sections of the shell. The model proposed by Gaddis and Gnielinski also includes correction coefficients to account for leakage and bypass occurring as result of manufacturing limitations. In the current work, these imperfections are neglected and we set leakage coefficients to 1. Aside from this simplification, the model is used integrally.

$$\Delta P_{shell,0} = (N_{baf} - 1)\Delta P_Q + 2\Delta P_{QE} + N_{baf}\Delta P_F + \Delta P_S \tag{2.42}$$

ΔP_Q is the pressure drop in a cross flow section

ΔP_{QE} is the pressure drop in the inlet and outlet cross flow sections

ΔP_F is the pressure drop in a window section

ΔP_S is the pressure drop in the inlet and outlet nozzles

Placing the shells in series, the total pressure drop across the whole heat exchanger is found as $\Delta P_{shell} = N_{shell}\Delta P_{shell,0}$.

Power to drive the heliostat field

The heliostats are large structures that track the sun at all time of the day. Power is necessary to drive the position actuators. In their simulation of a power plant similar to Gemasolar, Amadei et al. [2] used a constant value of 55W per heliostats. This value is used here for all moments of the day for which the sun's elevation α_s is greater than zero, that is, for every time interval that requires the heliostat field to be operated:

$$\dot{W}_{fld} = \begin{cases} 55N_{hel}, & \text{if } \alpha_s \geq 0 \\ 0, & \text{if } \alpha_s < 0. \end{cases} \tag{2.43}$$

A more detailed model could take into account the fact that various actuators with different power consumption may be required depending on the size of the heliostats.

Power dedicated to anti-freezing systems

While molten salt offers interesting thermal properties, it also has a melting point that is well above the temperatures that can be found in the environment surrounding the power plant. This means that molten salt that remains in the storage tanks might cool down below its melting point and "freeze". To prevent this from happening, each tank contains anti-freeze systems that will generate the heat necessary to keep the storage above a critical

temperature. For each iteration of the molten salt loop, if the computation would result in a storage temperature that is below the melting point of the salt mixture, energy would be required from the anti-freeze system. This is expressed as:

$$\dot{Q}_{AF} = \begin{cases} \dot{Q}_{loss,stor}, & \text{if } T_{stor} + \Delta T < T_{melt} \\ 0, & \text{if } T_{stor} + \Delta T \geq T_{melt}. \end{cases} \tag{2.44}$$

2.3.3 Yield constraints models

A simplified model to consider the stress sustained by the steel of the tubes in the receiver and steam generator is included in order to provide a limiting factor on their thickness and diameter. For the sake of simplicity and time, creeping effects in metals are not considered, although the system operates at temperatures for which this effect can't be expected to be negligible.

An exhaustive study of the heat exchanger system would also consider the stress imposed on the tubes by the molten salt, thereby providing an additional limiting factor on the tubes length and spacing and the baffles spacing. In the present work, though, only the outward radial pressure exerted by the fluid flowing inside the tubes is considered. The tension stress in the tubes steel is expressed as

$$\sigma_{tube} = \frac{D_{in}P}{2(D_o - D_{in})}. \tag{2.45}$$

In the central receiver, the molten salt is not pressurized and high pressure is the result of friction losses in the tubes. In the steam generator, the tubes contain water/steam which is pressurized by the compressor prior to entering it. Thus the pressure inside the tubes is caused by both the pressurization of the steam and friction. Because of the friction-induced pressure drop, the stress is maximum where the fluid enters the tubes circuit.

At all time, the pressure in the tubes must be such that $\sigma_{tube} < \sigma_{yield} = 290MPa$.

The determination of the pressure drops through the receiver and steam generator are shown in detail in section 2.3.2. In both cases, only the radial pressure exerted by the fluids inside the tubes is considered. We consider the extremities of the tubes to be solidly attached so that any tension in the axial direction is ignored.

2.3.4 Demand model

The demand model is independant of the simulation and design parameters. It is hardcoded as part of each optimization problem. It is what dictates to the powerblock the amount of energy that it must seek to generate during every time interval of the simulation. Three different profiles of the daily power demand are used in scenarios. One is a profile for scenarios in which the power plant is expected to generate power only during peak hours and is not expected to be the sole provider to the grid. The power plant is expected to produce a constant amount of power during a pre-determined schedule in order to alleviate the stress on the other means of energy production. In the context of the current market, this is what is most common, as solar thermal energy takes up only a decimal part of the global demand. This allows the turbine of CSP plants to be isolated from instantaneous power transients and to operate at its optimal regime.

The two other profiles simulate a case in which the power plant is actually expected to provide a substantial part of the total energy demand and is subjected to load transients. Data on the electricity demand was obtained from the IESO website [28], which tracks the hourly market demand in Ontario. The hourly demand for the winter day profile was obtained by averaging it over each day of the month of January in 2013. The same was done over the month of July of the same year for the summer day profile.

2.4 Model validation

Given the context and scope of this project, an exhaustive validation of the whole model was deemed too long. However, many parts of the whole power plant model were simulated using existing models of the main components. When existing models were applied almost integrally, as was the case for the central receiver and the thermal storages, the validation consisted mostly in verifying that the performance obtained was coherent with some of the published results. Li et al. [37] provided the average efficiency obtained for a simulation with parameters matching the Sandia National Laboratories' molten salt electric experiment receiver's. Zaversky et al. [63] provide heat drop data for specific tank sizes and insulation thickness, for the full hot tank and empty cold tank over a 24 hours period, for winter and summer days. These scenarios were tested, mostly to ascertain that the C++ implementation of these models was correct.

For the components that were not modeled from a single existing model, or for the whole power plant model, the difficulty arose from having little relevant available data: while there exist several well documented CSP plants, few use exactly the same combination of

technologies variants. For instance, while the Gemasolar [13] and Solar II [41](for which it was easiest to find performance and parametric data,) both use a heliostat field, they do not use a cavity receiver. Solar II also uses more than one heliostats sizes. Also the technical informations did not necessarily match the model's parameterization, so that some values had to be decided arbitrarily, or some specific details could not be accounted for in the model. These differences, combined with the obvious fact that the data is impacted by a number of operational factors that are not taken into account in numerical simulations, made it difficult to make relevant comparisons even for realistic cases.

Despite important differences in the shape of the heliostats field, the model was tested by running a simulation with the design parameters values set according to those of Solar II [60]. The parameters for the heliostats dimensions were chosen so that the total reflective surface and number of heliostats would be the same as that of Solar II. The simulation used the same latitude and production schedule and power, starting with an empty hot tank. We verified that the energy transfered to the thermal fluid, the duration of sustainable production using the storage and the overall solar-to-electricity conversion rate were comparable [42].

CHAPTER 3 OPTIMIZATION PROBLEMS

This chapter presents a family of nine optimization problems prepared using the power plant model described in Chapter 2. Exhaustive descriptions of the nine problems are provided in the appendices at the end of this document. Section 3.1 describes the general blackbox problem definition. Section 3.2 gives an overview of the diversity of the specific problems proposed as a result of this work, of which the validity is assessed in Section 3.3.

3.1 Blackbox problem description

We consider the optimization problems of the form

$$\begin{aligned} \min_{x} \quad & F(x) \\ s.t. \quad & C(x) \leq 0 \\ & \ell \leq x \leq u, \end{aligned} \tag{3.1}$$

where $F : \mathbb{R}^n \to \mathbb{R}^{N_{obj}}$ are the objective functions to minimize according to a set of constraints $C : \mathbb{R}^n \to \mathbb{R}^{N_c}$, x is the set of variables corresponding to the design parameters according to which the minimization of the objective functions is attempted, and where ℓ and u are respectively the lower and upper bounds of x in $\mathbb{R}^n \cup \{\pm\infty\}$. Depending on the problem definition, the elements of x may be real numbers, integers, binary, or categorical variables (materials, radically different configurations, etc.).

While, in the present case, the underlying modeling on which are based the objective functions and constraints substituted into Equations. (3.1) to create our set of problems is known and described in details in Chapter 2, it is important to note that the actual implementation of this modeling is, as mentioned in Section 1, a blackbox. For any set of variables x and a problem containing N_{obj} objective functions and N_c constraints, the program returns only a formatted output in the form of a single vector y containing the values of F and C such that $y^T = [f_1, ..., f_{N_{obj}}, c_1, ..., c_{N_c}]$. This straightforward dynamic is displayed in Figure 3.1.

Figure 3.1 Blackbox problem dynamic.

The optimization process, shown in Figure 3.2, consists in successively calling the blackbox with different values of x, and using the resulting y to dictate the values in the next x. For each problem contained in the blackbox, we define which design parameters are contained in x, which are fixed (and the values to which they are fixed), how y is computed from the simulation results, and which parts of the model are used to perform the simulation.

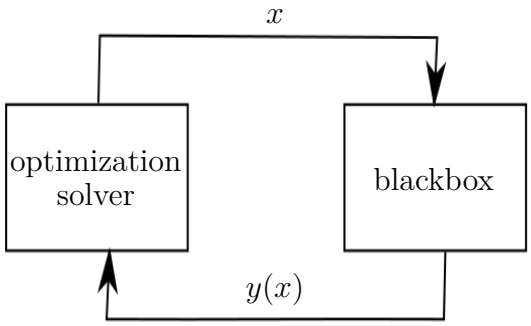

Figure 3.2 Blackbox optimization process.

Because the optimization solver is independent from the blackbox, it receives no information about the nature of the problem that is being solved. Thus all problems are treated as minimization problems by default: if the objective of a problem would be to maximize a value $f(x)$, then the return value of the blackbox for the objective function will be $F(x) = -f(x)$ instead.

Similarly, the constraints are all expressed so that a negative or zero value always indicates a success, and a strictly positive value means that the constraint was violated. For example, the first constraint $C_1(x')$ might indicate whether the solution x' satisfies a budget constraint $cost_{max}$. In this case, C_1 is expressed as $C_1(x') = cost(x') - cost_{max}$. In this form, $C_1(x')$ provides the margin by which the constraint is satisfied or exceeded. In other cases, it may be binary, indicating only if the constraint is satisfied or violated by respectively returning either 0 or 1.

The constraints in each problem may have different origins. Those that are tied to the optimization problem itself, that is, tied to quantitative limitations specific to the scenario (budget, surface area, power output requirements, etc.), are high-level design considerations that must be respected by the final solution. During the optimization process, though, they can be violated in order to progress towards better solutions. These constraints are always presented first after the objective function on the formatted problem output.

Other constraints are recurrent in most problems, independent of the scenario. They are feasibility constraints that may also be violated and are necessary in order to guarantee that

the solution is realistic. For example, in the heat exchanger, the tubes need to be sufficiently thick to withstand the steam pressure, and the molten salt cannot exit it with a temperature less than its melting point. While violating these constraints would result in a dysfunctional design, the simulation can still run its course and the results of it are still relevant in finding new candidate solutions.

Some constraints, however, are known relations between some variables that need to always be respected for the simulation to be possible: for example, the inner diameter of a tube must be smaller than its outer diameter. The compliance to these constraints is assessed before the simulation goes through and will prevent it from happening if they are not satisfied.

Finally, there are "hidden" constraints [17] consisting mostly of code glitches or instability: some solutions may cause the code to crash or to enter an infinite loop. These constraints are not given explicitly in the problem definition as they are unknown.

When a call to the blackbox is made, by default, all values of y for this problem are set to very large value that exceeds any value that the simulation could reasonably produce for the constraints or objective functions (here, 10^{20}). In a case where the simulation fails to compute all the outputs, the blackbox computes the values of y that it can and leaves the others at default.

3.2 Problems set overview

The problems are implemented in the form of a console application that can be called to compute a single evaluation of the objective function(s) and constraints for a problem according to a specific x. Nine blackbox problems, each characterized by its own formats for x (number of variables and their respective type and bounds) and y (the number and definition of the objective function(s) and constraints), are implemented. They are summarized in Table 3.1. The second column gives the number of each type of variables. The third column indicates if the problem is single or bi-objective. The fourth column gives the number of constraints and whether or not some are binary, and the last column indicates whether the starting point that we provide is a feasible solution or not.

The simulation parameters and the values of the problem-specific constraints are chosen to reflect realistic engineering problems. For instance, budgets, maximum field surface, and power output requirements are derived from known data on existing similar power plants.

The numerical models used for this blackbox made no use of any binary constraints. Because the point is also to provide a diversity of challenges for blackbox solvers, problems 6, 7 and 9 use constraints that were deliberately coded to return binary values. That is, instead of

Table 3.1 Blackbox problems characteristics.

Prob.	**Variables**				**Object.**	**Constraints**		**Start point**
N	Total	N_{con}	N_{dis}	N_{cat}	N_{obj}	Total	binary	feasible
1	9	8	1	0	single	5	0	no
2	14	12	2	0	single	13	0	yes
3	20	17	2	1	single	12	0	no
4	29	21	5	1	single	16	0	no
5	20	14	5	1	single	12	0	no
6	5	5	0	0	single	6	4	no
7	7	6	1	0	single	6	6	yes
8	13	11	2	0	bi.	7	0	no
9	29	21	5	1	bi.	17	12	yes

returning any margin of feasibility (or unfeasibility), the values of the constraints are simply set to 0 if they are met, and 1 if they are violated.

Some choices of x can lead to a lengthy execution (more than 15 minutes). For that reason, the option to use a surrogate model (a computationally cheaper but less precise version of the simulation) is available for each problem. Some solvers take advantage of such alternative models to conduct the optimization, and use the original model only to verify promising solutions found on the surrogate. The remainder of this section gives a high-level description of each problem.

Problem 1 - Maximize heliostat field energy output

This problem runs only the heliostat field model. It uses 9 variables of which 1 is discrete and the others are continuous. The objective is to maximize the energy concentrated on the receiver aperture by the heliostat field in 24 hours, while respecting a $50M budget and a maximum field area. The objective is subject to 5 explicit constraints. Details about the expressions of the objective function, constraints and variables are given in Appendix A.

Problem 2 - Minimize the heliostat field surface

This problem runs the whole power plant model and uses the idealized model for the heat exchanger. It uses 14 variables of which 2 are discrete and the others are continuous. The objective is to minimize the heliostat field surface while satisfying the power demand peaking at 20MW and respecting a $300M budget. The objective is subject to 14 explicit constraints. Details about the expression of the objective function, constraints and variables are given in Appendix A.

Problem 3 - Minimize total investment cost

This problem simulates the whole power plant and uses the idealized model for the steam generator. It uses 20 variables of which 2 are discrete, one is a categorical variable and 17 are continuous. The objective is to minimize the total investment cost while satisfying the demand and respecting a maximum field size. The simulation is done over 24 hours and the power plant is required to provide constant 10MW during peak hours, between noon and 6 p.m. The objective is subject to 12 explicit constraints. Details about the expression of the objective function, constraints and variables are given in Appendix A.

Problem 4 - Minimize total investment cost with S-n-T heat exchanger

Problem 4 is similar to problem 3, but with an increased level of complexity, in that it uses the NTU-effectiveness steam generator model presented in Section 2.2.4 instead of the idealized model. It uses 29 variables of which 6 are discrete, one is a categorical variable and 22 are continuous. The objective is to minimize the total investment cost while satisfying the demand and respecting a maximum field size. The simulation is done over 72 hours and the power plant is required to provide power at all time for a summer day demand profile peaking at 25MW. The objective is subject to 16 constraints. Details about the expression of the objective function, constraints and variables are given in Appendix A.

Problem 5 - Maximize the satisfaction of the demand

This problem runs the HTF loop and the powerblock models and substitute a performance data file to the heliostat field in order to reduce the computation time. It uses 20 variables of which 5 are discrete, one is a categorical variable and 14 are continuous. The power plant performance is simulated over a period of 30 days with an inconsistent field performance analogous to slightly unreliable weather conditions. The objective is to maximize the time for which the power plant is able to operate at nominal capacity. A surrogate model is available for this problem which consists in running the simulation on only a fraction of the 30 days and extrapolating the resulting performance over the 30 days. The objective is subject to 12 explicit constraints. Details about the expressions of the objective, the constraints and about the variables are given in Appendix A.

Problem 6 - Minimize the cost of storage

This problem runs a predetermined power plant using the HTF cycle and powerblock models. It uses 5 continuous variables. The objective is to minimize the cost of the thermal storage units so that the power plant is able to sustain a 100MW electrical power output for a 24 hours period. Since the heliostat field is not being optimized, its hourly power output is

read from a prerecorded file instead of being simulated, in order to reduce the computation time. The objective is subject to 6 explicit constraints, 4 of which return binary values. Details about the objective, constraints and about the variables are given in Appendix A.

Problem 7 - Maximize receiver efficiency

This problem simulates the heliostat field and the central receiver unit over a 24 hours period. It uses 7 variables, of which one is discrete and the others are continuous. The objective is to maximize the receiver's efficiency. A surrogate version of the model can be used so that a much lower density of sunrays is used to evaluate the field's performance. The objective is subject to 6 binary constraints. Details about the expressions of the objective function, the constraints and about the variables are given in Appendix A.

Problem 8 - Maximize heliostat field performance and minimize cost

This problem runs the heliostat field and central receiver models. It uses 13 variables, of which two are discrete and 11 are continuous. This is a bi-objective problem of which the two objectives are to maximize the amount of energy transfered to the molten salt over a 24 hours period all while minimizing the total cost of the field, tower and receiver. The optimization is conducted over the design parameters of both the heliostat field and the central receiver. The objectives are subject to 9 continuous constraints. Details about the expressions of the objective functions, the constraints and about the variables are given in Appendix A.

Problem 9 - Maximize power and minimize losses

This problem simulates the entire power plant over a single day. It uses 29 variables, of which 6 are discrete, one is a categorical variable and 22 are continuous. This is a bi-objective problem of which the two objectives are to maximize the generated electrical power and minimize the parasitic losses while respecting a $1.2B budget. The objectives are subject to 17 constraints, 12 of which are binary. Details about the expressions of the objective functions, the constraints and about the variables are given in Appendix A.

3.3 Validation and optimization results

Part of the challenge of building a new blackbox is making sure that the resulting optimization problems would actually present a valid challenge. They need to have non-trivial optimal solutions, and they need to be acceptably functional. For instance, if a problem would be to minimize the cost of the designed power plant, it has to contain constraints sufficient to ensure that an optimization algorithm won't cling to a trivial solution such as a power plant

with no heliostats at all that has a very low cost but also produces absolutely no energy. In order to verify that the blackbox does indeed contain valid problems, each of them was put to the test using the NOMAD [1] software with default settings. NOMAD uses the MADS algorithm [4] to solve Problems 1 to 7. The results of this validation process for problems 1 to 7 are summarized in Table 3.2. Problems 8 and 9 being multi-objective, they are treated separately.

Table 3.2 Optimization results for all problems.

	Problems						
	1	2	3	4	5	6	7
starting at	-	3.7×10^{6}	-	-	-	-	-4.8×10^{12}
best sol.	-3.4×10^{5}	2.7×10^{6}	5.8×10^{7}	2.9×10^{8}	-27.6	4.5×10^{7}	-4.9×10^{12}
best sol. feasible	yes	yes	no	yes	yes	yes	yes
blackbox eval.	2470	5000	5000	5000	5000	877	3228
failures %	2.9	19.6	0	0	0	0	0
saturated var. %	0	11	5	0	21	60	0

The value of the objective function for the initial solution is not indicated when it is not feasible. For problem 3, the final solution is infeasible and thus the best solution is the least infeasible one. In all cases the optimization went without providing any trivial solution, as noticeable by the low level of saturated variables in the best solutions. Problems 2 however exhibits a high level of failures, which may cause problems for some solvers.

3.3.1 Analysis

In order to see how the optimization process has improved the initial solutions, and to verify the validity of the final solutions obtained, this section presents data retrieved from the simulations of both. We also present convergence graph for each problem. It is worth noting that the data used to generate the convergence graphs use only the real blackbox evaluations, and not those of the surrogate model. Thus the number of evaluations seen on these graphs may differ from the numbers that appear in Table 3.2.

Problem 1 consists in maximizing the heliostat field power output throughout the day, with constraints on the budget and field surface. Figure 3.3 shows the change between initial and final heliostat field, along with their hourly concentrated power.

Less than half the total budget of evaluations were used to solve this problem, and the optimization stopped because NOMAD had reached its stopping criteria for convergence. This suggests that the final solution proposed might be a local minimizer. Figure 3.4 shows

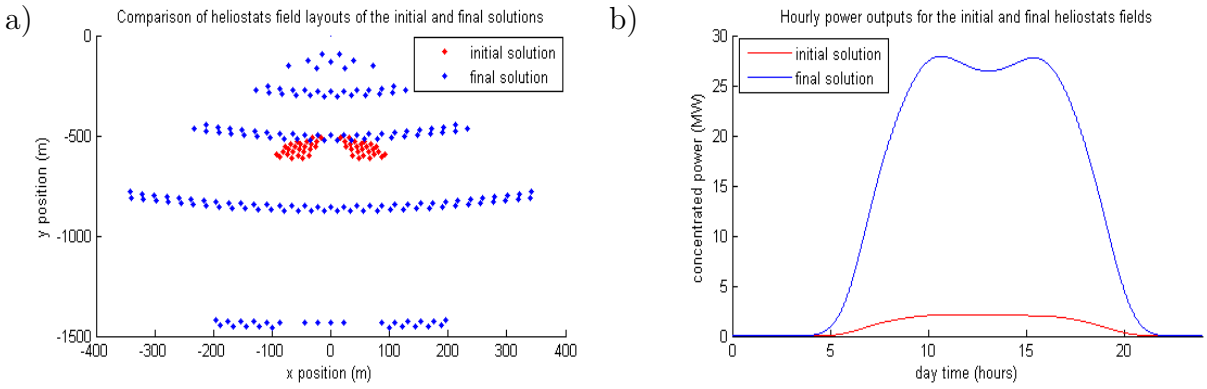

Figure 3.3 Differences between initial and final solutions of Problem 1: a) heliostat field layouts, b) hourly concentrated power.

the progression of the best value of the objective function in relation with the number of blackbox evaluations.

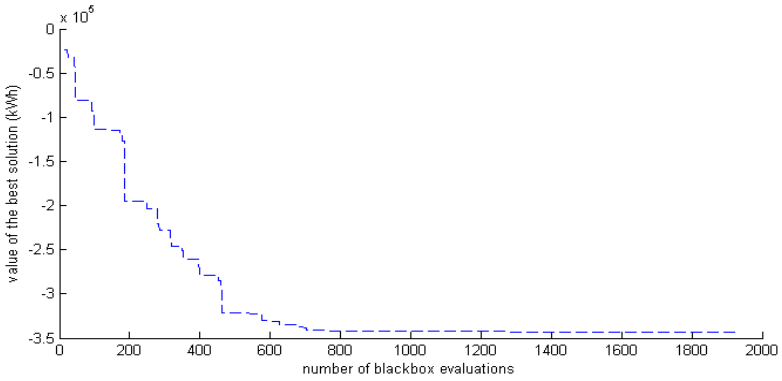

Figure 3.4 Convergence graph for Problem 1.

Table 3.3 compares the values of the constraints between the initial and final solutions. As reported in Table 3.1, the initial solution is not feasible.

In this problem, the two first constraints are of interest, whereas the last three are only simple geometric constraints that would prevent the simulation from happening if they were not satisfied. As described in Appendix A, the first constraint is the investment cost, which should not exceed 50M$, and the second one is the total field surface, which should not exceed $1.95\times10^6 m^2$. We see that the initial solution violates the first constraint significantly, but is also very far from violating the second one. Conversely, we see that the final solution not only meets the budget constraints, but does so by using virtually all of the budget, leaving a relatively small margin. We also see that it considerably reduces the margin by which

Table 3.3 Comparison of the feasibility of the initial and final solutions of Problem 1.

	initial sol.	**final sol.**
C_1	**3.1**$\times 10^7$	-484.3
C_2	-1.66$\times 10^6$	-5.5$\times 10^5$
C_3	-234	-30.33
C_4	-2	-19.06
C_5	0	0

the second constraint is satisfied. Predictably in this case, the optimal solution tends to maximize its use of the available resources (99.99% of the budget, and 71.8% of the available surface for the final solution, as opposed to 160% of the budget and 14% of the available surface for the initial solution).

Problem 2 consists in optimizing the solar collector (heliostat field and receiver) so that the total field surface required, to drive a predetermined power plant over a 72 hours period, is minimized. This problem starts with the hot storage filled to 60% of its maximum capacity. The entirety of the evaluations budget was used to optimize this problem, and the optimization stopped before NOMAD had reached convergence. Figure 3.5 shows the shape and the performance of the resulting heliostat field for the initial and final solutions, along with the level of the hot storage throughout the day.

This problem starts with an initial solution that is feasible, which explains in part why the difference observed between the performance and field configurations do not differ as much as the two solutions presented for Problem 1. The initial solution is already functional, and it must only be improved. As we can see in Figure 3.5 a), the final heliostat field reduces the land use. Expectedly, Figures 3.5 b) shows that the resulting power is also slightly smaller. During the simulation, the power plant is expected to generate a constant power output. We see from Figure 3.5 c) that the level in the hot storage drops faster with the final solution than with the initial solution. That is because the problem requires only the heliostat field to be such that power can be generated for a full 72 hours without interruption. This shows that the initial solution, while functional, was also gathering an excessive amount of energy with regard to the constraints. Thus we see that the final solution is designed to make use of the initially stored molten salt by eating away at it gradually during the course of the simulation. In fact, the hot storage in the final solution reaches the lowest level that it is allowed to, around the 55th simulated hour (in order to avoid instability in the evaluation of the temperature drop, the storage model does not feed the steam cycle if its level would drop below 5% of its maximum level, which is 10.5 meters here).

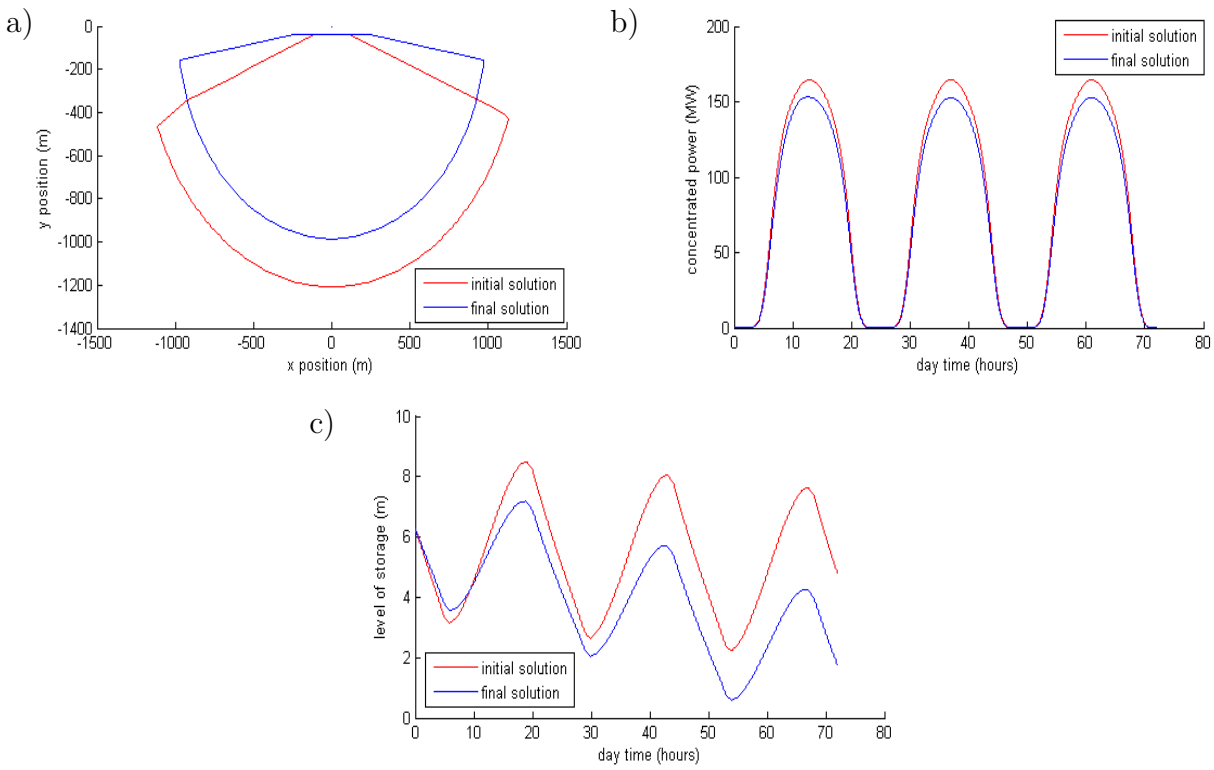

Figure 3.5 Differences between initial and final solutions of Problem 2: a) heliostat fields convex hulls, b) hourly concentrated power, c) level in hot storage.

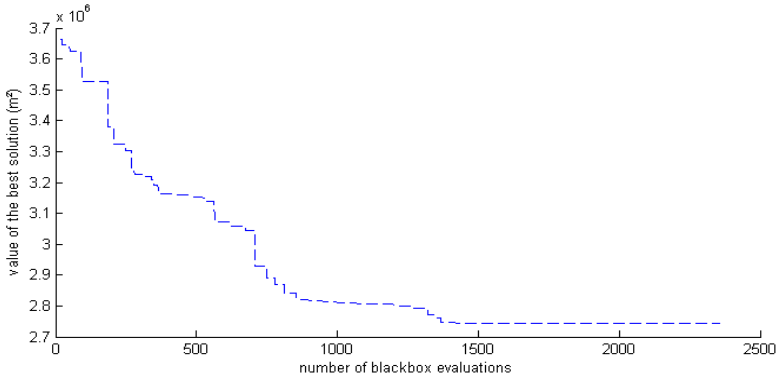

Figure 3.6 Convergence graph for Problem 2.

Since the optimization stopped before NOMAD reached its convergence criteria, this suggests that the final solution is not a local minimizer. However, as we can see in Figure 3.6, the value of the objective function could not be sensibly improved in close to 1000 evaluations, and the best solution proposed by NOMAD seems to be reasonably functional.

Problem 3 consists in minimizing the total cost required for a power plant to be able to generate 10MW between 3 p.m. and 9 p.m. Figure 3.7 shows the comparison of the power generated by both the initial and final solutions with the expected power production. We also show the progression of the level of the hot storage for both solutions.

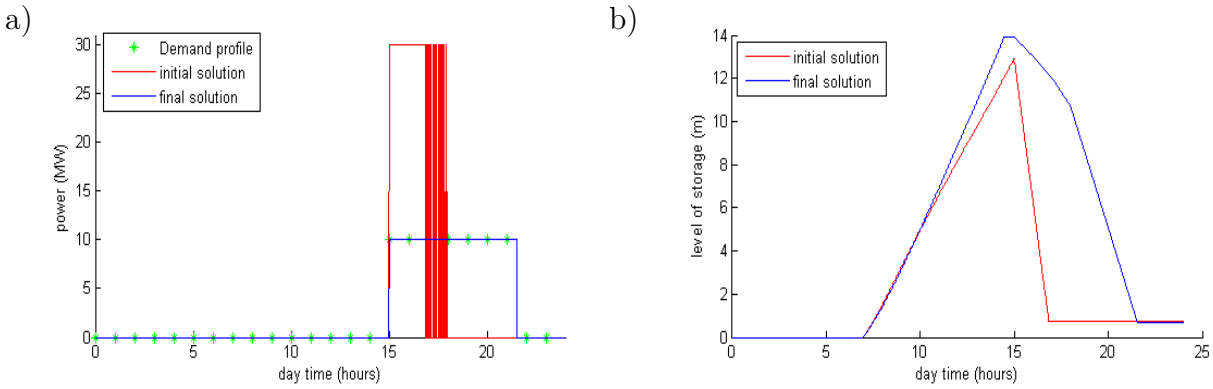

Figure 3.7 Differences between initial and final solutions of Problem 3: a) energy production compared with the demand, b) level of hot storage.

Figure 3.7 a) shows the profile of the power production for both the initial and final solutions. We can see that the initial solution, at first, generates more power than required by the demand. This is because the turbine selected in the initial solution has a minimal power production of 30MW. When this happens, the turbine works at its lowest regime, which also has the smallest efficiency. The behavior that we observe after the 17th hour demonstrates one of the shortcomings of the operating strategy and turbine modeling: repeated starts and stops of the turbine are not penalized, which can lead it to be activated as soon as enough molten salt is added to the storage to make it work for a single time interval. As we can see on Figure 3.7 b), the inconsistent behavior of the turbine does indeed coincide with the moment when the storage reaches its lowest permissible level, from which point the energy production is entirely reliant on the heliostat field output. A better operating strategy could have led the power plant to wait and start the energy production later, so that it could have operated consistently for a few hours and then stopped for good.

The final solution, however, exhibits a more consistent and realistic behavior. We note also that the final solution obtained for this problem is not feasible, failing to meet the demand in the last part of the last hour of expected production. For this problem, NOMAD reached the maximum number of blackbox evaluations before it was able to find a single feasible solution.

Table 3.4 shows that despite having found no feasible solution, the level of infeasibility was greatly reduced during the optimization. Looking at Figure 3.7, we see that one way to do

Table 3.4 Comparison of the feasibility of the initial and final solutions of Problem 3.

	initial sol.	**final sol.**
C_1	-1.40×10^5	-1.82×10^5
C_2	**70.57**	**6.53**
C_3	-128.9	-94.37
C_4	-4.5	-6.61
C_5	0	0
C_6	-7.29×10^7	-2.41×10^8
C_7	-221.0	-325.5
C_8	-31.68	0
C_9	-44.20	-0.772
C_{10}	-0.015	-0.013
C_{11}	-7.82	-5.22
C_{12}	-77.97	-66.98

this could be done by slightly increasing the size of the storage and possibly also the energy input from the collector. Looking at constraint C_1 which gives an upper bound to the size of the heliostat field, we see that it is not yet saturated.

Problem 4 consists in minimizing the total cost required for a power plant to be able to generate 25MW between 3 p.m. and 9 p.m. At the difference of Problem 3, this one also uses the NTU-effectiveness heat exchanger model to simulate the performance of the steam generator. Figure 3.8 shows the difference between the initial and final solutions.

We note that the initial solution for Problem 4 is not feasible. We see from Figure 3.8 that the heliostat field of the initial solution is much smaller than that of the final solution, and that its resulting concentrated power is much lower. Another important fact is that the temperature of the molten salt at the steam generator outlet for the initial solution is very high. This means that the efficiency of the heat exchanger is very low, and the molten salt exits it with still a lot of energy left in it. Figure 3.8 e) also shows where part of the infeasibility of the initial solution comes from: the turbine used has a maximum capacity of 10MW, which can never meet the 25MW demand. Figure 3.8 c) also shows that the storage reaches its maximal capacity around noon, which means that lots of energy from the heliostat field cannot be stored and is simply lost. The storage being too small, it also runs out before the simulation ends.

Looking at the final solution, we see that many of these shortcomings are fixed: the steam generator outlet temperature is low, the storage is not emptied before the end of the day, and the power demand is met completely. As in Problem 3, the entire evaluation budget was

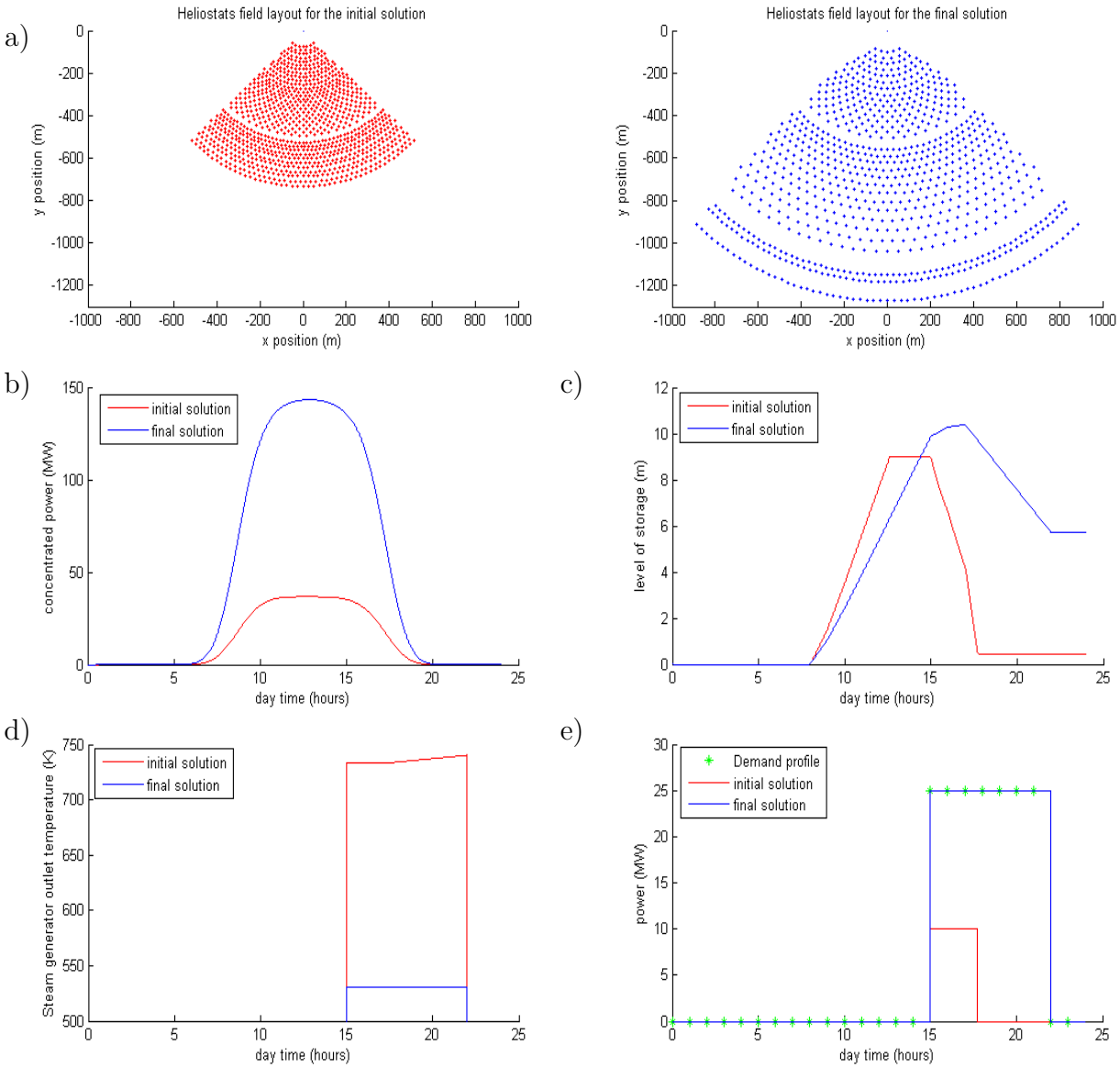

Figure 3.8 Differences between initial and final solutions of Problem 4: a) heliostat fields, b) comparison of the hourly concentrated power, c) level of hot storages, d) steam generator outlet temperatures, e) power production and demand.

reached before NOMAD converged. We can see, simply by looking at the level of the storage at the end of the simulation, that while this solution is feasible, it is most likely not optimal, in that there is an excess amount of energy that is generated. Although a feasible solution was found for this problem, no convergence graph is added because most of the optimization was spent looking for feasible solutions, of which only 4 were found.

Table 3.5 highlights the improvement of the feasibility achieved through the optimization. We see that the main problem with the initial solution is the constraint C_2, which verifies

the ability of the solution to meet the demand. Constraint C_5 is also violated but does not impact the simulation.

Table 3.5 Comparison of the feasibility of the initial and final solutions of Problem 4.

	initial sol.	**final sol.**
C_1	-1.56×10^6	-1.37×10^5
C_2	**84.5**	0
C_3	-132.0	-138.9
C_4	-4.5	-7.142
C_5	**3**	0
C_6	-2.03×10^8	-1.98×10^8
C_7	-386.1	-403.0
C_8	-63.64	-80.09
C_9	-65.00	-35.56
C_{10}	-0.0015	-0.0018
C_{11}	-6.266	-12.81
C_{12}	-97.00	-40.12
C_{13}	-0.134	-0.147
C_{14}	-0.001	-2.43×10^{-4}
C_{15}	-0.0005	-0.0146
C_{16}	-9.21×10^6	-3.08×10^8

Problem 5 consists in maximizing the satisfaction of a constant demand of 12MW over a period of 30 days with an inconsistent solar input, and for a maximum budget of 100M$. The provided initial solution is not feasible. The difference between the generated power of the initial and final solutions is shown on Figure 3.9.

First we note that the final solution suffers from the same problem as previously seen: repeated starts and stops of the turbine caused by the greedy operating strategy and the lack of penalty imposed for turbine starts. It is worth noting, though, that even with a better operating strategy, the resulting objective function would likely be similar for many solutions.

We see in Figure 3.9 b) that the molten salt temperature at the steam generator outlet is too low in the initial solution. This is corroborated by the value of constraint C_5 for the initial solution in Table 3.6, which verifies that the temperature of the molten salt never drops below its melting point. This problem is fixed in the final solution.

Despite having used the entire budget of evaluations, the best values obtained for the objective function are still low (demand is not met in a proportion higher than 28%). The convergence graph of this problem shown on Figure 3.10 shows a difficult optimization. After having found a first feasible solution, the best value for the objective function is barely improved.

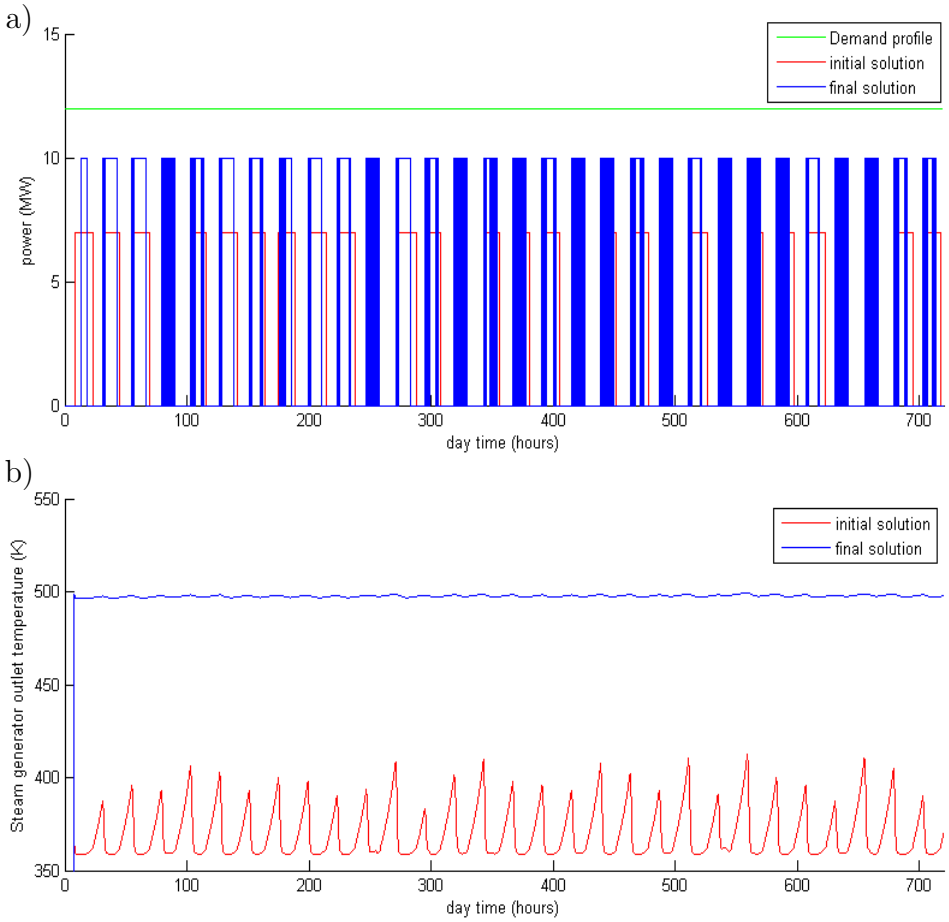

Figure 3.9 Differences between initial and final solutions of Problem 5: a) generated power, b) steam generator molten salt outlet temperature.

Table 3.6 Comparison of the feasibility of the initial and final solutions of Problem 5.

	initial sol.	**final sol.**
C_1	-6.84×10^7	-1.54×10^4
C_2	**3.47**×10^6	-1.36×10^8
C_3	-343.362	-448.1
C_4	0	-32.36
C_5	**136.365**	-1.162
C_6	-0.003×10^8	-0.0019
C_7	-8.872	-8.454
C_8	-97	-146.6
C_9	**1.384**	-0.0275
C_{10}	-0.027	-0.0046
C_{11}	-0.003	-0.0095
C_{12}	-4.034×10^7	-1.832×10^8

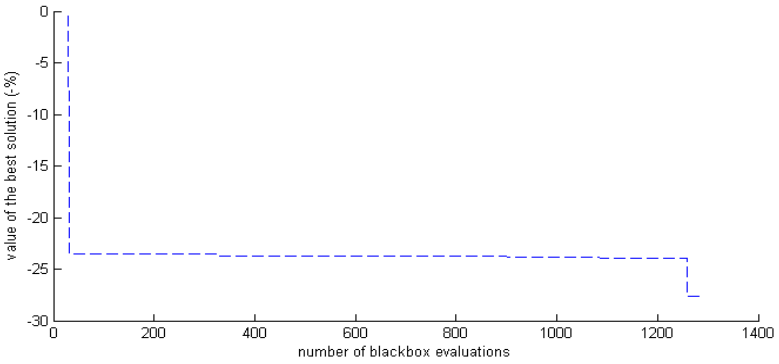

Figure 3.10 Convergence graph for Problem 5.

As seen in Figure 3.9 a), the selected turbine for the final solutions is one with a maximal power output of 10MW. The smaller turbines available for selection are separated by a large gap in power output, and they account for an important part of the total investment cost. It might be the case that the budget constraint for this problem was too tight, so that it was impossible for NOMAD to select a bigger turbine. Even with a different turbine, the fact that we see the power production alternating between stops and starts indicates that the storage is depleted even before the heliostat field stops generating power. This means that the collector field is also unable to collect enough energy. Yet the value of the budget constraint C_1 for the final solution shows that the budget of 100M$ is used in a proportion of 99.99%. This problem could be improved by increasing the budget constraint so that more functional solutions may be tested.

Problem 6 consists in minimizing the total cost of the storage units while still ensuring that a predetermined power plant is able to sustain a consistent power output for 24 hours. Only the thermal storage is optimized. The problem starts with an infeasible solution. Figure 3.11 shows the differences between the initial and final solutions.

For this problem, the storage starts at 50% capacity, but must end the simulated period with at least as much hot molten salt inventory as it started, in order to ensure sustainability over several days. As we can see on Figure 3.11 b), the initial solution fails to meet the demand. The initial molten salt inventory is insufficient to maintain the power output until the heliostat field starts gathering energy, and the turbine has to stop. Later in the day, once the sun is gone, the small storage is emptied quickly and the power has to stop. Thus at least two constraints are violated: the demand, and the requirement that the storage finishes with as much molten salt as it started.

a)

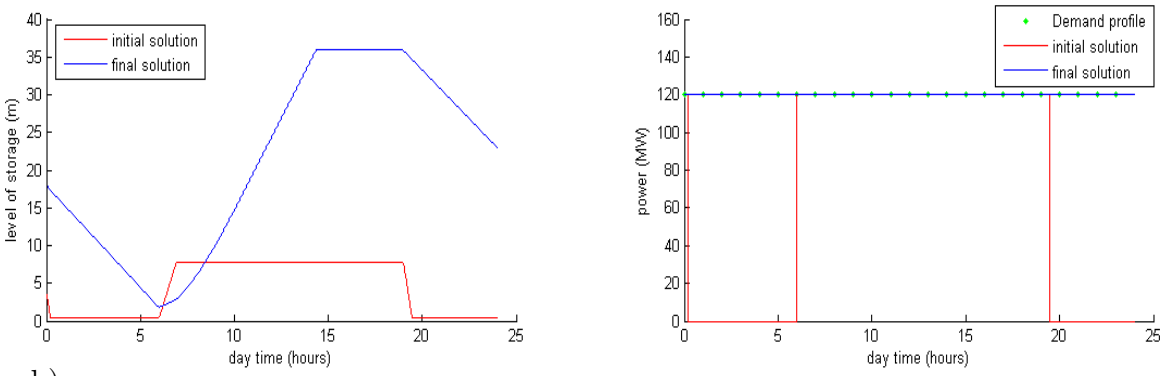

b)

Figure 3.11 Differences between initial and final solutions of Problem 6: a) hot storage level, b) generated power.

We see that the final solution uses a much larger storage and manages to contain enough energy to keep the turbine going until the end of the simulation.

Table 3.7 Comparison of the feasibility of the initial and final solutions of Problem 6.

	initial sol.	**final sol.**
C_1	**43.08**	0
C_2	0	0
C_3	0	0
C_4	0	0
C_5	0	0
C_6	**44.99**	-14.09

As reported in Table 3.2, the optimization for Problem 6 reaches convergence well within the evaluations budget. This can be seen on the convergence graph of Figure 3.12. This suggests that this solution might be a local minimizer.

Two things about the final solution suggest that this problem could be better tuned: the fact that the initial molten salt inventory is set as a ratio of its capacity makes it dependent on the sheer size of the storage, and the fact that it reaches its maximal capacity well before the heliostat field stops gathering energy and still ends the simulation with an exceeding amount of molten salt shows that the solar multiple (the ratio of the energy gathered by the collector field and the energy generated) might be too high for this problem. The size of the storage seems to be determined only by the fact that increasing its size also increases the amount of molten stored when the simulation starts, which would explain the high number of saturated variables (insulation is reduced to the bare minimum because it is useless given the fact that the system receives energy in excess).

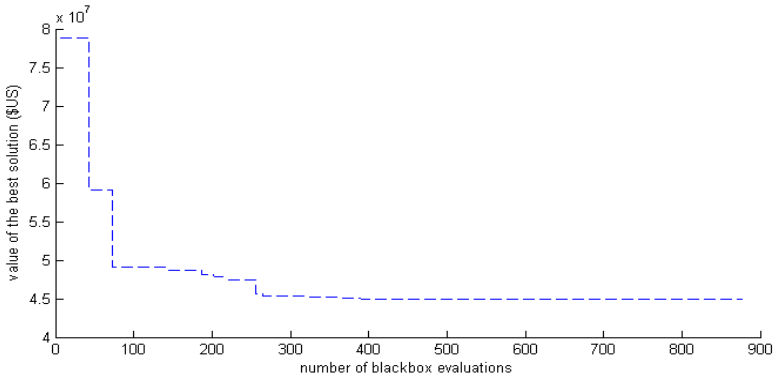

Figure 3.12 Convergence graph for Problem 6.

Problem 7 consists in maximizing the amount of energy collected by the central receiver for a predetermined heliostat field. The initial solution is feasible, and the amount of energy absorbed is assessed by considering the mass of molten salt that can be heated within a day for a given set of design parameters. Figure 3.13 shows the differences in the performance of the two solutions.

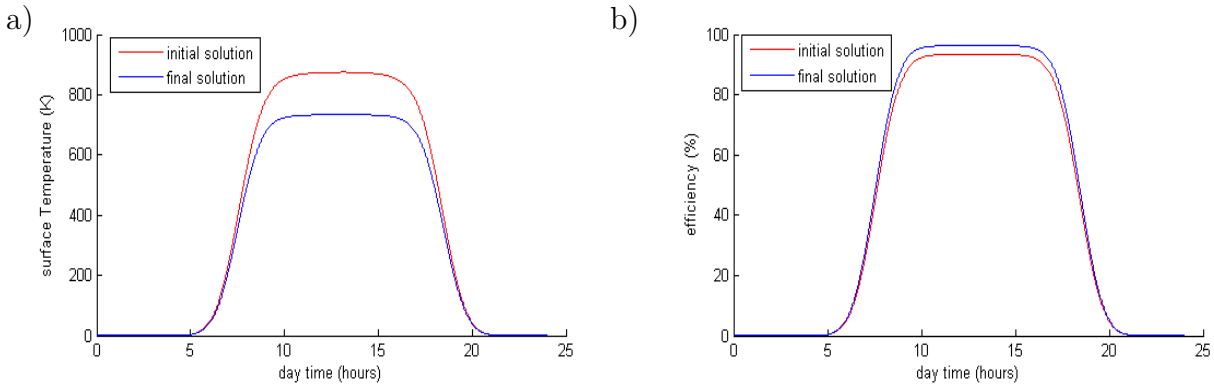

Figure 3.13 Differences between initial and final solutions of Problem 7: a) receiver surface temperature, b) receiver efficiency.

The initial solution reaches higher receiver surface temperatures. This causes increased heat losses to the exterior. This is reflected by the lower receiver efficiency observed on Figure 3.13 b). While the difference in surface temperature is substantial, the variation in the overall receiver efficiency remains around 3%. Figure 3.14 shows the convergence graph for Problem 7.

Problems 8 and 9

NOMAD solves bi-objective problems by finding the set of non-dominated feasible solu-

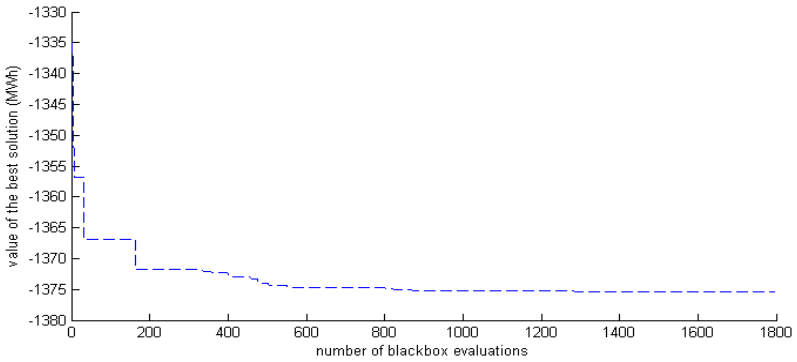

Figure 3.14 Convergence graph for Problem 7.

tions, that is, those for which no other solution is found that have a better value for both objectives or for which at least one objective is better without degrading the other. It does so by using the BIMADS algorithm [5]. Solutions that meet this requirement are said to be Pareto optimal, and form a set called the Pareto front. Figure 3.15 shows the results of the bi-objective optimizations performed for Problems 8 and 9. The full budget of 5000 blackbox evaluations was used in both cases.

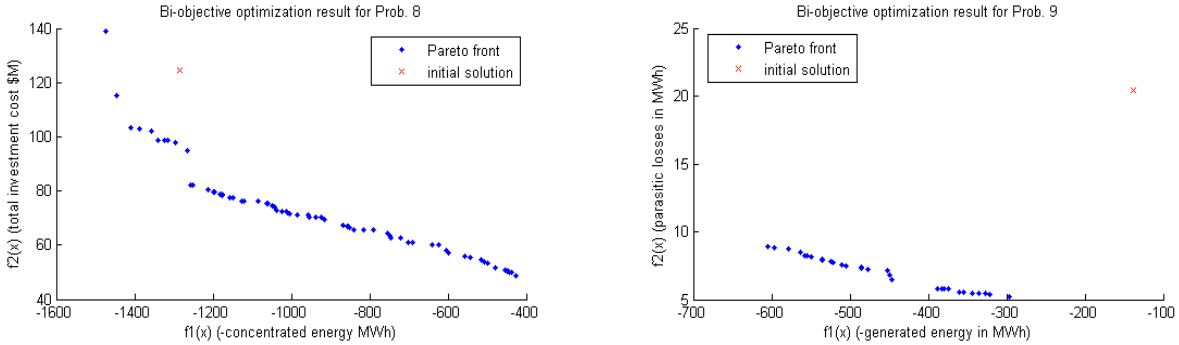

Figure 3.15 Starting points and Pareto fronts obtained following a default bi-objective optimization with NOMAD: Problem 8 on the left, Problem 9 on the right.

CHAPTER 4 CONCLUSION

A new family of 9 blackbox optimization problems has been proposed as a benchmark to test the performance of blackbox solvers. The problems it contains offer a wide range of complexity in terms of the number and type of variables (5 to 29, continuous, discrete and categories) and constraints they use (6 to 17, continuous and binary), and their number of objective functions (single and bi-objective). In order to reflect the complexity of real engineering problems, an original high level model of an electrical CSP plant was implemented. The model simulates each of the main components of a CSP plant using a molten salt thermal storage and a central receiver tower with an heliostat field as the optical collector system. The model proposed considers the effects of shadowing, blocking, spillage losses and atmospheric scattering, when evaluating the heliostat field performance. The molten salt cycle simulates the heat losses occurring in the storage and receiver units, and an approximative model of a shell-and-tubes heat exchanger can be used to simulate the efficiency of the steam generator. The powerblock simulates a basic Rankine power cycle and uses a simple predictive model to determine the efficiency of a steam turbine.

The validity and reliability of the problems was verified by performing a default optimization run with a maximum budget of 5000 evaluations with the NOMAD software. We show that in all cases, the results of the optimization does not lead to trivial solutions and that the blackbox does not fail to compute at a frequency that would make it unusable.

4.1 Limitations

The goal of this project was first and foremost to implement a functional simulation model as to allow the creation of a diverse set of blackbox optimization problems. With that in mind, the main concerns were not about the actual accuracy of the model, to the effect that the modeling of some parts of the model, namely the steam generator and the parasitic loads, were acceptably modeled with no great accuracy with the sole objective of increasing the diversity of the problems.

Conversely, while the heliostat field model considers most of the contributing factors to an optical collector's efficiency under ideal operating conditions, it is also the part of the code that is the most time-consuming to simulate, to the effect that the size of the instances has to be limited in almost every problem, and the precision of the Monte-Carlo integral kept low, to ensure that the blackbox executions tested by the solvers remain reasonably short (a

few minutes).

Finally, the model does not offer any option to dictate an operating strategy for the powerplant. As described in earlier sections, the powerplant operates with a greedy strategy, producing power as soon as it has the thermal resources to do so, which can lead to unrealistic instances in which a turbine will continually shift between no production and its maximum power for every time interval. This can cause some solutions to exhibit interesting values in terms of blackbox output, but be completely impractical.

While fixing these problems may seem compelling, one must also keep in mind that the primary objective of this work is to provide a benchmark for the optimization community. The resources put into this project did not entail the development of a highly accurate predictive model for the planning of actual CSP projects. In fact, there already exist some sophisticated softwares (SOLERGY, SAM, DELSOL) to estimate the performances of solar energy applications.

4.2 Future work

While remaining strictly concerned with the benchmarking aspect of this project, some improvements could still be made to the code so that it is more reliable and runs faster. First, the Monte-Carlo integral method to evaluate the heliostat field performance could be replaced by a deterministic method that would send sunrays exclusively on the heliostats using a discretization method as used by Ewert and Navarro [21], which would greatly reduce the amount of sunrays objects necessary, many of which, with the current method, are simply missing all heliostats and taking up even more computation time as a result. Secondly, the blackbox could be adapted to allow parallel executions.

More importantly, the main focus will be to spread the new benchmark to the blackbox optimization community and use it to work on improving the current algorithms in their ability to solve engineering problems.

BIBLIOGRAPHY

[1] M.A. Abramson, C. Audet, G. Couture, J.E. Dennis, Jr., S. Le Digabel, and C. Tribes. The NOMAD project. Software available at `http://www.gerad.ca/nomad`.

[2] C.A. Amadei, G. Allesina, P. Tartarini, and W. Yuting. Simulation of gemasolar-based solar tower plants for the chinese energy market: Influence of plant downsizing and location change. *Renewable Energy*, 55:366–373, 2013.

[3] C. Audet. A survey on direct search methods for blackbox optimization and their applications. In *Mathematics Without Boundaries*, pages 31–56. Springer, 2014.

[4] C. Audet and J.E. Dennis Jr. Mesh adaptive direct search algorithms for constrained optimization. *SIAM Journal on optimization*, 17(1):188–217, 2006.

[5] C. Audet, G. Savard, and W. Zghal. Multiobjective optimization through a series of single-objective formulations. *SIAM Journal on Optimization*, 19(1):188–210, 2008.

[6] A. L. Ávila-Marín. Volumetric receivers in solar thermal power plants with central receiver system technology: a review. *Solar Energy*, 85(5):891–910, 2011.

[7] A. Bahadori and H. B. Vuthaluru. Estimation of performance of steam turbines using a simple predictive tool. *Applied Thermal Engineering*, 30(13):1832–1838, 2010.

[8] J. Ballestrín and A. Marzo. Solar radiation attenuation in solar tower plants. *Solar Energy*, 86(1):388–392, 2012.

[9] D. Barlev, R. Vidu, and P. Stroeve. Innovation in concentrated solar power. *Solar Energy Materials and Solar Cells*, 95(10):2703–2725, 2011.

[10] H. Bjorn Putten. La situation energetique mondiale la bifurcation regionale des defis vers un monde electrique decarbonne. In *Institut de l'énergie Trottier*, 2014.

[11] S.-J. Bode and P. Gauché. Review of optical software for use in concentrating solar power systems. In *South African Solar Energy Conference, Stellenbosch*, 2012.

[12] R. W Bradshaw, D. B Dawson, W. De La Rosa, R. Gilbert, S. H Goods, M. J. Hale, P. Jacobs, S. A Jones, G. J Kolb, J. E Pacheco, et al. Final test and evaluation results from the solar two project. Technical report, Sandia National Labs., Albuquerque, NM (US); Sandia National Labs., Livermore, CA (US), 2002.

[13] J. Burgaleta, S. Arias, and D. Ramirez. Gemasolar, the first tower thermosolar commercial plant with molten salt storage. In *SolarPA-CES 2012 International Conference, Marrakech, Morocco, Sept*, pages 11–14, 2012.

[14] C. Burroughs. Sandia, stirling energy systems set new world record for solar-to-grid conversion efficiency, february 2008.

[15] E. Carrizosa, C. Domínguez-Bravo, E. Fernández-Cara, and M. Quero. An optimization approach to the design of multi-size heliostat fields. Technical report, Department of Statistics and Operations Research University of Seville, Spain, 2014.

[16] Y. A. Cengel, S. Klein, and W. Beckman. *Heat transfer: a practical approach*. WBC McGraw-Hill Boston, 1998.

[17] T.D. Choi and C. T. Kelley. Superlinear convergence and implicit filtering. *SIAM Journal on Optimization*, 10(4):1149–1162, 2000.

[18] F.J. Collado and J.A. Turégano. Calculation of the annual thermal energy supplied by a defined heliostat field. *Solar Energy*, 42(2):149–165, 1989.

[19] J. A. Duffie and W. A. Beckman. *Solar engineering of thermal processes*. John Wiley & Sons, 2013.

[20] eSolar. Solar thermal enhanced oil recovery, 2015.

[21] M. Ewert and O Navarro Fuentes. Modelling and simulation of a solar tower power plant.

[22] K.R. Fowler, J.P. Reese, C.E. Kees, J.E. Dennis, C.T. Kelley, C.T. Miller, C. Audet, A.J. Booker, G. Couture, R. W. Darwin, et al. Comparison of derivative-free optimization methods for groundwater supply and hydraulic capture community problems. *Advances in Water Resources*, 31(5):743–757, 2008.

[23] E. S. Gaddis and V. Gnielinski. Pressure drop on the shell side of shell-and-tube heat exchangers with segmental baffles. *Chemical Engineering and Processing: Process Intensification*, 36(2):149–159, 1997.

[24] A. Gastli, Y. Charabi, and S. Zekri. Gis based assessment of combined csp electric power and seawater desalination plant for duqum oman. *Renewable and Sustainable Energy Reviews*, 14(2):821–827, 2010.

[25] N. Hansen, A. Auger, S. Finck, and R. Ros. Real-parameter black-box optimization benchmarking 2010: Experimental setup. 2010.

[26] C. K. Ho and B. D. Iverson. Review of high-temperature central receiver designs for concentrating solar power. *Renewable and Sustainable Energy Reviews*, 29:835–846, 2014.

[27] K. Holmström. The TOMLAB optimization environment in matlab. 1999.

[28] IESO, January 2015.

[29] Frank P Incropera, P DeWitt David, Theodore L Bergman, and Adrienne S Lavine. Fundamentals of heat and mass transfer 6th edition, 2006, 2006.

[30] G. J. Janz, U. Krebs, H.F. Siegenthaler, and R.P.T. Tomkins. Molten salts: Volume 3 nitrates, nitrites, and mixtures: Electrical conductance, density, viscosity, and surface tension data. *Journal of Physical and Chemical Reference Data*, 1(3):581–746, 1972.

[31] S. A. Kalogirou. *Solar energy engineering: processes and systems*. Academic Press, 2013.

[32] D. A. Kaminski and M. K. Jensen. *Introduction to thermal and fluids engineering*. Wiley New York, 2005.

[33] D. Kearney. Utility-scale power tower solar systems: Performance acceptance test guidelines. *Contract*, 303:275–3000, 2013.

[34] G. J. Kolb, C. K. Ho, T. R. Mancini, and J. A. Gary. Power tower technology roadmap and cost reduction plan. *SAND2011-2419, Sandia National Laboratories, Albuquerque, NM*, 2011.

[35] A. Kribus. A high-efficiency triple cycle for solar power generation. *Solar Energy*, 72(1):1–11, 2002.

[36] M. Laguna, F. Gortázar, M. Gallego, A. Duarte, and R. Martí. A black-box scatter search for optimization problems with integer variables. *Journal of Global Optimization*, 58(3):497–516, 2014.

[37] X. Li, W. Kong, Z. Wang, C. Chang, and F. Bai. Thermal model and thermodynamic performance of molten salt cavity receiver. *Renewable Energy*, 35(5):981–988, 2010.

[38] T. Mancini, P. Heller, B. Butler, B. Osborn, W. Schiel, V. Goldberg, R. Buck, R. Diver, C. Andraka, and J. Moreno. Dish-stirling systems: An overview of development and status. *Journal of Solar Energy Engineering*, 125(2):135–151, 2003.

[39] J. J. Moré and S. M. Wild. Benchmarking derivative-free optimization algorithms. *SIAM Journal on Optimization*, 20(1):172–191, 2009.

[40] NREL. Gemasolar thermosolar plant, 2015.

[41] J. E. Pacheco, H. E. Reilly, J. Gregory, and C. E. Tyner. Summary of the solar two test and evaluation program. 2000.

[42] James E. Pacheco, RW Bradshaw, DB. Dawson, W. De la Rosa, R. Gilbert, SH Goods, MJ. Hale, P. Jacobs, SA. Jones, GJ. Kolb, et al. Final test and evaluation results from the solar two project. *Report No. SAND2002-0120, Sandia National Laboratories, Albuquerque, NM*, 2002.

[43] T. M. Rassias and P. M. Pardalos. *Mathematics Without Boundaries: Surveys in Pure Mathematics*. Number 31-56. Springer, 2014.

[44] R. G. Reddy. Novel molten salts thermal energy storage for concentrating solar power generation. Technical report, The University of Alabama, Tuscaloosa, 2013.

[45] L. M. Rios and N. V. Sahinidis. Derivative-free optimization: a review of algorithms and comparison of software implementations. *Journal of Global Optimization*, 56(3):1247–1293, 2013.

[46] M. Sanchez and M. Romero. Methodology for generation of heliostat field layout in central receiver systems based on yearly normalized energy surfaces. *Solar Energy*, 80(7):861–874, 2006.

[47] S. Schell. Design and evaluation of esolar's heliostat fields. *Solar Energy*, 85(4):614–619, 2011.

[48] P. Schramek and D. R. Mills. Multi-tower solar array. *Solar Energy*, 75(3):249–260, 2003.

[49] A. Segal and M. Epstein. The optics of the solar tower reflector. *Solar Energy*, 69:229–241, 2001.

[50] A. Segal and M. Epstein. Optimized working temperatures of a solar central receiver. *Solar Energy*, 75(6):503–510, 2003.

[51] F.M.F Siala and M.E Elayeb. Mathematical formulation of a graphical method for a no-blocking heliostat field layout. *Renewable Energy*, 23(1):77 – 92, 2001.

[52] AG Siemens. Steam turbines for csp plants. *Published in Germany by Siemens AG. Available online at www.siemens.com*, 2010.

[53] A. Steinfeld and M. Schubnell. Optimum aperture size and operating temperature of a solar cavity-receiver. *Solar Energy*, 50(1):19–25, 1993.

[54] DOE SunShot. Sunshot vision study–chapter 5, 2012.

[55] M. Súri, T. A. Huld, E. D. Dunlop, and H. A. Ossenbrink. Potential of solar electricity generation in the european union member states and candidate countries. *Solar Energy*, 81(10):1295 – 1305, 2007.

[56] Y. Tian and C.-Y. Zhao. A review of solar collectors and thermal energy storage in solar thermal applications. *Applied Energy*, 104:538–553, 2013.

[57] F. Trieb. Global potential of concentrating solar power. In *Conference Proceedings*, 2009.

[58] C. Turchi, M. Mehos, C. K. Ho, and G. J. Kolb. Current and future costs for parabolic trough and power tower systems in the us market. In *Proceedings of the 16th SolarPACES Conference, Perpignan, France*, 2010.

[59] C. S. Turchi and G. A. Heath. Molten salt power tower cost model for the system advisor model (sam). *Contract*, 303:275–3000, 2013.

[60] C. E. Tyner, J. P. Sutherland, and W.R. Gould. Solar two: A molten salt power tower demonstration. *VDI BERICHTE*, 1200:53–53, 1995.

[61] D. Vallentin and P. Viebahn. Economic opportunities resulting from a global deployment of concentrated solar power (csp) technologies - the example of german technology providers. *Energy Policy*, 38(8):4467–4478, 2010.

[62] D. Wilson, S. Cussat-Blanc, S. Rodrigues, and K. Veeramachaneni. 2nd edition of the wind farm layout optimization competition, 2015.

[63] F. Zaversky, J. García-Barberena, M. Sánchez, and D. Astrain. Transient molten salt two-tank thermal storage modeling for csp performance simulations. *Solar Energy*, 93:294–311, 2013.

[64] H. Zhang, Z. Wang, M. Guo, and W. Liang. Cosine efficiency distribution of heliostats field of solar thermal power tower plants. *NOT A JOURNAL - Shenyang Institude of Engineering, China*.

[65] H.L. Zhang, J. Baeyens, J. Degrève, and G. Cacères. Concentrated solar power plants: Review and design methodology. *Renewable and Sustainable Energy Reviews*, 22:466–481, 2013.

APPENDIX A – OPTIMIZATION PROBLEMS DEFINITION

Problem 1 - Maximize heliostats field energy output

This problem runs only the heliostats field model. It uses 9 variables of which 1 is discrete and the others are continuous. The objective is to maximize the energy concentrated on the receiver aperture by the heliostats field in 24 hours, while respecting a $50M budget and a maximum field area. The objective is subject to 5 explicit constraints. Simulation parameters and variables descriptions are shown in Tables A.1 and A.2 respectively.

Table A.1 Simulation parameters for Problem 1.

parameter	**symbol**	**value**
day	n	100
duration		24 hours
latitude	ϕ	44.95°
maximum budget	C_{cost}	$50M
maximum field surface	C_{sur}	$1.95 \times 10^6 m^2$

Table A.2 List of variables for Problem 1.

variable	**symbol**	**type**	**unit**	**lower bound**	**upper bound**
heliostats length	l	con.	m	1	40
heliostats width	w	con.	m	1	40
receiver aperture height	H_{Re}	con.	m	1	30
receiver aperture width	W_{Re}	con.	m	1	30
tower height	H_T	con.	m	20	250
number of heliostats	N_h	dis.		1	∞
field angular width	θ_{field}	con.	$^{\circ}$	1	89
min. distance from tower	R_{min}	con.	H_T	0	20
max. distance from tower	R_{max}	con.	H_T	1	20

The objective function $F(x)$ for this problem is the total energy gathered over a period of 24 hours.

$$F(x) = -\int_{t_0}^{t_f} P(x,t)dt.$$

In fact, the heliostats field model returns a vector with the power output for the field calculated for each hour. Thus the actual value of the objective function is a finite sum. In order to get better precision, the function is smoothed by the minute using a Gaussian smoothing

kernel.

$$
\begin{aligned}
F(x) &= -\sum_{i=1}^{1440} P_{smooth}(x,t_i) \times \Delta t \\
P_{smooth}(x,t_i) &= \frac{\sum_{j=1}^{24} P(x,t_j) e^{\frac{-(t_i-t_j)^2}{2}}}{\sum_{j=1}^{24} e^{\frac{-(t_i-t_j)^2}{2}}} \\
t_i &= i\Delta t \\
t_j &= i\Delta t \times 60 \\
\Delta t &= 60 seconds.
\end{aligned}
\tag{A.1}
$$

The objective function is subject to 5 constraints, 2 of which are related to the scenario, and 3 are feasibility constraints. The complete expression for each constraint are listed below.

Constraint C_1 is the budget. The investment cost for the collector field is obtain by summing the costs of the heliostats, the tower, and the receiver. Each cost is obtained from the economic model proposed in Chapter 3:

$$C_1(x) = N_h C_{hel}(x) + C_T(x) + C_{Re}(x) - C_{cost}.$$

Constraint C_2 is the field's surface. The surface is calculated a priori.

$$
\begin{aligned}
C_2(x) &= A_{field}(x) - C_{sur} \\
A_{field} &= \pi \left((R_{max} H_T)^2 - (R_{min} H_T)^2 \right) \frac{2\theta_{field}}{360}.
\end{aligned}
$$

Constraint C_3 imposes a minimum tower size related to the heliostats length. The tower has to be at least twice as high as heliostats. C_3 is verified a priori:

$$C_3(x) = 2l - H_T.$$

Constraint C_4 ensures that R_{min} is lesser than R_{max}. C_4 is verified a priori:

$$C_4(x) = R_{min} - R_{max}.$$

Constraint C_5 ensures that N_h heliostats can fit in the field. C_5 is verified once the field has been generated:

$$C_5(x) = N_h - N_{hel}$$

N_{hel} is the number of heliostats generated in the grid.

Problem 2 - Minimize the heliostats field surface

This problem runs the whole power plant model and uses the idealized model for the heat exchanger. It uses 14 variables of which 2 are discrete and the others are continuous. The objective is to minimize the heliostats field surface while satisfying the power demand peaking at 20MW and respecting a $300M budget. The objective is subject to 13 explicit constraints. Simulation parameters and variables descriptions are shown in Tables A.3 and A.4 respectively.

Table A.3 Simulation parameters for Problem 2.

parameter	**symbol**	**value**
day	n	180
duration		72 hours
latitude	ϕ	37.55°
demand profile		3
peak demand	P_{dem}	20 MW
storage start up		50%
hot storage diameter	D_{HS}	23 m
hot storage height	H_{HS}	10.5 m
hot storage insulation	d_{HS}	0.3 m
cold storage insulation	d_{CS}	0.2 m
steam generator out. T	$T_{Sg,o}$	595 K
steam turbine	ST	3 (ST-300)
maximum budget	C_{cost}	$300M
maximum field surface	C_{sur}	$4 \times 10^6 m^2$
demand satisfaction	C_{dem}	100%
parasitic loads	C_{par}	18%

The objective function $F(x)$ for this problem is simply the total area of the heliostats field in m^2.

$$F(x) = \pi \left((R_{max} H_T)^2 - (R_{min} H_T)^2 \right) \frac{2\theta_{field}}{360}. \tag{A.2}$$

The objective function is subject to 13 constraints, 3 of which are related to the scenario, and 10 are feasibility constraints.The complete expression for each constraint are listed below.

Table A.4 List of variables for Problem 2.

variable	**symbol**	**type**	**unit**	**lower bound**	**upper bound**
heliostats length	l	con.	m	1	40
heliostats width	w	con.	m	1	40
receiver aperture height	H_{Re}	con.	m	1	30
receiver aperture width	W_{Re}	con.	m	1	30
tower height	H_T	con.	m	20	250
number of heliostats	N_h	dis.		1	∞
field angular width	θ_{field}	con.	$^\circ$	1	89
min. distance from tower	R_{min}	con.	H_T	0	20
max. distance from tower	R_{max}	con.	H_T	1	20
central receiver outlet T	$T_{Re,o}$	con.	K	595	1000
receiver N of tubes	$N_{Re,tubes}$	dis.	1	-	
receiver insulation	d_{Re}	con.	m	0.01	2
receiver tubes inner D	$D_{Re,in}$	con.	m	0.005	0.1
receiver tubes outer D	$D_{Re,o}$	con.	m	0.005	0.1

Constraint C_1 is the field surface. Since the size of the field influences greatly the time of simulation, an upper bound is set to the field's surface so that no configurations are tested that would require an unreasonable amount of time:

$$C_1(x) = F(x) - C_{sur}.$$

Constraint C_2 ensures that the demand profile is met at all time

$$C_2(x) = C_{dem} - \frac{t_{met}(x)}{t_{total}}$$

t_{met} is the amount of time intervals when the demand was met

t_{total} is the total simulated time (72 hours).

Constraint C_3 is the budget. The investment cost for the collector field is obtained by summing the costs of the components of the whole power plant. Each cost is obtained from the economic model proposed in Chapter 3:

$$C_3(x) = N_h C_{hel}(x) + C_T(x) + C_{Re}(x) + C_{stor} + C_{Sg}(x) + C_{ST} - C_{cost}.$$

Constraint C_4 imposes a minimum tower size related to the heliostats length. The tower has to be at least twice as high as heliostats. C_4 is verified a priori.

$$C_4(x) = 2l - H_T.$$

Constraint C_5 ensures that R_{min} is lesser than R_{max}. C_4 is verified a priori.

$$C_5(x) = R_{min} - R_{max}.$$

Constraint C_6 ensures that N_h heliostats can fit in the field. C_6 is verified once the field has been generated.

$$C_6(x) = N_h - N_{hel}.$$

N_{hel} is the number of heliostats generated in the grid

Constraint C_7 verifies that the pressure in the receiver tubes does not exceed their yield stress at any moment. The pressure and yield are computed as described in Section 2.3.3:

$$C_7(x) = P_{max}(x) - P_{yield}$$

P_{max} is the maximum pressure attained in tubes during simulation

P_{yield} is the pressure that causes constraints in tubes steel to reach yield point.

Constraints $C_{8,9,10}$ ensure that the temperature of the molten salt never drops below its melting point. C_8 is for the hot storage, C_9 is for the cold storage, and C_{10} is for the steam generator outlet:

$$C_i(x) = C_{melt} - C_{min,i}(x).$$

C_{melt} is the melting point of the molten salt.

$C_{min,i}$ is the minimum temperature reached at location i during the simulation.

Constraint C_{11} verifies that the values entered for the tubes inner diameter is smaller than that of the outer diameter. C_{11} is verified a priori.

$$C_{11}(x) = D_{Re,in} - D_{Re,o}.$$

Constraint C_{12} verifies that the number of tubes $N_{Re,tubes}$ fit inside the receiver. C_{12} is verified a priori.

$$C_{12}(x) = N_{Re,tubes} D_{Re,o} - \pi W_{Re}/2.$$

Constraint C_{13} verifies that the receiver outlet temperature $T_{Re,o}$ is superior to that of the turbine's inlet steam. C_{13} is verified a priori.

$$C_{13}(x) = T_{ST,in} - T_{Re,o}.$$

Problem 3 - Minimize total investment cost

This problem simulates the whole power plant and uses the idealized model for the steam generator. It uses 20 variables of which 2 are discrete, one is a categorical variable and 17 are continuous. The objective is to minimize the total investment cost while satisfying the demand and respecting a maximum field size. 3 consecutive days are simulated and the power plant is required to provide constant 10MW during peak hours, between noon and 6 p.m. The objective is subject to 12 explicit constraints. Simulation parameters and variables descriptions are shown in Tables A.5 and A.6 respectively.

Table A.5 Simulation parameters for Problem 3.

parameter	**symbol**	**value**
day	n	1
duration		72 hours
latitude	ϕ	35.$^\circ$
demand profile		1
start time	t_{start}	3 p.m.
stop time	t_{stop}	9 p.m.
peak demand	P_{dem}	10 MW
storage start up		0%
maximum field surface	C_{sur}	$7 \times 10^5 m^2$
demand satisfaction	C_{dem}	100%
parasitic loads	C_{par}	18%

The objective function $F(x)$ for this problem is the total investment cost for the solution, as computed by the economical model described in Section 2.3.1:

$$F(x) = Cost(x). \tag{A.3}$$

The objective is subject to 12 constraints, 2 of which are related to the scenario, and 10 are

Table A.6 List of variables for Problem 3.

variable	**symbol**	**type**	**unit**	**lower bound**	**upper bound**
heliostats length	l	con.	m	1	40
heliostats width	w	con.	m	1	40
receiver aperture height	H_{Re}	con.	m	1	30
receiver aperture width	W_{Re}	con.	m	1	30
tower height	H_T	con.	m	20	250
number of heliostats	N_h	dis.		1	∞
field angular width	θ_{field}	con.	$^\circ$	1	89
min. distance from tower	R_{min}	con.	H_T	0	20
max. distance from tower	R_{max}	con.	H_T	1	20
central receiver outlet T	$T_{Re,o}$	con.	K	595	1000
receiver N of tubes	$N_{Re,tubes}$	dis.	-	1	-
receiver insulation	d_{Re}	con.	m	0.01	2
receiver tubes inner D	$D_{Re,in}$	con.	m	0.005	0.1
receiver tubes outer D	$D_{Re,o}$	con.	m	0.005	0.1
hot storage diameter	D_{HS}	con.	m	1	30
hot storage height	H_{HS}	con.	m	1	50
hot storage insulation	d_{HS}	con.	m	0.01	3
cold storage insulation	d_{CS}	con.	m	0.01	3
steam generator outlet T	$T_{Sg,o}$	con.	K	495	650
steam turbine	ST	cat.		1	8

feasibility constraints. The complete expression for each constraint are listed below.

Constraint C_1 is the field surface. Since the size of the field influences greatly the time of simulation, an upper bound is set to the field's surface so that no configurations are tested that would require an unreasonable amount of time:

$$C_1(x) = \pi \left((R_{max} H_T)^2 - (R_{min} H_T)^2 \right) \frac{2\theta_{field}}{360} - C_{sur}.$$

Constraint C_2 ensures that the demand profile is met at all time:

$$C_2(x) = C_{dem} - \frac{t_{met}(x)}{t_{total}}.$$

t_{met} is the amount of time intervals when the demand was met.

t_{total} is the total simulated time (72 hours).

Constraint C_3 imposes a minimum tower size related to the heliostats length. The tower has to be at least twice as high as heliostats. C_3 is verified a priori.

$$C_3(x) = 2l - H_T.$$

Constraint C_4 ensures that R_{min} is lesser than R_{max}. C_4 is verified a priori.

$$C_4(x) = R_{min} - R_{max}.$$

Constraint C_5 ensures that N_h heliostats can fit in the field. C_6 is verified once the field has been generated.

$$C_5(x) = N_h - N_{hel}$$

N_{hel} is the number of heliostats generated in the grid.

Constraint C_6 verifies that the pressure in the receiver tubes does not exceed their yield stress at any moment. The pressure and yield are computed as described in Section 2.3.3:

$$C_6(x) = P_{max}(x) - P_{yield}$$

P_{max} is the maximum pressure attained in tubes during the simulation.

P_{yield} is the pressure that causes constraints in tubes steel to reach yield point.

Constraints $C_{7,8,9}$ ensure that the temperature of the molten salt never drops below its melting point. C_7 is for the hot storage, C_8 is for the cold storage, and C_9 is for the steam generator outlet:

$$C_i(x) = C_{melt} - C_{min,i}(x)$$

C_{melt} is the melting point of the molten salt

C_{min} is the minimum temperature reached at location i during the simulation.

Constraint C_{10} verifies that the values entered for the tubes inner diameter is smaller than that of the outer diameter. C_{10} is verified a priori.

$$C_{10}(x) = D_{Re,in} - D_{Re,o}.$$

Constraint C_{11} verifies that the number of tubes $N_{Re,tubes}$ fit inside the receiver. C_{12} is verified a priori.

$$C_{11}(x) = N_{Re,tubes} D_{Re,o} - \pi W_{Re}/2.$$

Constraint C_{12} verifies that the receiver outlet temperature $T_{Re,o}$ is superior to that of the turbine's inlet steam. C_{12} is verified a priori.

$$C_{12}(x) = T_{ST,in}(x) - T_{Re,o}.$$

Problem 4 - Minimize total investment cost with S-n-T heat exchanger

Problem 4 is almost identical to problem 3, but with an increased level of complexity, in that it uses the NTU-effectiveness steam generator model presented in Section 2.2.4 instead of the idealized model. It uses 29 variables of which 6 are discrete, one is a categorical variable and 22 are continuous. The objective is to minimize the total investment cost while satisfying the demand and respecting a maximum field size. The simulation is done over 72 hours and the power plant is required to provide constant 10MW during peak hours, between 3 and 9 p.m. The objective is subject to 16 constraints. Simulation parameters and variables descriptions are shown in Tables A.7 and A.8 respectively.

Table A.7 Simulation parameters for Problem 4.

parameter	**symbol**	**value**
day	n	1
duration		72 hours
latitude	ϕ	35.$^{\circ}$
demand profile		1
start time	t_{start}	3 p.m.
stop time	t_{stop}	9 p.m.
peak demand	P_{dem}	25 MW
storage start up		0%
maximum field surface	C_{sur}	$7 \times 10^5 m^2$
demand satisfaction	C_{dem}	100%
parasitic loads	C_{par}	18%

The objective function $F(x)$ for this problem is the total investment cost for the solution, as computed by the economical model described in Section 2.3.1:

$$F(x) = Cost(x). \tag{A.4}$$

Table A.8 List of variables for Problem 4.

variable	**symbol**	**type**	**unit**	**lower bound**	**upper bound**
heliostats length	l	con.	m	1	40
heliostats width	w	con.	m	1	40
receiver aperture height	H_{Re}	con.	m	1	30
receiver aperture width	W_{Re}	con.	m	1	30
tower height	H_T	con.	m	20	250
number of heliostats	N_h	dis.		1	∞
field angular width	θ_{field}	con.	$^\circ$	1	89
min. distance from tower	R_{min}	con.	H_T	0	20
max. distance from tower	R_{max}	con.	H_T	1	20
central receiver outlet T	$T_{Re,o}$	con.	K	595	1000
receiver N of tubes	$N_{Re,tube}$	dis.	-	1	-
receiver insulation	d_{Re}	con.	m	0.01	2
receiver tubes inner D	$D_{Re,in}$	con.	m	0.005	0.1
receiver tubes outer D	$D_{Re,o}$	con.	m	0.005	0.1
hot storage diameter	D_{HS}	con.	m	1	30
hot storage height	H_{HS}	con.	m	1	50
hot storage insulation	d_{HS}	con.	m	0.01	3
cold storage insulation	d_{CS}	con.	m	0.01	3
cold storage default T	$T_{CS,0}$	con.	K	495	650
steam gen. tubes spacing	S_t	con.	m	0.001	0.3
steam gen. tubes inner D	$D_{Sg,in}$	con.	m	0.005	0.1
steam gen. tubes outer D	$D_{Sg,o}$	con.	m	0.005	0.1
steam gen. tubes length	L_{Sg}	con.	m	0.5	10
steam gen. baffles cut	$H_{Sg,baf}$	con.	m	0.15	0.4
steam gen. Nb of baffles	$N_{Sg,baf}$	dis.	-	2	-
steam gen. Nb of tubes	$N_{Sg,tube}$	dis.	-	1	-
steam gen. shell passes	$N_{Sg,shell}$	dis.		1	10
steam gen. tubes passes	$N_{Sg,pass}$	dis.		1	9
steam turbine	ST	cat.		1	8

This problem uses 16 constraints, 2 of which are related to the scenario, and 14 are feasibility constraints. The complete expressions for each constraint are listed below.

Constraint C_1 is the field surface. Since the size of the field influences greatly the time of simulation, an upper bound is set to the field's surface so that no configurations are tested that would require an unreasonable amount of time:

$$C_1(x) = \pi \left((R_{max} H_T)^2 - (R_{min} H_T)^2 \right) \frac{2\theta_{field}}{360} - C_{sur}.$$

Constraint C_2 ensures that the demand profile is met at all time:

$$C_2(x) = C_{dem} - \frac{t_{met}(x)}{t_{total}}.$$

t_{met} is the amount of time intervals when the demand was met.

t_{total} is the total simulated time (72 hours).

Constraint C_3 imposes a minimum tower size related to the heliostats length. The tower has to be at least twice as high as heliostats. C_4 is verified a priori.

$$C_3(x) = 2l - H_T.$$

Constraint C_4 ensures that R_{min} is lesser than R_{max}. C_4 is verified a priori.

$$C_4(x) = R_{min} - R_{max}.$$

Constraint C_5 ensures that N_h heliostats can fit in the field. C_6 is verified once the field has been generated.

$$C_5(x) = N_h - N_{hel}$$

N_{hel} is the number of heliostats generated in the grid.

Constraint C_6 verifies that the pressure in the receiver tubes does not exceed their yield stress at any moment. The pressure and yield are computed as described in Section 2.3.3:

$$C_6(x) = P_{max}(x) - P_{yield}.$$

P_{max} is the maximum pressure attained in tubes during simulation.

P_{yield} is the pressure that causes constraints in tubes steel to reach yield point.

Constraints $C_{7,8,9}$ ensure that the temperature of the molten salt never drops below its melting point. C_8 is for the hot storage, C_9 is for the cold storage, and C_{10} is for the steam generator outlet:

$$C_i(x) = C_{melt} - C_{min,i}(x).$$

C_{melt} is the melting point of the molten salt.

C_{min} is the minimum temperature reached at location i during the simulation.

Constraint C_{10} verifies that the values entered for the tubes inner diameter is smaller than that of the outer diameter. C_{10} is verified a priori.

$$C_{10}(x) = D_{Re,in} - D_{Re,o}.$$

Constraint C_{11} verifies that the number of tubes $N_{Re,tubes}$ fit inside the receiver. C_{12} is verified a priori.

$$C_{11}(x) = N_{Re,tubes} D_{Re,o} - \pi W_{Re}/2.$$

Constraint C_{12} verifies that the receiver outlet temperature $T_{Re,o}$ is superior to that of the turbine's inlet steam. C_{12} is verified a priori.

$$C_{12}(x) = T_{ST,in}(x) - T_{Re,o}.$$

Constraint C_{13} verifies that the parasitic loads do not account for more than 18% of the energy production using the parasitic load model proposed in Section 2.3.2:

$$C_{13}(x) = \frac{Parx}{E_{total}(x)} - C_{par}.$$

Constraint C_{14} verifies that the steam generator tubes spacing is larger than their diameters. C_{14} is verified a priori.

$$C_{14}(x) = D_{Sg,o} - S_t.$$

Constraint C_{15} verifies that the steam generator tubes inner and outer diameter are consistent. C_{15} is verified a priori.

$$C_{15}(x) = D_{Sg,in} - D_{Sg,o}.$$

Constraint C_{16} verifies that the pressure in the steam generator tubes does not exceed their yield stress at any moment. The pressure and yield are computed as described in Section 2.3.3:

$$C_{16}(x) = P_{max,Sg}(x) - P_{yield}$$

$P_{max,Sg}$ maximum pressure attained in tubes during simulation

P_{yield} pressure that causes stress in tubes steel to reach yield point.

Problem 5 - Maximize the satisfaction of the demand

This problem runs the HTF loop and the powerblock models and substitutes a performance data file to the heliostats field in order to reduce computation time. It uses 18 variables of which 5 are discrete, one is a categorical variable and 14 are continuous. The power plant's performance is simulated over a period of 30 days with an inconsistent field performance analogous to slightly unreliable weather conditions. The objective is to maximize the time for which the power plant is able to operate at nominal capacity. A surrogate model is available for this problem which consists in running the simulation on only a fraction of the 30 days and extrapolating the resulting performance over the 30 days. The objective is subject to 12 explicit constraints. Simulation parameters and variables descriptions are shown in Tables A.9 and A.10 respectively.

Table A.9 Simulation parameters for Problem 5.

parameter	**symbol**	**value**
day	n	30
duration		720 hours
latitude	ϕ	37.5581°
demand profile		1
start time	t_{start}	0 p.m.
stop time	t_{stop}	24 p.m.
peak demand	P_{dem}	10 MW
storage start up		0%
heliostats length	l	2.1336 m
heliostats width	w	3.048 m
tower height	H_T	100 m
receiver aperture height	H_{Re}	6 m
receiver apeture width	W_{Re}	6 m
number of heliostats	N_{hel}	3800
field angular width	θ_{field}	89°
min distance from tower	R_{min}	0.1
max distance from tower	R_{max}	10
maximum cost	C_{cost}	$100M
parasitic loads	C_{par}	18%

The objective function $F(x)$ is total time for which the demand could be met over the entire simulated time period:

$$F(x) = -\frac{t_{met}\frac{t_{met}}{t_{total}}}{t_{total}}. \tag{A.5}$$

This problem uses 12 constraints, of which one is related to the scenario, and 11 are feasibility

Table A.10 List of variables for Problem 5.

variable	**symbol**	**type**	**unit**	**lower bound**	**upper bound**
central receiver outlet T	$T_{Re,o}$	con.	K	595	1000
receiver N of tubes	$N_{Re,tube}$	dis.	-	1	-
receiver insulation	d_{Re}	con.	m	0.01	2
receiver tubes inner D	$D_{Re,in}$	con.	m	0.001	0.2
receiver tubes outer D	$D_{Re,o}$	con.	m	0.001	0.2
hot storage diameter	D_{HS}	con.	m	1	30
hot storage height	H_{HS}	con.	m	1	50
hot storage insulation	d_{HS}	con.	m	0.01	3
cold storage insulation	d_{CS}	con.	m	0.01	3
cold storage default T	$T_{CS,0}$	con.	K	495	650
steam gen. tubes spacing	S_t	con.	m	0.001	0.3
steam gen. tubes inner D	$D_{Sg,in}$	con.	m	0.005	0.1
steam gen. tubes outer D	$D_{Sg,o}$	con.	m	0.005	0.1
steam gen. tubes length	L_{Sg}	con.	m	0.5	10
steam gen. baffle cut	$H_{Sg,baf}$	con.	-	0.15	0.4
steam gen. Nb of baffles	$N_{Sg,baf}$	dis.	-	2	-
steam gen. Nb of tubes	$N_{Sg,tube}$	dis.		1	-
steam gen. shell passes	$N_{Sg,shell}$	dis.		1	10
steam gen. tubes passes	$N_{Sg,pass}$	dis.		1	9
steam turbine	ST	cat.		1	8

constraints. The complete expressions for each constraint are listed below.

Constraint C_1 is the budget. The investment cost for the collector field is obtain by summing the costs of the components of the whole power plant. Each cost is obtained from the economic model proposed in Chapter 3:

$$C_1(x) = C_{hel} + C_T + C_{Re}(x) + C_{stor}(x) + C_{Sg}(x) + C_{ST}(x) - C_{cost}.$$

Constraint C_2 verifies that the pressure in the receiver tubes does not exceed their yield stress at any moment. The pressure and yield are computed as described in Section 2.3.3:

$$C_2(x) = P_{max}(x) - P_{yield}$$

P_{max} maximum pressure attained in tubes during simulation

P_{yield} pressure that causes constraints in tubes steel to reach yield point.

Constraints $C_{3,4,5}$ ensure that the temperature of the molten salt never drops below its melting point. C_3 is for the hot storage, C_4 is for the cold storage, and C_5 is for the steam generator outlet:

$$C_i(x) = C_{melt} - C_{min,i}(x)$$

C_{melt} is the melting point of the molten salt

C_{min} is the minimum temperature reached at location i during the simulation.

Constraint C_6 verifies that the values entered for the tubes inner diameter is smaller than that of the outer diameter. C_{10} is verified a priori.

$$C_6(x) = D_{Re,in} - D_{Re,o}.$$

Constraint C_7 verifies that the number of tubes $N_{Re,tubes}$ fit inside the receiver. C_7 is verified a priori.

$$C_7(x) = N_{Re,tubes} D_{Re,o} - \pi W_{Re}/2.$$

Constraint C_8 verifies that the receiver outlet temperature $T_{Re,o}$ is superior to that of the turbine's inlet steam. C_8 is verified a priori.

$$C_8(x) = T_{ST,in}(x) - T_{Re,o}.$$

Constraint C_9 verifies that the parasitic loads do not account for more than 18% of the energy production using the parasitic load model proposed in Section 2.3.2:

$$C_9(x) = \frac{Parx}{E_{total}(x)} - C_{par}.$$

Constraint C_{10} verifies that the steam generator tubes spacing is larger than their diameters. C_{14} is verified a priori.

$$C_{10}(x) = D_{Sg,o} - S_t.$$

Constraint C_{11} verifies that the steam generator tubes inner and outer diameter are consistent. C_{11} is verified a priori.

$$C_{11}(x) = D_{Sg,in} - D_{Sg,o}.$$

Constraint C_{12} verifies that the pressure in the steam generator tubes does not exceed their yield stress at any moment. The pressure and yield are computed as described in Section 2.3.3:

$$C_{12}(x) = P_{max,Sg}(x) - P_{yield}$$

$P_{max,Sg}$ maximum pressure attained in tubes during simulation

P_{yield} pressure that causes stress in tubes steel to reach yield point.

Problem 6 - Minimize the cost of storage

This problem runs a predetermined power plant using the HTF cycle and powerblock models. It uses 5 continuous variables. The objective is to minimize the cost of the thermal storage units so that the power plant is able to sustain a 100MW electrical power output for a 24 hours period. Since the heliostats field is not being optimized, its hourly power output is read from a prerecorded file instead of being simulated, in order to reduce the computation time. The objective is subject to 6 explicit constraints, 4 of which return binary values. Simulation parameters and variables descriptions are shown in Tables A.11 and A.12 respectively.

Table A.11 Simulation parameters for Problem 6.

parameter	**symbol**	**value**
day	n	1
duration		72 hours
latitude	ϕ	30.05°
demand profile		1
start time	t_{start}	0 p.m.
stop time	t_{stop}	24 p.m.
peak demand	P_{dem}	100 MW
storage start up		50%
heliostats length	l	9 m
heliostats width	w	9 m
tower height	H_T	250 m
receiver aperture height	H_{Re}	9 m
receiver apeture width	W_{Re}	9.5 m
number of heliostats	N_{hel}	12232
field angular width	θ_{field}	65°
min distance from tower	R_{min}	1
max distance from tower	R_{max}	10.5
satisfaction of demand	C_{dem}	100%
type of turbine	ST	5 (ST-600)

Table A.12 List of variables for Problem 6.

variable	symbol	type	unit	lower bound	upper bound
central receiver outlet T	$T_{Re,o}$	con.	K	595	1000
hot storage diameter	D_{HS}	con.	m	1	30
hot storage height	H_{HS}	con.	m	1	50
hot storage insulation	d_{HS}	con.	m	0.01	3
cold storage insulation	d_{CS}	con.	m	0.01	3

The objective function $F(x)$ for this problem is the cost of the storage:

$$F(x) = C_{stor}(x). \tag{A.6}$$

The objective is subject to 5 constraints, one of which is objective-related. The others are feasibility constraints and return binary values. The complete expression for each constraint are listed below.

Constraint C_1 ensures that the demand profile is met at all time.

$$C_1(x) = C_{dem} - \frac{t_{met}(x)}{t_{total}}$$

t_{met} time intervals when the demand was met

t_{total} total simulated time (72 hours)

All of the following constraints return binary values

Constraint C_2 verifies that the pressure in the receiver tubes does not exceed their yield stress at any moment. The pressure and yield are computed as described in Section 2.3.3.

$$C_2(x) = \begin{cases} 0, & \text{if } P_{max}(x) - P_{yield} \leq 0 \\ 1, & \text{if } P_{max}(x) - P_{yield} > 0 \end{cases}$$

P_{max} maximum pressure attained in tubes during simulation

P_{yield} pressure that causes constraints in tubes steel to reach yield point

Constraints $C_{3,4}$ ensure that the temperature of the molten salt never drops below its melting point. C_3 is for the hot storage and C_4 for the cold storage.

$$C_i(x) = \begin{cases} 0, & \text{if } C_{melt} - C_{min,i}(x) \leq 0 \\ 1, & \text{if } C_{melt} - C_{min,i}(x) > 0 \end{cases}$$

C_{melt} is the melting point of the molten salt

C_{min} is the minimum temperature reached at location i during the simulation

Constraint C_5 verifies that the receiver outlet temperature $T_{Re,o}$ is superior to that of the turbine's inlet steam. C_6 is verified a priori.

$$C_5(x) = \begin{cases} 0, & \text{if } T_{ST,in} - T_{Re,o} \leq 0 \\ 1, & \text{if } T_{ST,in} - T_{Re,o} > 0 \end{cases}$$

Constraint C_6 verifies that the storage is at least as full at the end of the simulation as it was at the beginning:

$$C_6(x) = m_{stored,i} - m_{stored,f}.$$

Problem 7 - Maximize receiver efficiency

This problem simulates the heliostats field and the central receiver unit over a 24 hours period. It uses 7 variables, of which one is discrete and the others are continuous. The objective is to maximize the receiver's efficiency. A surrogate version of the model can be used so that a much lower density of sunrays is used to evaluate the field's performance. The objective is subject to 6 binary constraints. Simulation parameters and variables descriptions are shown in Tables A.13 and A.14 respectively.

The objective function $F(x)$ for this problem is the total energy passed to the molten salt via the central receiver:

$$F(x) = -c_{ms} \int \dot{m}_{ms}(t,x) \Delta T_{ms}(t,x) dt. \tag{A.7}$$

The objective is subject to 5 binary constraints. The complete expression for each constraint are listed below.

Table A.13 Simulation parameters for Problem 7.

parameter	**symbol**	**value**
day	n	1
duration		24 hours
latitude	ϕ	30.05°
demand profile		1
start time	t_{start}	0 p.m.
stop time	t_{stop}	24 p.m.
peak demand	P_{dem}	0
storage start up		50%
heliostats length	l	7.5 m
heliostats width	w	7.5 m
tower height	H_T	250 m
receiver aperture height	H_{Re}	8 m
receiver apeture width	W_{Re}	8 m
number of heliostats	N_{hel}	10400
field angular width	θ_{field}	60°
min distance from tower	R_{min}	1
max distance from tower	R_{max}	14

Table A.14 List of variables for Problem 7.

variable	**symbol**	**type**	**unit**	**lower bound**	**upper bound**
aperture height	H_{Re}	con.	m	1	30
aperture width	W_{Re}	con.	m	1	30
insulation thickness	d_{Re}	con.	m	0.01	3
number of tubes	$N_{Re,tube}$	dis.	-	1	-
outlet temperature	$T_{Re,o}$	con.	K	595	1000
tubes inner diameter	D_{in}	con.	m	0.005	0.1
tubes outer diameter	D_o	con.	m	0.005	0.1

Constraint C_1 specifies the maximum cost for the receiver unit:

$$C_1(x) = C_{Re}(x) - C_{cost}$$

t_{met} time intervals when the demand was met

t_{total} total simulated time (72 hours).

All of the following constraints return binary values

Constraint C_2 verifies that the pressure in the receiver tubes does not exceed their yield stress at any moment. The pressure and yield are computed as described in Section 2.3.3:

$$C_2(x) = \begin{cases} 0, & \text{if } P_{max}(x) - P_{yield} \leq 0 \\ 1, & \text{if } P_{max}(x) - P_{yield} > 0 \end{cases}$$

P_{max} maximum pressure attained in tubes during simulation

P_{yield} pressure that causes constraints in tubes steel to reach yield point.

Constraint C_3 verifies that the values entered for the tubes inner diameter is smaller than that of the outer diameter. C_3 is verified a priori.

$$C_3(x) = \begin{cases} 0, & \text{if } D_{Re,in} - D_{Re,o} \leq 0 \\ 1, & \text{if } D_{Re,in} - D_{Re,o} > 0. \end{cases}$$

Constraint C_4 verifies that the receiver outlet temperature $T_{Re,o}$ is superior to that of the turbine's inlet steam. C_4 is verified a priori.

$$C_4(x) = \begin{cases} 0, & \text{if } T_{ST,in} - T_{Re,o} \leq 0 \\ 1, & \text{if } T_{ST,in} - T_{Re,o} > 0. \end{cases}$$

Constraint C_5 verifies that the work to drive the receiver pump dos not exceed 5% of the absorbed energy 2.3.2:

$$C_5(x) = \begin{cases} 0, & \text{if } \frac{Parx}{E_{abs}(x)} - C_{par} \leq 0 \\ 1, & \text{if } \frac{Parx}{E_{abs}(x)} - C_{par} > 0. \end{cases}$$

Constraint C_6 verifies that the parasitic loads do not account for more than 5% of the absorbed energy using the parasitic load model proposed in Section 2.3.2:

$$C_6(x) = \begin{cases} 0, & \text{if } \frac{Parx}{E_{total}(x)} - C_{par} \leq 0 \\ 1, & \text{if } \frac{Parx}{E_{total}(x)} - C_{par} > 0. \end{cases}$$

Problem 8 - Maximize heliostats field output with minimum cost

This problem runs the heliostats field and central receiver models. It uses 13 variables, of which two are discrete and 11 are continuous. This is a bi-objective problem of which the two

objectives are to maximize the amount of energy transfered to the molten salt over a 24 hours period all while minimizing the total cost of the field, tower and receiver. The optimization is conducted over the design parameters of both the heliostats field and the central receiver. The objectives are subject to 8 constraints. Simulation parameters and variables descriptions are shown in Tables A.15 and A.16 respectively.

Table A.15 Simulation parameters for Problem 8.

parameter	**symbol**	**value**
day	n	1
duration		24 hours
latitude	ϕ	30.05°
demand profile		1
start time	t_{start}	0 p.m.
stop time	t_{stop}	24 p.m.
peak demand	P_{dem}	0
receiver outlet temperature	$T_{Re,o}$	1000 K
storage start up		0%
maximum field surface	C_{sur}	$5 \times 10^6 m^2$

Table A.16 List of variables for Problem 8.

variable	**symbol**	**type**	**unit**	**lower bound**	**upper bound**
heliostats length	l	con.	m	1	40
heliostats width	w	con.	m	1	40
receiver aperture height	H_{Re}	con.	m	1	30
receiver aperture width	W_{Re}	con.	m	1	30
tower height	H_T	con.	m	20	250
number of heliostats	N_h	dis.		1	∞
field angular width	θ_{field}	con.	$^{\circ}$	1	89
min. distance form tower	R_{min}	con.	-	0	20
max. distance form tower	R_{max}	con.	-	1	20
receiver N of tubes	$N_{Re,tube}$	dis.	-	1	-
receiver insulation	d_{Re}	con.	m	0.01	2
receiver tubes inner D	$D_{Re,in}$	con.	m	0.005	0.1
receiver tubes outer D	$D_{Re,o}$	con.	m	0.005	0.1

The objective functions $\vec{F}(x)$ for this problem are the total energy passed to the molten salt via the central receiver $F_1(x)$ and the combined cost of the heliostats field, the tower and

receiver $F_2(x)$.

$$\begin{aligned} F_1(x) =& - c_{ms} \int \dot{m}_{ms}(t,x)\Delta T_{ms}(t,x)dt \\ F_2(x) =& N_h C_{hel}(x) + C_T(x) + C_{Re}(\vec{x}). \end{aligned} \tag{A.8}$$

The objectives are subject to 9 constraints, of which the expressions are given below.

Constraint C_1 is the field surface. In order to provide an upper bound to the maximum power that can be gathered, a field surface constraint is imposed:

$$C_1(x) = \pi \left((R_{max} H_T)^2 - (R_{min} H_T)^2 \right) \frac{2\theta_{field}}{360} - C_{sur}.$$

Constraint C_2 imposes a minimum tower size related to the heliostats length. The tower has to be at least twice as high as heliostats. C_2 is verified a priori.

$$C_2(x) = 2l - H_T.$$

Constraint C_3 ensures that R_{min} is lesser than R_{max}. C_3 is verified a priori.

$$C_3(x) = R_{min} - R_{max}.$$

Constraint C_4 ensures that N_h heliostats can fit in the field:

$$C_4(x) = N_h - N_{hel}$$

N_{hel} is the number of heliostats positions generated in the grid.

Constraint C_5 verifies that the pressure in the receiver tubes does not exceed their yield stress at any moment. The pressure and yield are computed as described in Section 2.3.3:

$$C_5(x) = P_{max}(x) - P_{yield}$$

P_{max} maximum pressure reached in the tubes during simulation

P_{yield} pressure that causes constraints in the tubes steel to reach the yield point.

Constraint C_6 verifies that the value entered for the tubes inner diameter is smaller than that of the outer diameter. C_6 is verified a priori.

$$C_6(x) = D_{Re,in} - D_{Re,o}.$$

Constraint C_7 verifies that $N_{Re,tube}$ tubes fit inside the receiver. C_7 is verified a priori.

$$C_7(x) = N_{Re,tube} D_{Re,o} - \pi W_{Re}/2.$$

Constraint C_8 verifies that the solution generates at least a minimum of energy:

$$C_8(x) = C_{energy} - \int P_{out}(t, x)dt.$$

Constraint C_9 verifies that the parasitic loads do not account for more than 20% of the energy production using the parasitic load model proposed in Section 2.3.2:

$$C_9(x) = \frac{Parx}{E_{total}(x)} - C_{par}.$$

Problem 9 - Maximize power and minimize losses

This problem simulates the entire power plant over a single day. It uses 29 variables, of which 6 are discrete, one is a categorical variable and 22 are continuous. This is a bi-objective problem of which the two objectives are to maximize the generated electrical power and minimize the parasitic losses while respecting a $1.2B budget. The objectives are subject to 16 constraints, 12 of which are binary. Simulation parameters and variables descriptions are shown in Tables A.17 and A.18 respectively.

Table A.17 Simulation parameters for Problem 9.

parameter	**symbol**	**value**
day	n	180
duration		24 hours
latitude	ϕ	25°
demand profile		1
start time	t_{start}	0 p.m.
stop time	t_{stop}	24 p.m.
peak demand	P_{dem}	0
storage start up		50%
satisfaction of demand	C_{dem}	100%

Table A.18 List of variables for Problem 9.

variable	**symbol**	**type**	**unit**	**lower bound**	**upper bound**
heliostats length	l	con.	m	1	40
heliostats width	w	con.	m	1	40
receiver aperture height	H_{Re}	con.	m	1	30
receiver aperture width	W_{Re}	con.	m	1	30
tower height	H_T	con.	m	20	250
number of heliostats	N_h	dis.		1	∞
field angular width	θ_{field}	con.	$^\circ$	1	89
min. distance from tower	R_{min}	con.	H_T	0	20
max. distance from tower	R_{max}	con.	H_T	1	20
central receiver outlet T	$T_{Re,o}$	con.	K	595	1000
receiver N of tubes	$N_{Re,tube}$	dis.	1	-	
receiver insulation	d_{Re}	con.	m	0.01	2
receiver tubes inner D	$D_{Re,in}$	con.	m	0.005	0.1
receiver tubes outer D	$D_{Re,o}$	con.	m	0.005	0.1
hot storage diameter	D_{HS}	con.	m	1	30
hot storage height	H_{HS}	con.	m	1	50
hot storage insulation	d_{HS}	con.	m	0.01	3
cold storage insulation	d_{CS}	con.	m	0.01	3
cold storage baseline T	$T_{CS,0}$	con.	K	495	900
steam gen. tubes spacing	S_t	con.	m	0.001	0.3
steam gen. tubes inner D	$D_{Sg,in}$	con.	m	0.005	0.1
steam gen. tubes outer D	$D_{Sg,o}$	con.	m	0.005	0.1
steam gen. tubes length	L_{Sg}	con.	m	0.5	10
steam gen. baffle cut	$H_{Sg,baf}$	con.	-	0.15	0.4
steam gen. Nb of baffles	$N_{Sg,baf}$	dis.	-	2	-
steam gen. Nb of tubes	$N_{Sg,tube}$	dis.		1	-
steam gen. shell passes	$N_{Sg,shell}$	dis.		1	10
steam gen. tubes passes	$N_{Sg,pass}$	dis.		1	9
steam turbine	ST	cat.		1	8

The two objective functions are the total investment cost of the solution $F_1(x)$, as well as the energy used to operate the power plant $F_2(x)$.

In order to limit the computation time and avoid trivial solutions from being attempted, constraints are added to specify a minimum for the energy generated and a maximum for the investment cost. The objectives are subject to a total 17 constraints. The complete expression for each constraint are listed below.

Constraint C_8 verifies that the solution generates at least a minimum of energy:

$$C_8(x) = C_{energy} - \int P_{out}(t,x)dt.$$

The objective functions $\vec{F}(x)$ for this problem are the total energy passed to the molten salt via the central receiver $F_1(x)$ and the combined cost of the heliostats field, the tower and receiver $F_2(x)$.

$$\begin{aligned} F_1(x) &= -\int P_{out}(t,x)dt \\ F_2(x) &= \int P_{par}(t,x)dt. \end{aligned} \tag{A.9}$$

Constraint C_1 is the budget. The investment cost for the collector field is obtain by summing the costs of the components of the whole power plant. Each cost is obtained from the economic model proposed in Chapter 3:

$$C_1(x) = N_h C_{hel}(x) + C_T(x) + C_{Re}(x) + C_{stor} + C_{Sg}(x) + C_{ST} - C_{cost}.$$

Constraint C_2 verifies that the solution generates at least a minimum of energy:

$$C_2(x) = C_{energy} - \int P_{out}(t,x)dt.$$

Constraint C_3 is the field's surface. The surface is calculated a priori.

$$\begin{aligned} C_3(x) &= A_{field}(x) - C_{sur} \\ A_{field} &= \pi \left((R_{max}H_T)^2 - (R_{min}H_T)^2 \right) \frac{2\theta_{field}}{360}. \end{aligned}$$

Constraint C_4 imposes a minimum tower size related to the heliostats length. The tower has to be at least twice as high as heliostats. C_4 is verified a priori:

$$C_4(x) = 2l - H_T.$$

Constraint C_5 ensures that R_{min} is lesser than R_{max}. C_5 is verified a priori:

$$C_5(x) = R_{min} - R_{max}.$$

Constraint C_6 ensures that N_h heliostats can fit in the field. C_6 is verified once the field has been generated:

$$C_6(x) = N_h - N_{hel}$$

N_{hel} is the number of heliostat positions generated in the grid.

Constraint C_7 verifies that the pressure in the receiver tubes does not exceed their yield stress at any moment. The pressure and yield are computed as described in Section 2.3.3:

$$C_7(x) = \begin{cases} 0, & \text{if } P_{max}(x) - P_{yield} \leq 0 \\ 1, & \text{if } P_{max}(x) - P_{yield} > 0. \end{cases}$$

P_{max} is the maximum pressure attained in tubes during simulation.

P_{yield} is the pressure that causes constraints in tubes steel to reach yield point.

Constraints $C_{8,9,10}$ ensure that the temperature of the molten salt never drops below its melting point. C_8 is for the hot storage, C_9 is for the cold storage, and C_{10} is for the steam generator outlet:

$$C_i(x) = \begin{cases} 0, & \text{if } C_{melt} - C_{min,i}(x) \leq 0 \\ 1, & \text{if } C_{melt} - C_{min,i}(x) > 0. \end{cases}$$

C_{melt} is the melting point of the molten salt.

$C_{min,i}$ is the minimum temperature reached at location i during the simulation.

Constraint C_{11} verifies that the values entered for the tubes inner diameter is smaller than that of the outer diameter. C_{11} is verified a priori.

$$C_{11}(x) = D_{Re,in} - D_{Re,o}.$$

Constraint C_{12} verifies that the number of tubes $N_{Re,tubes}$ fit inside the receiver. C_{12} is verified a priori.

$$C_{12}(x) = N_{Re,tubes} D_{Re,o} - \pi W_{Re}/2.$$

Constraint C_{13} verifies that the receiver outlet temperature $T_{Re,o}$ is superior to that of the turbine's inlet steam. C_{13} is verified a priori.

$$C_{13}(x) = T_{ST,in} - T_{Re,o}.$$

Constraint C_{14} verifies that the parasitic loads do not account for more than 18% of the energy production using the parasitic load model proposed in Section 2.3.2:

$$C_{14}(x) = \frac{Parx}{E_{total}(x)} - C_{par}.$$

Constraint C_{15} verifies that the steam generator tubes spacing is larger than their diameters. C_{15} is verified a priori.

$$C_{15}(x) = D_{Sg,o} - S_t.$$

Constraint C_{16} verifies that the steam generator tubes inner and outer diameter are consistent. C_{16} is verified a priori.

$$C_{16}(x) = D_{Sg,in} - D_{Sg,o}.$$

Constraint C_{17} verifies that the pressure in the steam generator tubes does not exceed their yield stress at any moment. The pressure and yield are computed as described in Section 2.3.3:

$$C_{17}(x) = \begin{cases} 0, & \text{if } P_{max,Sg}(x) - P_{yield} \leq 0 \\ 1, & \text{if } P_{max,Sg}(x) - P_{yield} > 0. \end{cases}$$

$P_{max,Sg}$ maximum pressure attained in tubes during simulation.

P_{yield} pressure that causes stress in tubes steel to reach yield point.